



8

Analysis of Oriented Patterns

Many images are composed of piecewise linear objects.

Linear or oriented objects possess directional coherence that can be quantified and examined to assess the underlying pattern.



In texture segmentation, a common approach for identifying the differing regions is to find the dominant orientation of the different texture elements.

Directional analysis is useful in the identification, segmentation, and characterization of oriented or weakly ordered texture.



8.1 Oriented Patterns in Images

In most cases of natural materials, strength is derived from highly coherent, oriented fibers.

A normal, healthy ligament is composed of bundles of collagen fibrils that are coherently oriented along the long axis of the ligament; see Figure 1.8.

An injured or healing ligament, on the other hand, contains scabs of scar material that are not aligned.

Thus, the determination of the relative disorder of collagen fibrils could provide a direct indicator of the health, strength, and functional integrity (or lack thereof) of a ligament.



Examples of oriented patterns in biomedical images include:

- Fibers in muscles and ligaments; see Figure 8.22.
- Fibroglandular tissue, ligaments, vessels, and ducts in the breast;
see Figures 7.2 and 8.66.
- Vascular networks in ligaments, lungs, and the heart.
- Bronchial trees in the lungs; see Figure 7.1.



In man-made materials such as paper and textiles, strength usually relies upon the individual fibers uniformly knotting together.

The strength of the material is directly related to the organization of the individual fibril strands.

Information related to orientation has been used in remote sensing to analyze satellite maps for the detection of anomalies.

Because man-made structures tend to have strong linear segments, directional features can help in the identification of buildings, roads, and urban features in aerial or satellite images.



8.2 Measures of Directional Distribution

Statistical measures that are commonly used for the analysis of data points in rectangular coordinate systems may lead to improper results if applied to circular or directional data.

We do not usually consider directional components in images to be directed elements (or vectors):

there should be no need to differentiate between components that are at angles θ and $\theta \pm 180^\circ$.

Therefore, we could limit our analysis to the semicircular space of $[0^\circ, 180^\circ]$ or $[-90^\circ, 90^\circ]$.



8.2.1 *The rose diagram*

The rose diagram is a graphical representation of directional data.

Corresponding to each angular interval or bin, a sector or a petal of the rose is plotted with its apex at the origin.

Usually, the radius of the sector is made proportional to the area of the image components directed in the corresponding angle band.

The area of each sector in a rose diagram as above varies in proportion to the square of the directional data.

In order to make the areas of the sectors directly proportional to the orientation data, the square roots of the data elements could be related to the radii of the sectors.



8.2.2 *The principal axis*

The spatial moments of an image may be used to determine its principal axis, which could be helpful in finding the dominant angle of directional alignment.

The moment of inertia of an image $f(x, y)$ is at its minimum when the moment is taken about the centroid (\bar{x}, \bar{y}) of the image.

The moment of inertia of the image about the line $(y - \bar{y}) \cos \theta = (x - \bar{x}) \sin \theta$ passing through (\bar{x}, \bar{y}) and having the slope $\tan \theta$ is given by

$$m_\theta = \int_x \int_y [(x - \bar{x}) \sin \theta - (y - \bar{y}) \cos \theta]^2 f(x, y) dx dy. \quad (8.1)$$



In order to make m_θ independent of the choice of the coordinates, the centroid of the image could be used as the origin.

Then, $\bar{x} = 0$ and $\bar{y} = 0$, and Equation 8.1 becomes

$$\begin{aligned} m_\theta &= \int_x \int_y (x \sin \theta - y \cos \theta)^2 f(x, y) dx dy \\ &= m_{20} \sin^2 \theta - 2 m_{11} \sin \theta \cos \theta + m_{02} \cos^2 \theta, \end{aligned} \quad (8.2)$$

where m_{pq} is the $(p, q)^{th}$ moment of the image, given by

$$m_{pq} = \int_x \int_y x^p y^q f(x, y) dx dy. \quad (8.3)$$



The moment of inertia about the principal axis is at its minimum.

Differentiating Equation 8.2 with respect to θ and equating the result to zero gives

$$m_{20} \sin 2\theta - 2 m_{11} \cos 2\theta - m_{02} \sin 2\theta = 0, \quad (8.4)$$

$$\tan 2\theta = \frac{2 m_{11}}{(m_{20} - m_{02})}. \quad (8.5)$$

By solving this equation, we can find the slope or the direction of the principal axis of the given image.



If the input image consists of directional components along an angle ϕ only, then $\phi \approx \theta$.

If there are a number of directional components at different angles, then θ represents their weighted average direction.

This method cannot detect the existence of components in various angle bands, and is not applicable for the analysis of multiple directional components.

This method cannot quantify the directional components in various angle bands.



8.2.3 Angular moments

The angular moment M_k of order k of an angular distribution is

$$M_k = \sum_{n=1}^N \theta^k(n) p(n). \quad (8.6)$$

$\theta(n)$ = center of the n^{th} angle band in degrees,

$p(n)$ = normalized weight or probability in the n^{th} band,

N = number of angle bands.



To determine the dispersion of the angular data about their principal axis, the moments may be taken with respect to the centroidal angle $\bar{\theta} = M_1$ of the distribution.

Because the second-order moment is at its minimum when taken about the centroid, we could choose $k = 2$ for statistical analysis of angular distributions.

Hence, the second central moment M_2 may be defined as

$$M_2 = \sum_{n=1}^N [\theta(n) - \bar{\theta}]^2 p(n). \quad (8.7)$$



8.2.4 *Distance measures*

The directional distribution obtained by a particular method for an image may be represented by a vector

$$\mathbf{p}_1 = [p_1(1), p_1(2), \dots, p_1(N)]^T,$$

$p_1(n)$ = distribution in the n^{th} angle band.

Let the true distribution of the image be \mathbf{p}_0 .



The Euclidean distance may be used to compare the accuracies of different methods of directional analysis:

$$\|\mathbf{p}_1 - \mathbf{p}_0\| = \sqrt{\sum_{n=1}^N [p_1(n) - p_0(n)]^2}. \quad (8.8)$$

Manhattan distance:

$$|\mathbf{p}_1 - \mathbf{p}_0| = \sum_{n=1}^N |p_1(n) - p_0(n)|. \quad (8.9)$$



8.2.5 Entropy

If we take $p(n)$ as the directional PDF of an image in the n^{th} angle band, the entropy H of the distribution is given by

$$H = - \sum_{n=1}^N p(n) \log_2[p(n)]. \quad (8.10)$$

Entropy is a useful measure of the scatter of the directional elements in an image.



If the image is composed of directional elements with a uniform distribution (maximal scatter), the entropy is at its maximum;

if the image is composed of directional elements oriented in a narrow angle band, the entropy is low.

Entropy, while not giving the angle band of primary orientation or the principal axis, could give a good indication of the directional spread or scatter. (See Figure 8.24.)

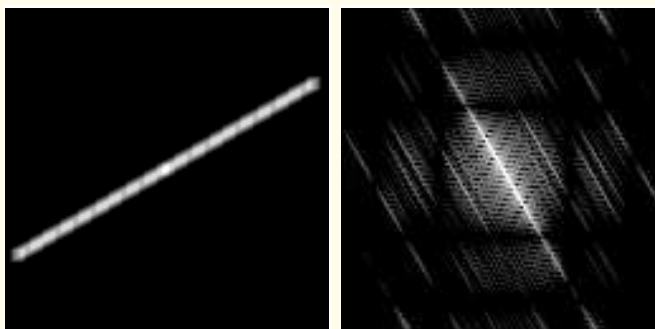


8.3 Directional Filtering

The Fourier transform of an oriented linear segment is a sinc function oriented in the direction orthogonal to that of the original segment in the spatial domain; see Figure 8.1.

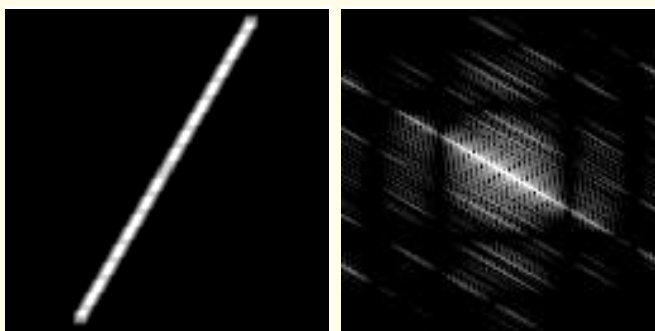
Based upon this property, we can design filters to select linear components at specific angles.

Difficulty lies in the development of high-quality filters that are able to select linear components without the undesirable effects of ringing in the spatial domain.



(a)

(b)



(c)

(d)

Figure 8.1: (a) A test image with a linear feature. (b) Log-magnitude Fourier spectrum of the test image in (a). (c) Another test image with a linear feature at a different angle. (d) Log-magnitude Fourier spectrum of the test image in (b). See also Figure 2.30.



Schiller et al. showed that the human eye contains orientation-selective structures.

This motivated research on human vision by Marr, who showed that the orientation of linear segments, primarily edges, is important in forming the *primal sketch*.

Several researchers, including Kass and Witkin, Zucker, and Low and Coggins used oriented bandpass filters to simulate the human visual system's ability to identify oriented structures in images.

Allen et al. developed a very-large-scale integrated (VLSI) circuit implementation of an orientation-specific “retina”.



Chaudhuri et al. used a set of bandpass filters to obtain directional components in SEM images of ligaments; see Sections 8.3.1 and 8.7.1.

Bruton et al. designed high-quality fan filters using methods from circuit theory.

This method results in 2D recursive filters that have high directional selectivity and good roll-off characteristics, and is described in Section 8.3.3.



8.3.1 Sector filtering in the Fourier domain

Consider a line segment of orientation (slope) a and y -axis intercept b in the (x, y) plane, with the spatial limits $[-X, X]$ and $[-Y, Y]$.

To obtain the Fourier transform of the image, we could evaluate a line integral in 2D along the line $y = ax + b$.

Assume that the integration occurs over a square region with $X = Y$.



$f(x, y) = 1$ along the line $y = ax + b$.

Using $x = (y - b)/a$, the Fourier transform of the line is

$$F(u, v) = \frac{2 Y}{|a|} \exp\left(j 2 \pi \frac{bu}{a}\right) \operatorname{sinc}\left[\left(\frac{u}{a} + v\right) Y\right]. \quad (8.11)$$



The Fourier transform of the line is a sinc function with an argument that is a linear combination of the two frequency variables (u, v), with a slope that is the negative reciprocal of the slope of the original line.

The intercept is translated into a phase shift of b/a in the u variable.

The sinc function is oriented at 90° to the original line, centered about the origin in the frequency domain regardless of the intercept of the original line.



This allows us to form filters to select lines solely on the basis of orientation and regardless of the location in the space domain.

Spatial components in a certain angle band may thus be obtained by applying a bandpass filter in an angle band perpendicular to the band of interest and applying the inverse transform.

A spatial offset would only result in a phase shift;

the magnitude spectrum would remain the same.

Figure 8.2 illustrates the ideal form of the “fan” filter that may be used to select oriented segments in the Fourier domain.

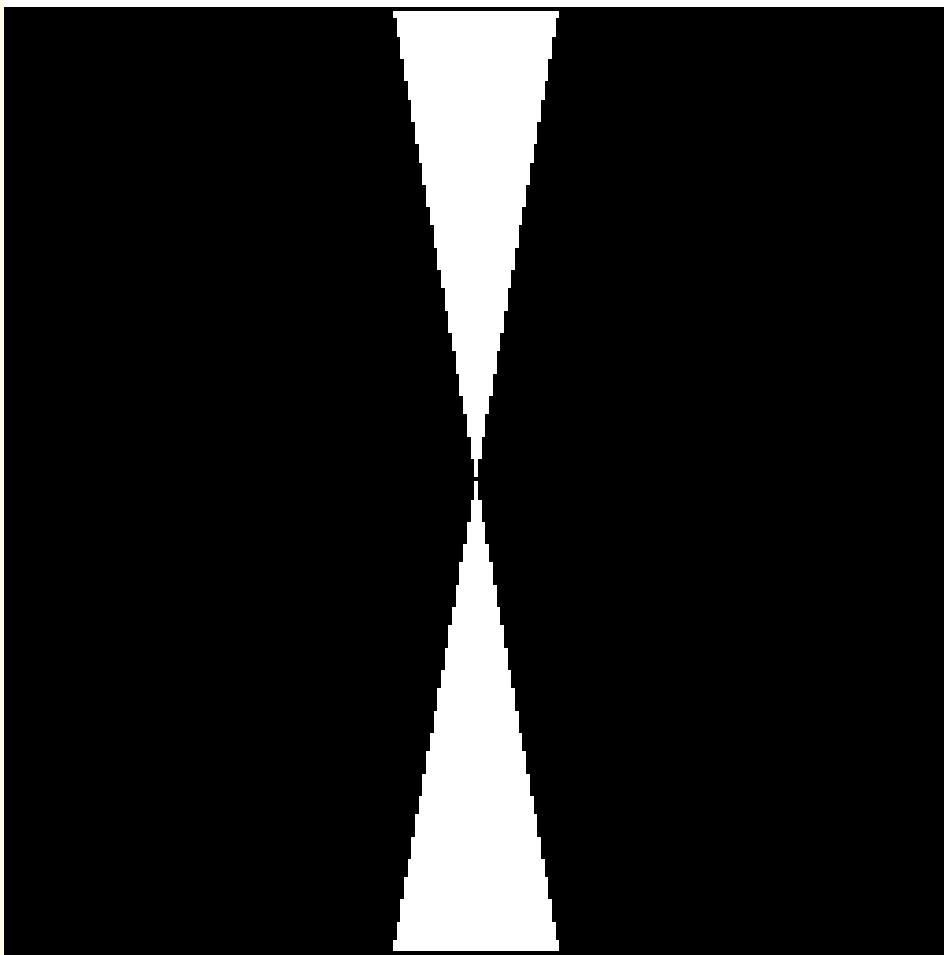


Figure 8.2: Ideal fan filter in the Fourier domain to select linear components oriented between $+10^\circ$ and -10° in the image plane. Black represents the stopband and white represents the passband. The origin $(u, v) = (0, 0)$ is at the center of the figure.



Prior to the availability of high-speed digital processing systems, attempts at directional filtering used optical processing in the Fourier domain.

Arsenault et al. used optical bandpass filters to selectively filter contour lines in aeromagnetic maps.

Duvernoy and Chalasinska-Macukow developed a directional sampling method to analyze images;

the method involved integrating along an angle band of the Fourier-transformed image to obtain the directional content.

This method was used by Dziedzic-Goclawska et al. to identify directional content in bone tissue images.



Problems with Fourier-domain techniques:

the filters do not behave well with occluded components or at junctions of linear components;

smearing of the line segments occurs, leading to inaccurate results when inverse transformed to the space domain;

truncation artifacts and spectral leakage;

ringing in the inverse-transformed image.



Chaudhuri et al. used a decomposition of the spectral domain into 12 equal angle bands at 15° per band.

Each sector filter in this design is a combination of an ideal fan filter, a Butterworth bandpass filter, a ramp-shaped lowpass filter, and a raised cosine window:

$$H(f_r) = \frac{(1 - \beta f_r)}{\left[\left[1 + \left(\frac{f_L}{f_r} \right)^{2p} \right] \left[1 + \left(\frac{f_r}{f_H} \right)^{2q} \right] \right]^{1/2}} \cos^{\alpha} \left(\frac{\theta - \theta_o}{B} \pi \right). \quad (8.12)$$



β	= slope of the weighting function	= 0.7,
f_r	= normalized radial frequency	= $\sqrt{u^2 + v^2}$,
p	= order of the highpass filter	= 6,
q	= order of the lowpass filter	= 4,
f_H	= upper cutoff frequency (normalized)	= 0.5,
f_L	= lower cutoff frequency (normalized)	= 0.02,
θ	= angle of the Fourier transform sample	= $\arctan(v/u)$,
θ_o	= central angle of the desired angle band,	
B	= angular bandwidth, and	
α	= weighting factor	= 0.5.

The combined filter with $\theta = 135^\circ$ and $B = 15^\circ$ is illustrated in Figure 8.3.

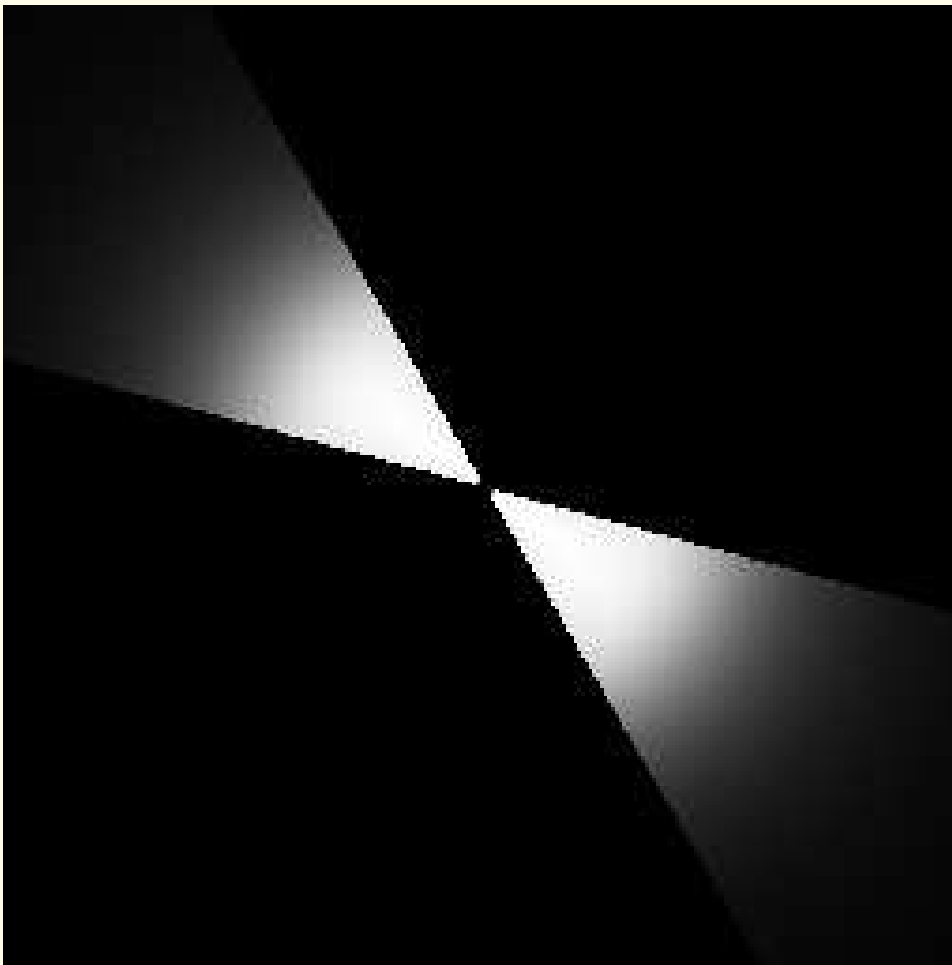


Figure 8.3: Directional (sector) filter in the Fourier domain. The brightness is proportional to the gain. Figure courtesy of W.A. Rolston.



Filtering an image with sector filters as above results in 12 component images.

Each component image contains the linear components of the original image in the corresponding angle band.

To minimize artifacts, a thresholding method was applied to accentuate the linear features in the image.

Otsu's thresholding algorithm (see Section 8.3.2) was applied in the study of collagen fiber images by Chaudhuri et al.



8.3.2 *Thresholding of the component images*

The component images from the sector filters described in Section 8.3.1 possess histograms that are smeared mainly due to the strong DC component present in images.

Even with high-quality filters, the DC component appears as a constant in all of the component images due to its isotropic nature.

This could pose problems in obtaining an effective threshold to select linear image features from the component images.

Removal of the DC component would lead to the detection of edges, and the loss of information related to the thickness of the oriented patterns.



Otsu's method of threshold selection is based upon discriminant measures derived from the gray-level PDF of the given image.

Discriminant criteria are designed so as to maximize the separation of two classes of pixels into a foreground or the desired objects and a background.

Consider the gray-level PDF $p(l)$ of an image with L gray levels, $l = 0, 1, 2, \dots, L - 1$.



If the PDF is divided into two classes C_0 and C_1 separated by a threshold k , then the probability of occurrence ω_i of the class C_i , $i = \{0, 1\}$, is given by

$$\omega_0(k) = P(C_0) = \sum_{l=0}^k p(l) = \omega(k), \quad (8.13)$$

$$\omega_1(k) = P(C_1) = \sum_{l=k+1}^{L-1} p(l) = 1 - \omega(k). \quad (8.14)$$



The class mean levels μ_i for $C_i, i = \{0, 1\}$, are

$$\mu_0(k) = \sum_{l=0}^k l P(l|C_0) \quad (8.15)$$

$$= \sum_{l=0}^k l \frac{p(l)}{\omega_0(k)} = \frac{\mu(k)}{\omega(k)},$$

$$\mu_1(k) = \sum_{l=k+1}^{L-1} l P(l|C_1) \quad (8.16)$$

$$= \sum_{l=k+1}^{L-1} l \frac{p(l)}{\omega_1(k)} = \frac{\mu_T - \mu(k)}{1 - \omega(k)}.$$



$$\omega(k) = \sum_{l=0}^k p(l), \quad (8.17)$$

$$\mu(k) = \sum_{l=0}^k l p(l) \quad (8.18)$$

are the cumulative probability and first-order moment of the PDF $p(l)$ up to the threshold level k .

$$\mu_T = \sum_{l=0}^{L-1} l p(l) \quad (8.19)$$

is the average gray level of the image.



The class variances are

$$\sigma_0^2(k) = \sum_{l=0}^k [l - \mu_0(k)]^2 P(l|C_0) \quad (8.20)$$

$$= \sum_{l=0}^k [l - \mu_0(k)]^2 \frac{p(l)}{\omega_0(k)},$$

$$\sigma_1^2(k) = \sum_{l=k+1}^{L-1} [l - \mu_1(k)]^2 P(l|C_1) \quad (8.21)$$

$$= \sum_{l=k+1}^{L-1} [l - \mu_1(k)]^2 \frac{p(l)}{\omega_1(k)}.$$



Discriminant criterion:

$$\nu = \frac{\sigma_B^2(k)}{\sigma_T^2}, \quad (8.22)$$

$$\sigma_B^2(k) = \omega_0(k)[\mu_0(k) - \mu_T]^2 \quad (8.23)$$

$$+ \omega_1(k)[\mu_1(k) - \mu_T]^2,$$

$$\sigma_T^2 = \sum_{l=0}^{L-1} (l - \mu_T)^2 p(l). \quad (8.24)$$



Otsu's algorithm aims to find the threshold level k that maximizes the discriminant criterion ν given in Equation 8.22.

Maximizing ν reduces to maximizing σ_B^2 , because σ_T^2 does not vary with the threshold k .

The optimal threshold value k^* is given as

$$k^* = \arg \left\{ \max_{0 \leq k \leq L-1} \sigma_B^2(k) \right\}. \quad (8.25)$$

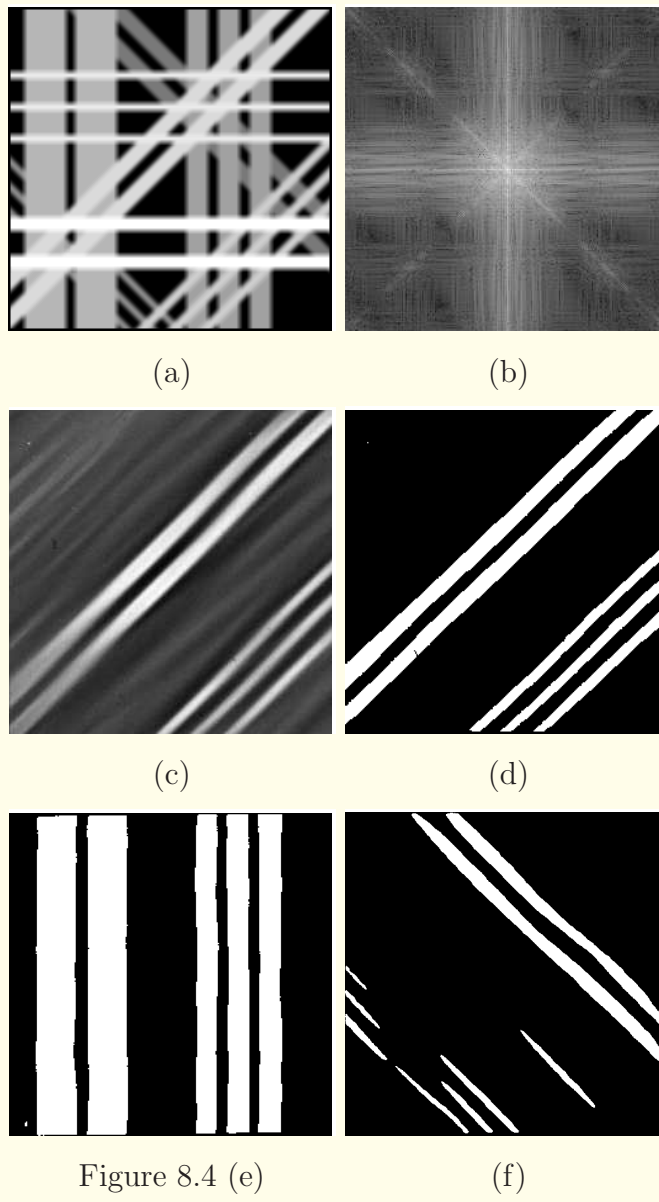


Figure 8.4 (e)

(f)



Figure 8.4: (a) A test image with overlapping directional components at 0° , 45° , 90° , and 135° . (b) Log-magnitude Fourier spectrum of the test image. Results of directional filtering (with the angle bands specified in the image domain): (c) $35^\circ - 50^\circ$. (d) Result in (c) after thresholding and binarization. (e) $80^\circ - 95^\circ$ (binarized). (f) $125^\circ - 140^\circ$ (binarized). The areas of the line segments extracted by the filtering procedure had errors, with respect to the known areas in the original test image, of 3.0%, -4.3%, -3.0%, and -28.6% for the 0° , 45° , 90° , and 135° components, respectively. Reproduced with permission from S. Chaudhuri, H. Nguyen, R.M. Rangayyan, S. Walsh, and C.B. Frank, “A Fourier domain directional filtering method for analysis of collagen alignment in ligaments”, *IEEE Transactions on Biomedical Engineering*, 34(7): 509 – 518, 1987. © IEEE.



8.3.3 Design of fan filters

The problem in the design of fan filters is in forming the filter at $(u, v) = (0, 0)$ or the DC point in the Fourier domain:

the ideal fan filter structure has a knife edge, which makes the filter nonanalytic.

2D filters are commonly derived from real, rational, continuous functions of the form

$$T(s_1, s_2) = \frac{Q(s_1, s_2)}{P(s_1, s_2)} = \frac{\sum_{m=0}^{M_2} \sum_{n=0}^{N_2} q_{mn} s_1^m s_2^n}{\sum_{m=0}^{M_1} \sum_{n=0}^{N_1} p_{mn} s_1^m s_2^n}, \quad (8.26)$$

where s_1 and s_2 are the Laplace variables.



$T(s_1, s_2)$ is the Laplace-transformed version of the 2D partial differential equation that is related to the required filter response;

$Q(s_1, s_2)$ is the numerator polynomial resulting from the Laplace transform of the forward differential forms expressed as a sum of products in s_1 and s_2 with the coefficients q_{mn} ;

M_2 and N_2 represent the order of the polynomial Q in m and n ;

$P(s_1, s_2)$ is the denominator polynomial obtained from the Laplace transform of the backward differential forms expressed as a sum of products in s_1 and s_2 with the coefficients p_{mn} ;

M_1 and N_1 represent the order of the polynomial P in m and n .



The corresponding frequency response function $T(u, v)$ is obtained by the substitution of $s_1 = j 2 \pi u$ and $s_2 = j 2 \pi v$.

The discontinuous requirement in the continuous prototype filter at the origin results in the filter transfer function $T(s_1, s_2)$ having a nonessential singularity of the second kind at the origin.

A nonessential singularity of the second kind occurs when the numerator and the denominator polynomials, $P(s_1, s_2)$ and $Q(s_1, s_2)$ in Equation 8.26, approach zero at the same frequency location (a_1, a_2) , resulting in $T(a_1, a_2) = \frac{0}{0}$.



The discrete form of the function in Equation 8.26 is obtained through the 2D version of the bilinear transform in 1D:

$$s_i = \frac{(z_i - 1)}{(z_i + 1)} \quad \text{for } i = 1, 2, \quad (8.27)$$

$$H(z_1, z_2) = \frac{B(z_1, z_2)}{A(z_1, z_2)} = \frac{\sum_{m=0}^{M_2^*} \sum_{n=0}^{N_2^*} b_{mn} z_1^{-m} z_2^{-n}}{\sum_{m=0}^{M_1^*} \sum_{n=0}^{N_1^*} a_{mn} z_1^{-m} z_2^{-n}}, \quad (8.28)$$

where the orders of the polynomials M_1^* , N_1^* , M_2^* , and N_2^* are different from the corresponding limits of the continuous-domain filter in Equation 8.26 due to the bilinear transform.



Filter design using nonessential singularities:

Bruton and Bartley viewed the nonessential singularity inherent to fan filters not as an obstacle in the design process, but as being necessary to generate useful magnitude responses.

The method relies on classical electrical circuit theory, and views the input image as a surface of electrical potential.

The surface of electrical potential is acted upon by a 2D network of components such as capacitors, inductors, and resistors;

the components act as integrators, differentiators, and dissipators.

Construct a network of components that will not add energy to the input: a completely passive or “nonenergetic” circuit that is stable.



Bruton and Bartley showed that the necessary condition for a filter to be stable is that the admittance matrix that links the current and voltage surfaces must have negative Toeplitz symmetry with reactive elements supplied by inductive elements that satisfy the nonenergic constraint.

They provided the design and coefficients of a narrow, 15° fan-stop filter, obtained using a numerical optimization method.

A filter of fifth order in z_1 and second order in z_2 was designed using this method (coefficients listed in Table 8.1).

The coefficients in the numerator and denominator each add up to zero at $z_1 = 1$ and $z_2 = 1$, confirming that the filter conforms to the requirement of the knife-edge discontinuity.

Table 8.1: Coefficients of the Discrete-domain Fan Filter with a 15° Fan Stopband. Data Courtesy of N.R. Bartley.

b_{mn}	$n = 0$	$n = 1$	$n = 2$
$m = 0$	0.02983439380935332	-0.6855181788590949	0.7027763362367445
$m = 1$	-0.1469615281783627	3.397745073546105	-3.629041657524303
$m = 2$	0.2998008459584214	-6.767662643767763	7.49061181619684
$m = 3$	-0.3165448124171246	6.771378027945815	-7.725572280971142
$m = 4$	0.1724438585800683	-3.403226865621513	3.981678690012933
$m = 5$	-0.03857214742977072	0.6872844383634052	-0.82045337027416
a_{mn}	$n = 0$	$n = 1$	$n = 2$
$m = 0$	1.000000000000000	-0.82545044546957	0.03722700706807863
$m = 1$	-4.476280705843249	3.791276128445935	-0.161179724642936
$m = 2$	8.03143251366382	-7.00124160940265	0.2870351311929377
$m = 3$	-7.220029589516617	6.499290024154175	-0.2623441075303727
$m = 4$	3.252431250257176	-3.03268003600527	0.122960282645262
$m = 5$	-0.5875259501210567	0.5687740686107076	-0.0236904653803231



Rotation of the filter and image:

The fan filter design algorithm of Bruton and Bartley provides filters only for a specific angle band — in the above case, for a 15° bandstop filter centered at 0° in the Fourier domain.

To obtain filters with different central orientations, it is necessary to perform a rotation of the prototype filter.

$$s_1 \Leftarrow s_1 \cos \theta + s_2 \sin \theta, \quad (8.29)$$

$$s_2 \Leftarrow s_2,$$

where θ is the amount of rotation desired.



The rotation step above is not the usual rotational transformation for filters, but it is necessary to use this transformation in order to ensure that the filter is stable.

If the normal rotational transformation were to be used, s_2 would also be rotated as

$$s_2 \Leftarrow -s_1 \sin \theta + s_2 \cos \theta. \quad (8.30)$$

Then, values of s_2 could turn out to be negative: this would indicate that there would be energy added to the system, which would make the filter unstable.



Suppose that the prototype filter as in Equation 8.26, given by $T_0(s_1, s_2)$ and with the corresponding frequency response function given by $T_0(u, v)$, is bounded by the straight lines L_- and L_+ passing through the origin at angles of $-\theta_p$ and $+\theta_p$ with the central line of the filter $CL = 0^\circ$ where $u = 0$.

The lines L_- and L_+ are given by [see Figure 8.5 (a)]

$$\begin{aligned} u \cos \theta_p - v \sin \theta_p &= 0 : L_- \\ u \cos \theta_p + v \sin \theta_p &= 0 : L_+ \end{aligned} \quad (8.31)$$



As a result of the transformation in Equation 8.29, the center of the passband of the rotated frequency response $T_r(u, v)$ is given as $T_0(u', v') = T_0(u \cos \theta_c + v \sin \theta_c, v)$.

Similarly, the straight lines L_- and L_+ are rotated to the straight lines given by

$$\begin{aligned} u \cos \theta_p \cos \theta_c + v (\sin \theta_c \cos \theta_p - \sin \theta_p) &= 0 : L_- \\ u \cos \theta_p \cos \theta_c + v (\sin \theta_c \cos \theta_p + \sin \theta_p) &= 0 : L_+; \end{aligned} \quad (8.32)$$

[see Figure 8.5 (b)].

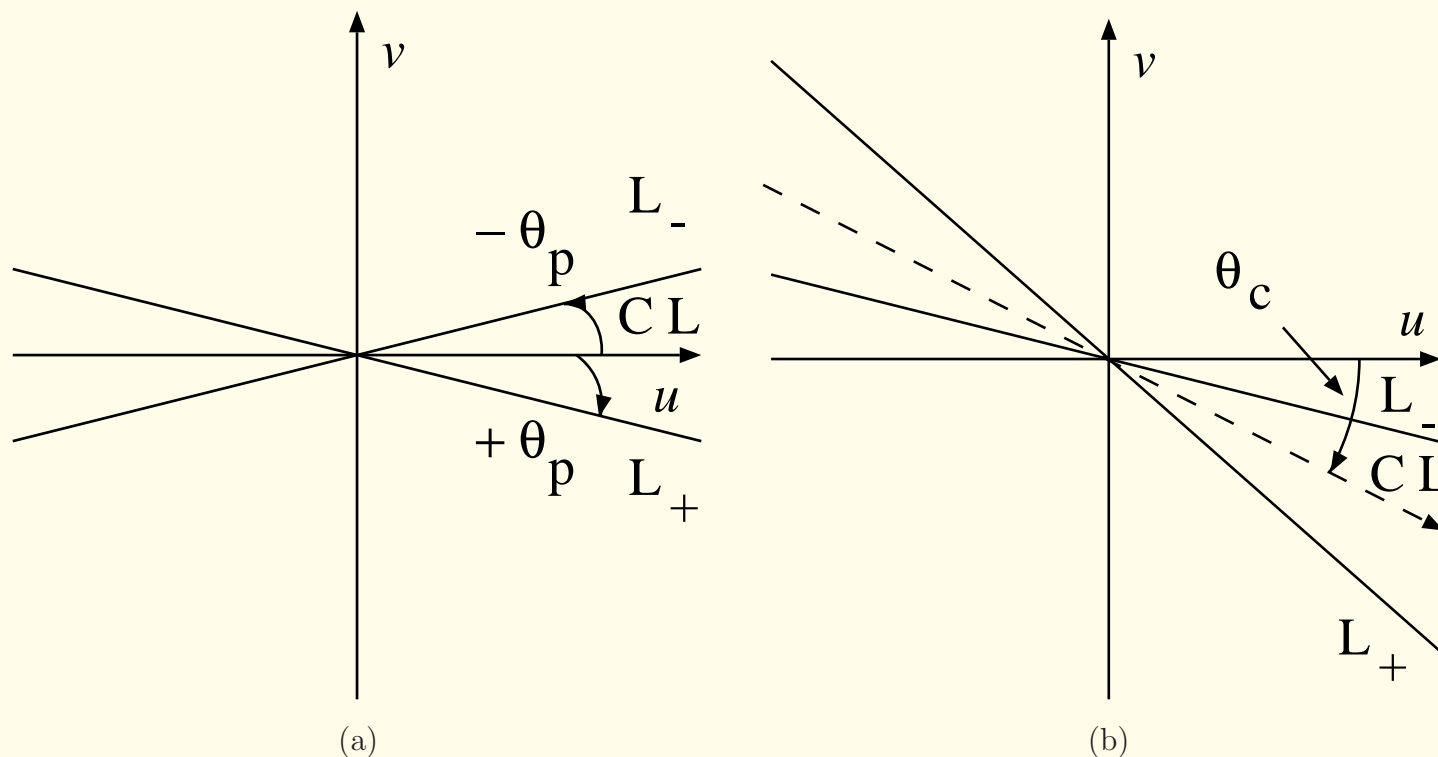


Figure 8.5: (a) Original fan filter. (b) The fan filter after rotation by the transformation given in Equation 8.29. Figure courtesy of W.A. Rolston.

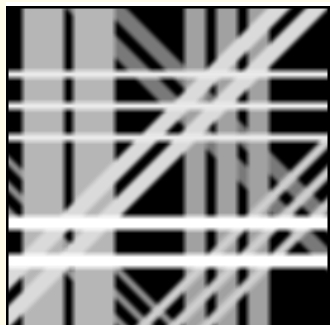


A limitation to filter rotation as above is that rotating the filter by more than 45° would result in a loss of symmetry about the central line of the filter.

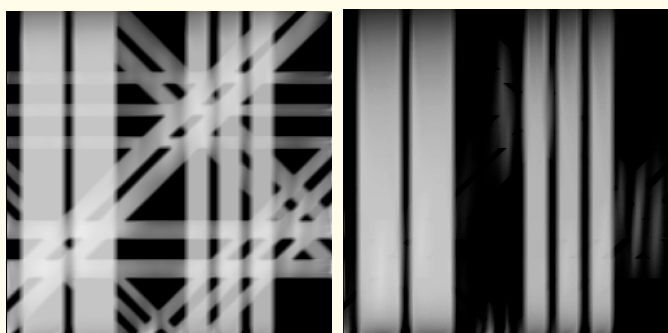
The rotational warping effect may be compensated for in the prototype filter $T_0(s_1, s_2)$.

In the work of Rolston, the prototype filter was rotated by 45° in either direction to obtain filters covering an angle band of 90° ($0^\circ - 45^\circ$ and $135^\circ - 180^\circ$ in the Fourier domain).

Filtering in the range $45^\circ - 135^\circ$ was achieved by rotating the image by 90° before passing it through the same filters as above.



(a)



(b)

(c)

Figure 8.6: (a) A test image with overlapping directional components at 0° , 45° , 90° , and 135° . Results of fan filtering at 90° after (b) one pass, (c) nine passes. Figure courtesy of W.A. Rolston.



8.4 Gabor Filters

Gabor suggested the use of time-limited functions as the kernels of a transform instead of the unlimited sine and cosine functions that are the kernel functions of the Fourier transform.

Gabor showed that complex, sinusoidally modulated, Gaussian basis functions satisfy the lower bound on the uncertainty principle that governs the resolution in time and frequency:

$$\Delta t \Delta f \geq \frac{1}{4\pi}, \quad (8.33)$$

where Δt and Δf are time and frequency resolution.



The uncertainty principle implies that there is a resolution limit between the spatial and the Fourier domains.

The uncertainty relationship in 2D is given by

$$\Delta x \Delta y \Delta u \Delta v \geq \frac{1}{16\pi^2}, \quad (8.34)$$

where Δx and Δy represent the spatial resolution,

and Δu and Δv represent the frequency resolution.



Gabor functions provide optimal joint resolution in both the Fourier and time domains in 1D, and form a complete basis set through phase shift and scaling or dilation of the original (mother) basis function.

The set of functions forms a multiresolution basis that is commonly referred to as a wavelet basis (formalized by Mallat).

Daugman extended Gabor functions to 2D:

2D sinusoidal plane waves of some frequency and orientation in a 2D Gaussian envelope.

Gabor functions have been found to provide good models for the receptive fields of simple cells in the striate cortex.



The 2D Gabor functions are given as

$$h(x, y) = g(x', y') \exp[-j 2 \pi (Ux + Vy)],$$

$$(x', y') = (x \cos \phi + y \sin \phi, -x \sin \phi + y \cos \phi), \quad (8.35)$$

where (x', y') are the (x, y) coordinates rotated by ϕ ,

$$g(x, y) = \left(\frac{1}{2\pi\lambda\sigma^2} \right) \exp \left[-\frac{(x/\lambda)^2 + y^2}{2\sigma^2} \right] \quad (8.36)$$

is a Gaussian shaping window with the aspect ratio λ .

U, V are the center frequencies in the (u, v) frequency plane.



Gabor functions act as bandpass filters with directional selectivity.

The frequency domain is usually divided into a symmetric set of slightly overlapping regions at octave intervals.

The imaginary component of the Gabor function is the Hilbert transform of its real component.

The Hilbert transform shifts the phase of the original function by 90° , resulting in an odd version of the function.

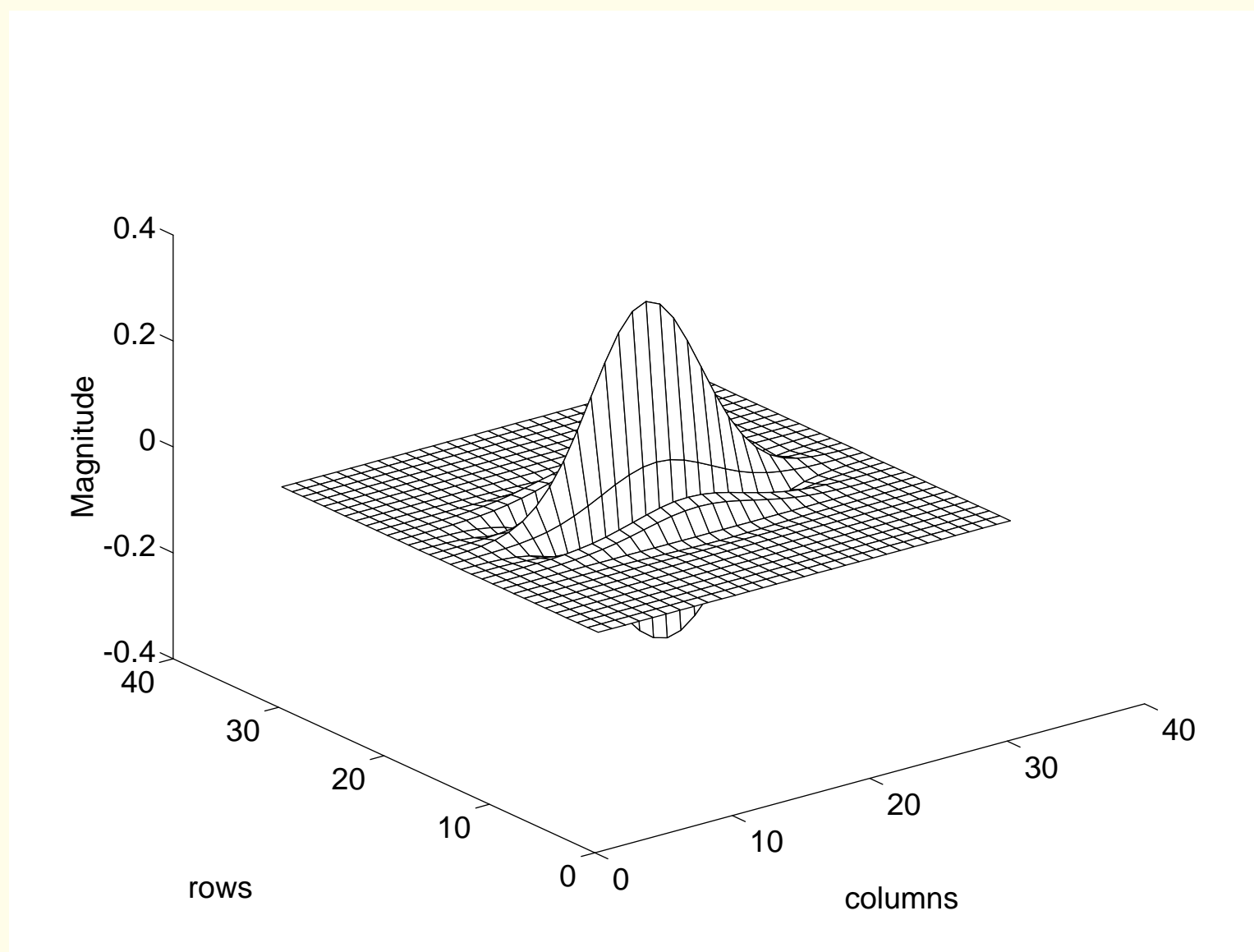


Figure 8.7: An example of the Gabor kernel with $\sigma = 0.5$, $\lambda = 0.6$, $U = 1$, $V = 0$, and $\phi = 0$ (with reference to Equations 8.35 and 8.36). Figure courtesy of W.A. Rolston.

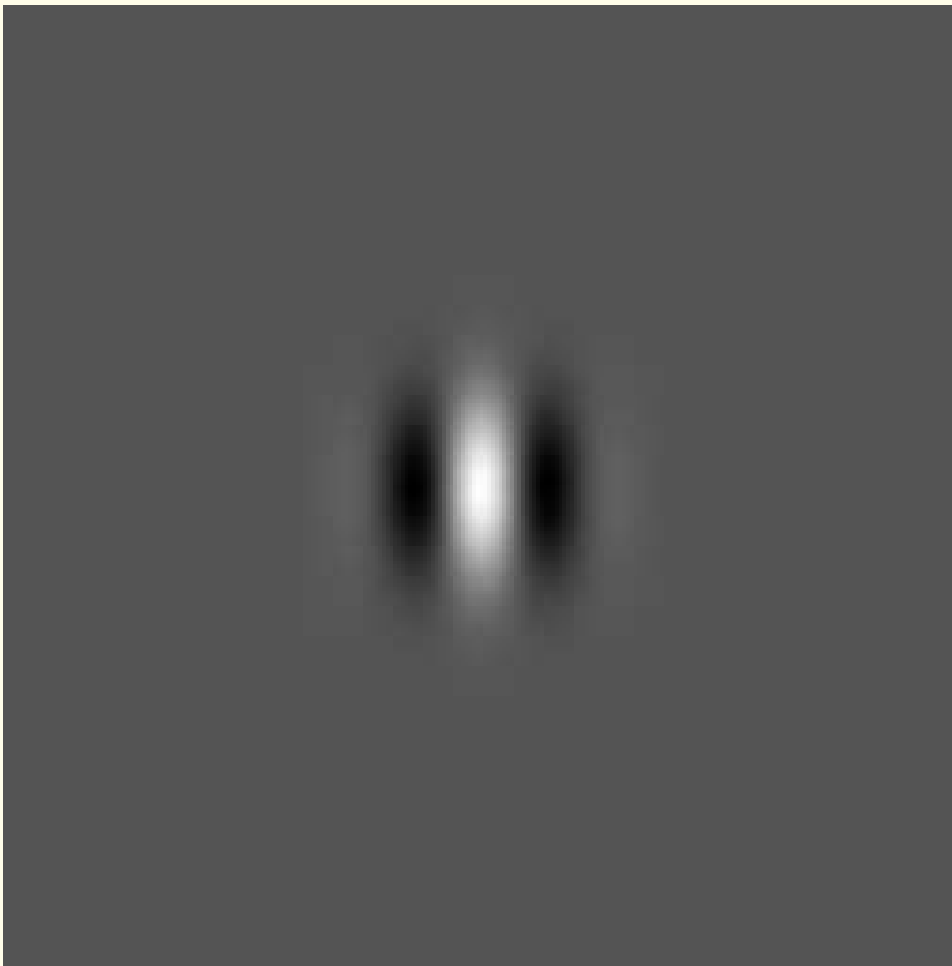


Figure 8.8: An example of a Gabor kernel, displayed as an image. Figure courtesy of W.A. Rolston.

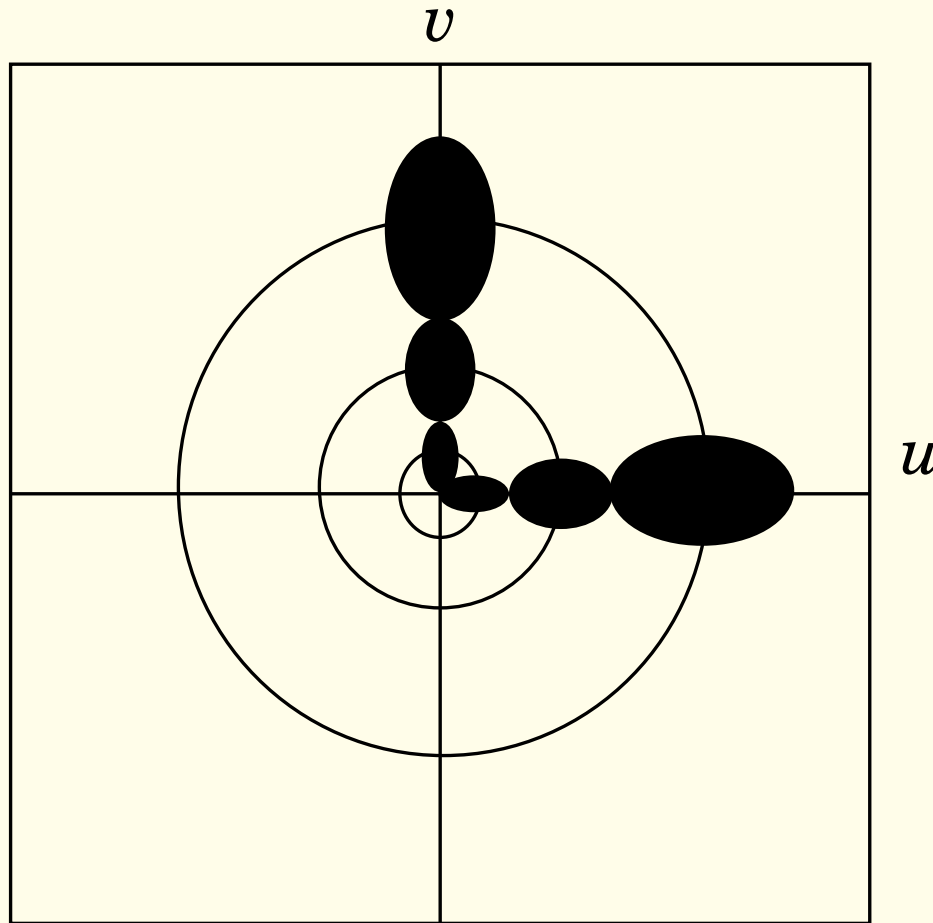


Figure 8.9: Division of the frequency domain by Gabor filters. Two sets of oval regions are shown in black, corresponding to the passbands of three filters in each set, oriented at 0° and 90° . In each case, the three regions correspond to three scales of the Gabor wavelets. There is a 90° shift between the angles of corresponding filter functions in the space and frequency domains. Figure courtesy of W.A. Rolston.



8.4.1 *Multiresolution signal decomposition*

Multiresolution signal analysis is performed using a single prototype function called a wavelet.

Fine temporal or spatial analysis is performed with contracted versions of the wavelet;

fine frequency analysis is performed with dilated versions.

The definition of a wavelet is flexible, and requires only that the function have a bandpass transform;

thus, a wavelet at a particular resolution acts as a bandpass filter.



The bandpass filters must have constant relative bandwidth or constant quality factor.

The constant relative bandwidth of perceptual processes such as the auditory and visual systems has long been recognized.

Multiresolution analysis has also been used in computer vision for tasks such as segmentation and object recognition.

The analysis of nonstationary signals often involves a compromise between how well transitions or discontinuities can be located, and how finely long-term behavior can be identified.

This is reflected in the uncertainty principle.



Gabor originally suggested his kernel function to be used over band-limited, equally spaced areas of the frequency domain, or equivalently, with constant window functions.

This is commonly referred to as the short-time Fourier transform (STFT) for short-time analysis of nonstationary signals.

The 2D equivalent of the STFT is given by

$$\begin{aligned} F_S(x', y', u, v) = & \int_{x=-\infty}^{\infty} \int_{y=-\infty}^{\infty} f(x, y) w(x - x', y - y') \\ & \times \exp[-j 2 \pi (ux + vy)] dx dy. \end{aligned} \quad (8.37)$$

w = a windowing function, f = signal (image) to be analyzed.



Advantage of short-time (or moving-window) analysis:
if the energy of the signal is localized in a part of the signal,
it is also localized to a part of the 4D space (x', y', u, v).

Disadvantage: the same window is used at all frequencies, the resolution is the same at all locations in the resultant space.

The uncertainty principle does not allow for arbitrary resolution in both of the space and frequency domains:

if the window function is small, the large-scale behavior of the signal is lost,

if the window is large, rapid discontinuities are washed out.



To identify fine or small-scale discontinuities in signals, we need to use basis functions that are small in spatial extent,

whereas functions of large spatial extent would be required to obtain fine frequency analysis.

By varying the window function, one will be able to identify both the discontinuous and stationary characteristics of a signal.

The notion of *scale* is introduced when the size of the window is increased by an order of magnitude.



Such a multiresolution or multiscale view of signal analysis is the essence of the wavelet transform.

Wavelet decomposition, in comparison to STFT analysis, is performed over regions in the frequency domain of constant relative bandwidth as opposed to a constant bandwidth.



The wavelet basis is given by

$$h_{x',y',\lambda_1,\lambda_2}(x,y) = \frac{1}{\sqrt{\lambda_1 \lambda_2}} h\left(\frac{x-x'}{\lambda_1}, \frac{y-y'}{\lambda_2}\right) \quad (8.38)$$

where x' , y' , λ_1 , and λ_2 are real numbers,

and h is the basic or mother wavelet.

For large values of λ_1 and λ_2 , the basis function becomes a stretched or expanded version of the prototype wavelet or a low-frequency function,

for small λ_1 and λ_2 , the basis function becomes a contracted wavelet, that is, a short, high-frequency function.



The wavelet transform is then defined as

$$\begin{aligned} F_W(x', y', \lambda_1, \lambda_2) &= \frac{1}{\sqrt{\lambda_1 \lambda_2}} \int_{x=-\infty}^{\infty} \int_{y=-\infty}^{\infty} f(x, y) \\ &\quad \times h\left(\frac{x - x'}{\lambda_1}, \frac{y - y'}{\lambda_2}\right) dx dy. \quad (8.39) \end{aligned}$$

Wavelet analysis of a signal consists of the contraction, dilation, and translation of the basic mother wavelet, and computing the projections of the resulting wavelets on to the given signal.



8.4.2 *Formation of the Gabor filter bank*

In the method proposed by Bovik et al., the given image is convolved with the complex Gabor kernel, and the maximum magnitude of the result is taken as an indicator to identify changes in the dominant orientation of the image.

In the work of Rolston and Rangayyan, this method was observed to fail in the presence of broad directional components.

The real component of the Gabor filter acts as a matched filter to detect broad directional components, and thus, is better suited to the identification of such regions.



The parameters of Gabor filters that may be varied are as follows:

With reference to Equations 8.35 and 8.36, the parameter σ specifies the spatial extent of the filter;

λ specifies the aspect ratio of the filter that modulates the σ value.

If $\lambda = 1$, the ϕ parameter in Equation 8.35 need not be specified, because $g(x, y)$ is then isotropic.

In the frequency domain, this results in an oriented filter occupying the middle subsection of the corresponding ideal fan filter, with the orientation given by $\tan^{-1}(V/U)$ (Figure 8.9).

These parameters completely specify the Gabor filter bank.



In the directional analysis algorithm proposed by Rolston and Rangayyan, only the real component of the Gabor wavelet is used, with $\lambda = 1/0.6$, $\sigma = 1.0$, and the primary orientation given by $\tan^{-1}(V/U) = 0^\circ, 45^\circ, 90^\circ$, and 135° .

A given image is analyzed by convolving band-limited and decimated versions of the image with the same analyzing wavelet.

When a decimated image is convolved with a filter of constant spatial extent, relative to the original image, the filter is effectively scaled larger with respect to the decimated image.

The advantage of this procedure is that filters with larger σ values, or with center frequencies closer to DC, can be simulated, instead of resorting to using filters of larger spatial extent.



Filters with larger σ values correspond to portions of the frequency domain closer to the DC point; see Figure 8.9.

The frequency plane is completely covered by the decimation and filtering operation.

Each black oval in Figure 8.9 represents the frequency band being filtered by each decimation and filtering operation.

The largest black oval at each orientation corresponds to one-to-one filtering, and the smaller ovals closer to the origin correspond to higher orders of decimation and filtering.



Higher levels of decimation and filtering geometrically approach the DC point.

The size of the original image imposes a limiting factor:
a 256×256 image can only be decimated a few times before the details of interest are lost.

Because the filter bank works on decimated images, the computational load of convolution reduces geometrically at each successive stage of decimation.



8.4.3 *Reconstruction of the Gabor filter bank output*

Directional filtering and analysis procedures proposed by Rolston and Rangayyan:

The given image is decimated and convolved at each of three scales with a filter of fixed size.

Decimation and filtering at each scale results in equal energy across all of the scales due to the selection of the filter coefficients.

After interpolation of the decimated and convolved images, the responses at the different scales can be added without scaling to obtain the overall response of the filter at the different scales.



After obtaining the responses to the filters at 0° , 45° , 90° , and 135° , a vector summation of the filter responses is performed.

Vector summation is performed at each pixel in the original image domain to obtain a magnitude and angle at each pixel.

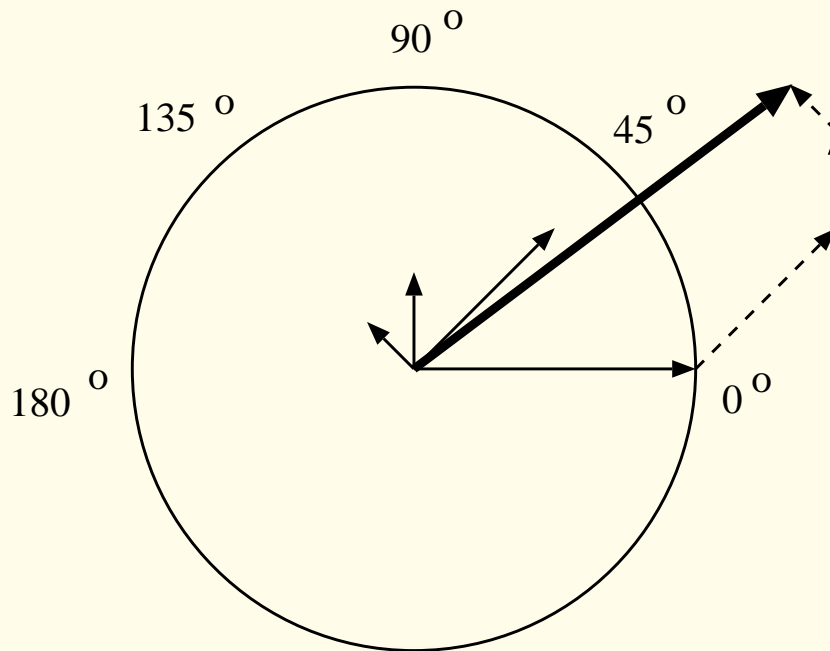


Figure 8.10: Vector summation of the responses of Gabor filters at 0° , 45° , 90° , and 135° . Figure courtesy of W.A. Rolston.

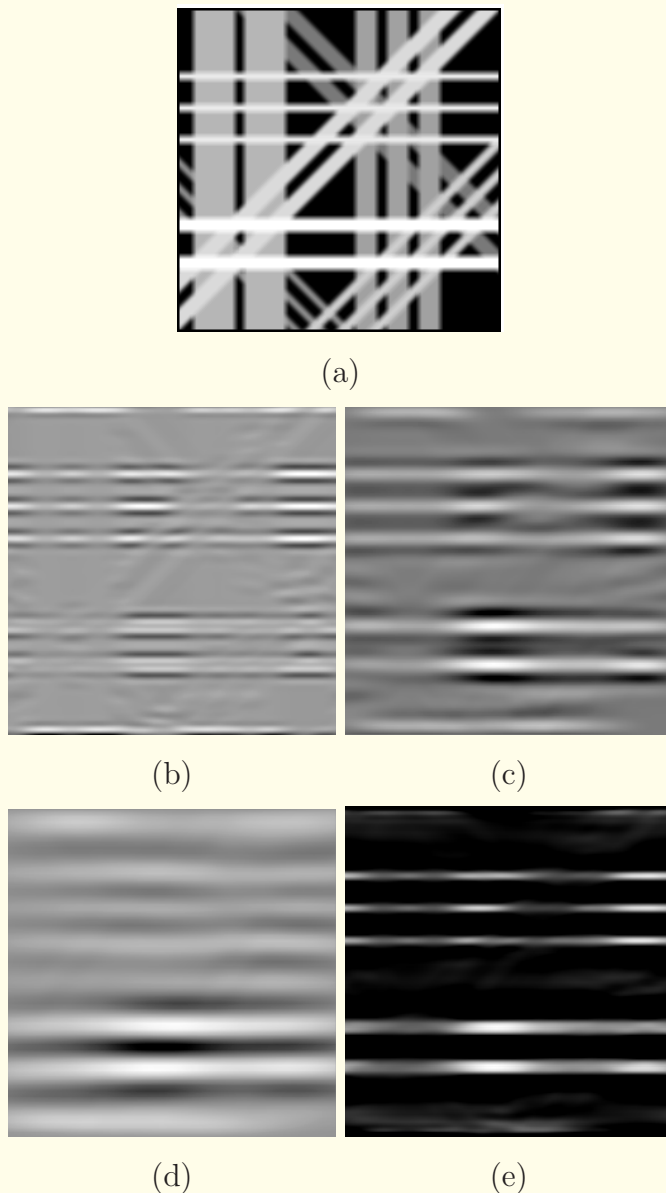


Figure 8.11: (a) A test image with overlapping directional components at 0° , 45° , 90° , and 135° . Results of Gabor filtering at 0° after decimation at (b) one-to-one, (c) two-to-one, and (d) four-to-one. (e) Overall response at 0° after vector summation as illustrated in Figure 8.10. Figure courtesy of W.A. Rolston.



8.5 Directional Analysis via Multiscale Edge Detection

Methods for edge detection via multiscale analysis using LoG functions are described in Section 5.3.3.

Liu et al. applied further steps to the edge stability map obtained by this method (see Figure 5.16) to detect linear segments corresponding to collagen fibers in SEM images of ligaments.

Estimating the area of directional segments:

Directional analysis requires the estimation of the area covered by linear segments in specified angle bands.

The pattern boundaries obtained by the relative stability index (see Equation 5.26) may be used for this purpose.



The directional information of a pattern is given by the directions of the gradients along the detected pattern boundaries.

Figure 8.12 (a) depicts the approach of Liu et al. for area computation, where two pattern-covered regions are denoted by R_A and R_B .

The arrows along the boundaries indicate the directions of the gradients, which are computed from the original image on a discretized grid.

The use of gradients enables the definition of the region enclosed by the boundaries.

A linear segment can be identified by a pair of line segments running in opposite directions.



Liu et al. proposed a piecewise labeling procedure that includes two steps: line labeling and region labeling.

In the line-labeling procedure, the full plane is sectioned into eight sectors (see Figure 8.13).

A set of templates is defined for pixel classification.

The relative stability index is scanned left to right and top to bottom.

To each element in the relative stability index, a line label is assigned according to its match with one of the templates.

A structure array is constructed to store the descriptions of the lines at both pixel and line levels.



The structure array contains several description fields:

the line starting location (xs, ys) ;

the ending location (xe, ye) ;

the orientation θ ;

and a corner label, which is also a structure array, containing the corner location and the lines that form the corner.

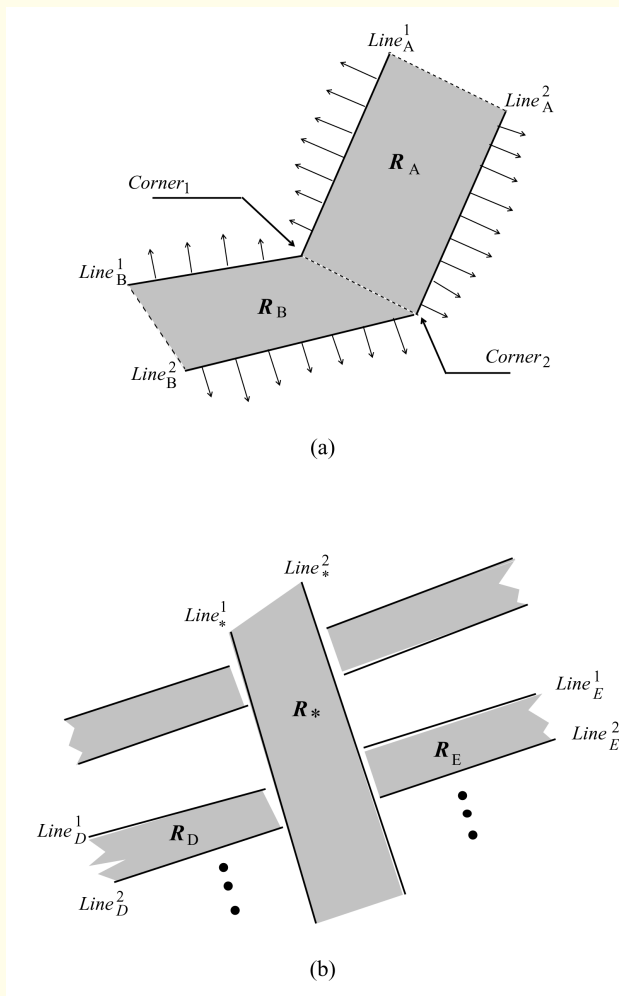


Figure 8.12: (a) Computation of the area covered by directional segments. The arrows perpendicular to the pattern boundaries represent gradient directions used for detecting the interior of the linear segment over which the area is computed. The directional information associated with the pattern is also stored for analysis. (b) Computation of occluded segments based upon the detected T-joints. The subscripts denote different regions, and the superscripts denote the line numbers. Reproduced with permission from Z.-Q. Liu, R.M. Rangayyan, and C.B. Frank, “Directional analysis of images in scale-space”, *IEEE Transactions on Pattern Analysis and Machine Intelligence*, 13(11):1185–1192, 1991. © IEEE.



Once the line segments have been labeled, a set of region descriptors is generated, which includes

paired line labels, their starting and ending locations, orientation, and the area of the region [see Figure 8.12 (a)].

In region labeling, a line (for example, Line_A^1) is paired with an adjacent line (for example, Line_A^2) having a direction that is in the sector opposite to that of Line_A^1 (see Figure 8.13).

The area of the linear segment (R_A) is then computed by counting the number of pixels contained by the pair of line segments.

The orientation of the linear segment is indicated by the orientation of the pair of line segments.



For instance, if Line_A^1 and Line_A^2 form a pair, their associated region descriptor can be defined as

$$R\{A, [(xs, ys), (xe, ye), \theta]_1; [(xs, ys), (xe, ye), \theta]_2; \alpha\}, \quad (8.40)$$

where the subscripts 1 and 2 represent Line_A^1 and Line_A^2 , respectively, and α is the area computed for the region R_A .

[See Figure 8.12 (a).]

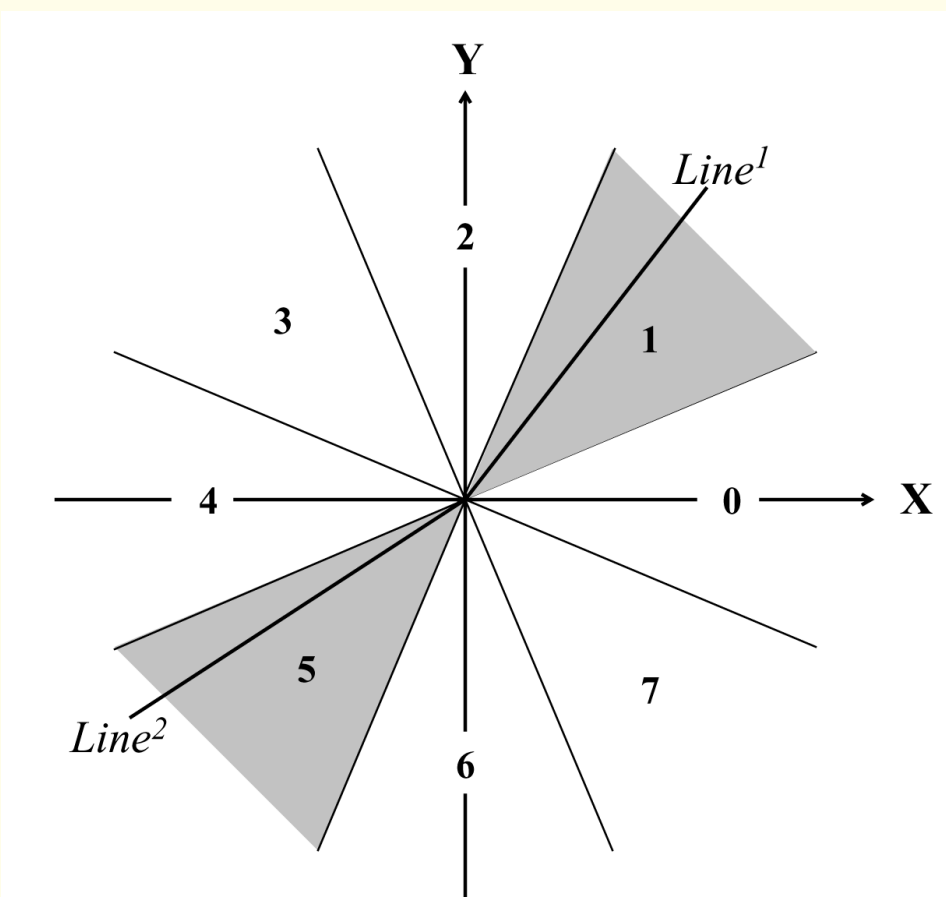


Figure 8.13: The image plane is divided into eight sectors. *Line¹* and *Line²* form a pair. Reproduced with permission from Z.-Q. Liu, R.M. Rangayyan, and C.B. Frank, “Directional analysis of images in scale-space”, *IEEE Transactions on Pattern Analysis and Machine Intelligence*, 13(11):1185–1192, 1991. © IEEE.



Detection of occluded linear segments:

In natural images, linear patterns often intersect and some segments of a linear pattern will be occluded.

Occluded segments typically appear as T-junctions in an edge image.

As described above, a corner structure array is generated along with the line structure array.

T-junctions can be readily detected by inspecting the corners, and if necessary, linking lines according to the following procedure.



The lines that form T-junctions with a common line [see Figure 8.12 (b)] are considered to be occluded line segments and are stored in a T-junction array structure:

$$T\{k, Line_A^1, Line_A^2; Line_B^1, Line_B^2; \dots; Line_*^k\}, \quad (8.41)$$

where k indicates the k^{th} T-junction structure, and the subscript $*$ indicates the region associated with the common line.

After all the T-junction structures are constructed, they are paired by bringing together the T-junction structures with $Line_*^k$ that share the same region.



Corresponding line elements in paired T-junction structures are then compared to detect lines that cut across the common region.

This is performed by verifying if a line in one of the T-junction structures of the pair lies within a narrow cone-shaped neighborhood of the corresponding line in the other T-junction structure of the pair.

If such a line pair is detected across a pair of T-junction structures, the lines are considered to be parts of a single line with an occluded part under the common region.



Furthermore, if two such occluded lines form two regions (on either side of the common region), the two regions are merged by adding the occluded region, and relabeled as a single region.

With reference to Figure 8.12 (b), the above procedure would merge the regions labeled as R_D and R_E into one region, including the area occluded in between them, R_* .

The entire procedure for directional analysis proposed by Liu et al. for directional analysis via multiscale filtering with LoG functions (see Section 5.3.3) is summarized by the following algorithm.



1. Generate a set of zero-crossing maps (images).
2. Classify or authenticate the zero crossings.
3. Generate the adjusted zero-crossing maps from the original zero-crossing maps.
4. Generate a stability map from the adjusted zero-crossing maps.
5. Generate the relative stability index map.
6. Compute the edge orientation from the relative stability index map and the original image.
7. Compute the orientational distribution of the segments identified.
8. Compute statistical measures to quantify the angular distribution of the linear patterns (see Section 8.2).



The methods described above were tested with the image in Figure 8.4 (a).

The areas of the line segments extracted by the procedures had errors, with respect to the known areas in the original test image, of -2.0% , -6.3% , -3.4% , and -40.6% for the 0° , 45° , 90° , and 135° components, respectively.

Liu et al. applied the procedures described above for the analysis of collagen remodeling in ligaments; see Section 8.7.1.



8.6 Hough-Radon Transform Analysis

The Hough transform is a method of transforming an image into a parameter domain where it is easier to obtain the desired information in the image; see Section 5.6.1.

The main drawback of the Hough transform is that it is primarily applicable to binary images.

The results are dependent upon the binarization method used for segmenting the image.

Rangayyan and Rolston proposed the use of a combination of the Hough transform and the Radon transform that overcomes this drawback.



8.6.1 *Limitations of the Hough transform*

With reference to Figure 8.14, we see that a straight line can be specified in terms of its orientation θ with respect to the x axis, and its distance ρ from the origin:

$$\rho = x \cos \theta + y \sin \theta. \quad (8.42)$$

In this form of parameterization, any straight line is bounded in angular orientation by the interval $[0, \pi]$

and bounded by the Euclidean distance to the farthest point of the image from the center of the image.



For a specific point in the image domain (x_i, y_i) , we obtain a sinusoidal curve in the Hough domain (ρ, θ) .

Each point (x_i, y_i) lying on a straight line with $\rho = \rho_0$ and $\theta = \theta_0$ in the image domain corresponds to a sinusoidal curve in the (ρ, θ) domain specified by

$$\rho_0 = x_i \cos \theta_0 + y_i \sin \theta_0. \quad (8.43)$$

For each point in the image domain, the Hough transform performs a one-to-many mapping, resulting in a modulated sum of sinusoids in the Hough domain.



The Hough transform is referred to as a voting procedure, where each point in the image casts votes for all parameter combinations that could have produced the point.

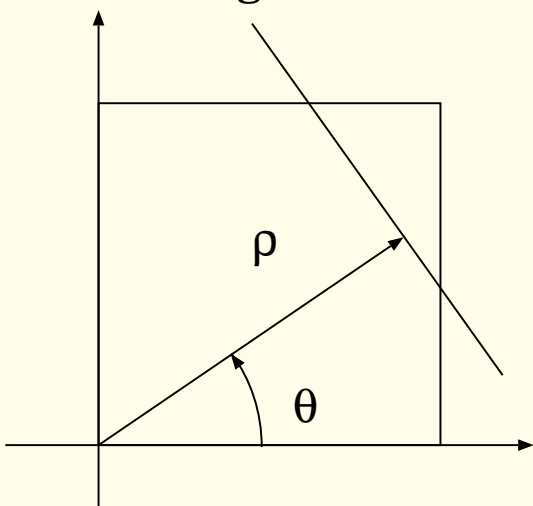
All of the sinusoids resulting from the mapping of a straight line in the image domain have a common point of intersection at (ρ_0, θ_0) in the Hough domain.

Linear segments in the spatial domain correspond to large-valued points in the Hough domain; see Figures 5.39 and 5.40.

Thus, the problem of determining the directional content of an image becomes a problem of peak detection in the Hough parameter space.

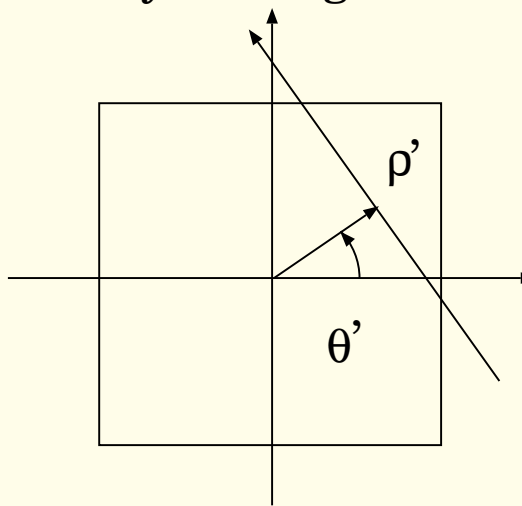


Straight line



Hough transform

Ray of integration



Radon transform

Figure 8.14: Parameters in the representation of a straight line in the Hough transform and a ray in the Radon transform. Reproduced with permission from R.M. Rangayyan and W.A. Rolston, “Directional image analysis with the Hough and Radon transforms”, *Journal of the Indian Institute of Science*, 78: 17–29, 1998. © Indian Institute of Science.



The Hough transform appears to be the ideal tool for detecting linear components in images.

However, there are some limitations to this approach.

The results are sensitive to the quantization intervals used for the angle θ and the distance ρ .

Decreasing the quantization step for θ increases the computation time, because the calculation for ρ needs to be performed across each value of θ and each pixel.



Another problem with this method is the “crosstalk” between multiple straight lines in the Hough domain.

If the image contains several lines parallel to the x axis, they would correspond to several peak values in the Hough domain at differing ρ values for $\theta = 90^\circ$.

However, the Hough transform would also detect false linear segments for $\theta = 0^\circ$, which would show up as smaller peaks at a continuum of ρ values in the Hough domain; see Figure 8.15.

This is caused by the fact that the Hough transform finds line segments at specific ρ values that are not necessarily contiguous.

Several straight lines may be perceived within a broad element with angles spread about the dominant orientation of the element, as well as at several other angles: see Figure 8.16.

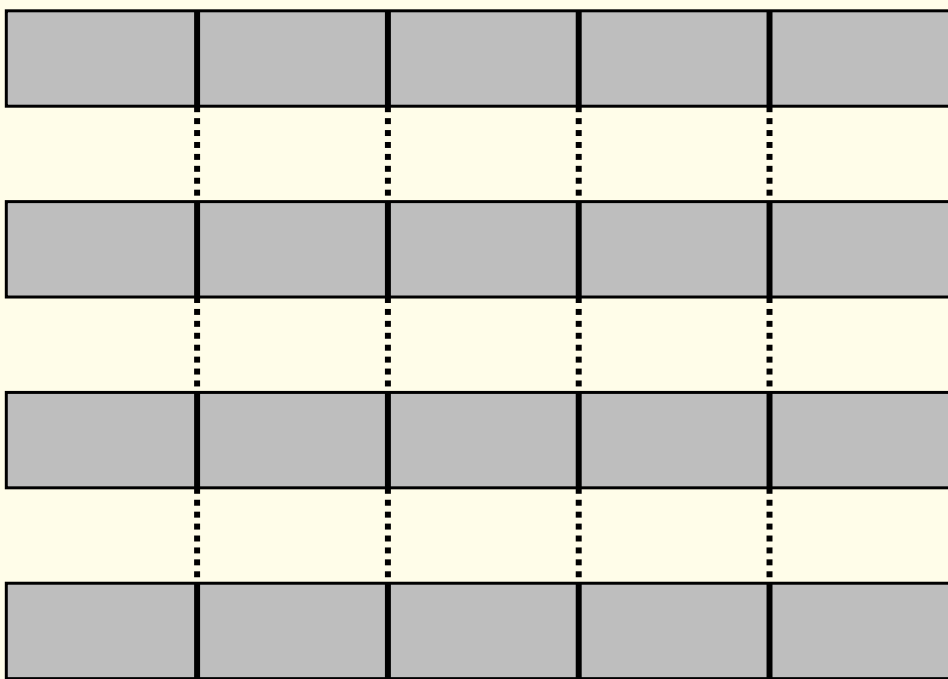


Figure 8.15: Crosstalk between multiple lines causing the Hough transform to detect false lines. In the case illustrated, several short segments of vertical lines are detected, in addition to the true horizontal lines.

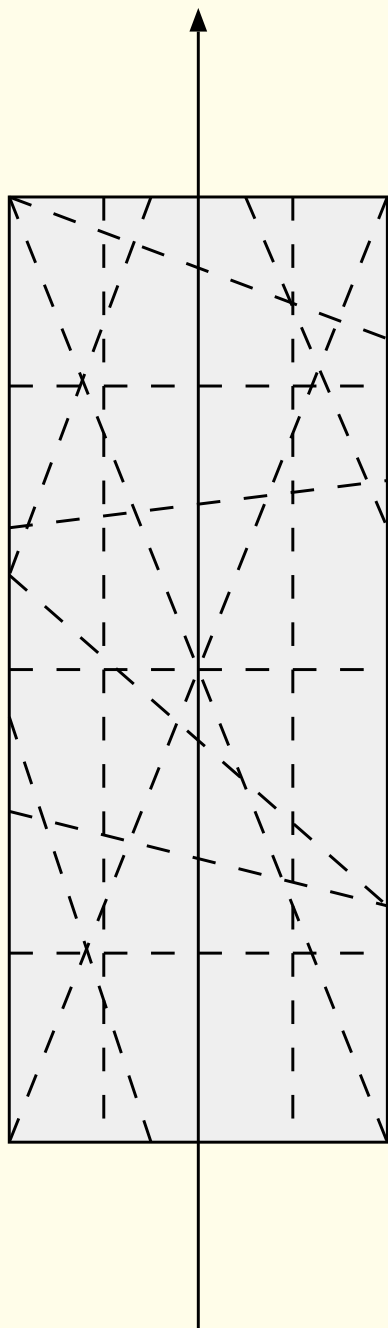


Figure 8.16: False detection of straight lines at several angles (dashed lines) within a broad linear feature by the Hough transform.



The Hough transform has the desirable feature that it handles the occlusion of directional components gracefully, because the size of the parameter peaks is directly proportional to the number of matching points of the component.

The Hough transform also has the feature that it is robust to the addition of random pixels from poor segmentation, because random image points are unlikely to contribute coherently to a single point in the parameter space.



8.6.2 The Hough and Radon transforms combined

The Hough transform may be viewed as a special case of the Radon transform but with a different transform origin, and performed on a binary image.

Typically, the Radon transform is defined with its transform origin at the center of the original image;

the Hough transform is defined with its transform origin at the location of the image where the row and column indices are zero.

Thus, the distance ρ as in Equation 8.42 for a 256×256 image for the Hough transform is calculated relative to the $(0, 0)$ point in the image, whereas, for the Radon transform, the ρ value is calculated relative to the $(128, 128)$ point; see Figure 8.14.



In the method proposed by Rangayyan and Rolston, a Hough-Radon hybrid transform is computed by updating the (ρ_i, θ_i) parameter point by adding the pixel intensity and not by incrementing by one as with the Hough transform.

Brighter lines correspond to larger peaks in the Hough-Radon domain.

The Hough-Radon space is indexed from 0° to 180° along one axis, and from $-N$ to $M\sqrt{2} + N\sqrt{2}$ for an image with M rows and N columns, as shown in Figure 8.17.

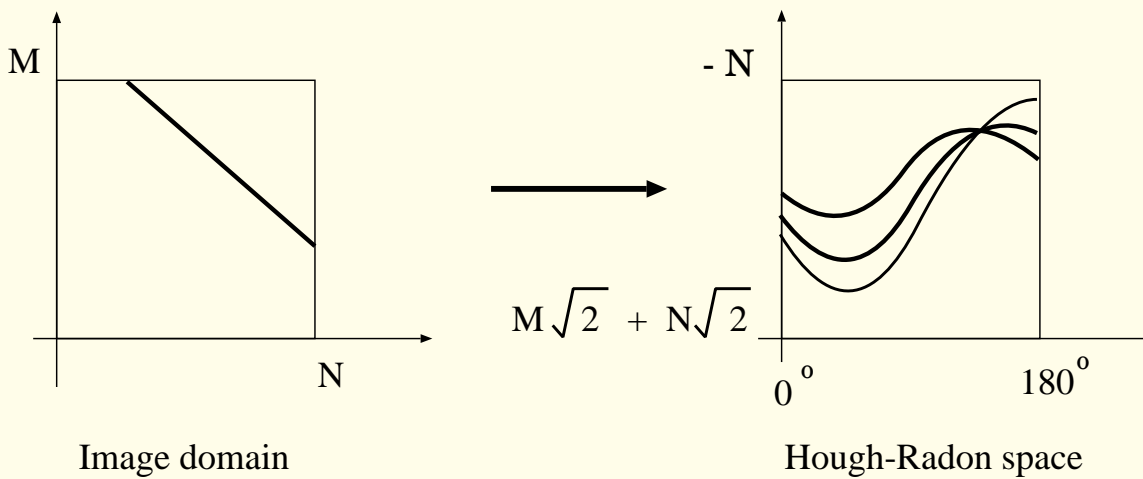


Figure 8.17: Mapping of a straight line from the image domain to the Hough-Radon space. Reproduced with permission from R.M. Rangayyan and W.A. Rolston, “Directional image analysis with the Hough and Radon transforms”, *Journal of the Indian Institute of Science*, 78: 17–29, 1998. © Indian Institute of Science.



The generation of the Hough-Radon space produces relative intensities of the directional features in the given image.

Figure 8.18: example of the Hough-Radon space for a simple test pattern.

In directional analysis, it would be of interest to obtain the number of pixels or the percentage of the image area covered by linear segments within a particular angle band.

Therefore, it is necessary to form a shadow parameter space with the numbers of the pixels that are in a particular cell in the parameter space.

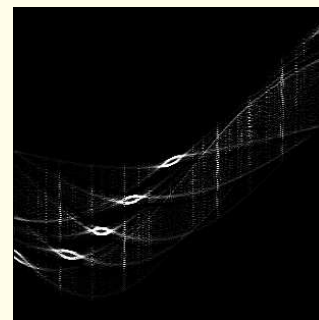
The shadow parameter space is the Hough transform of the image with no accompanying threshold.



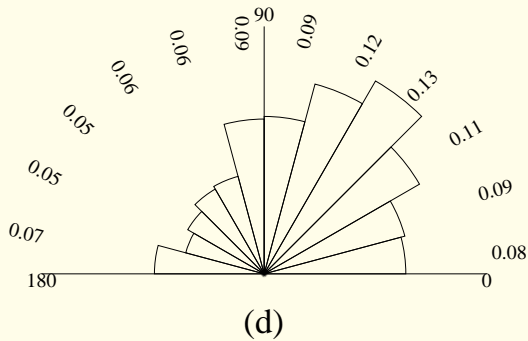
(a)



(b)



(c)



(d)

Figure 8.18: (a) A test image with five line segments. (b) The Hough-Radon space of the image. (c) Filtered Hough-Radon space. (d) Rose diagram of directional distribution. See also Figure 8.17. Reproduced with permission from R.M. Rangayyan and W.A. Rolston, “Directional image analysis with the Hough and Radon transforms”, *Journal of the Indian Institute of Science*, 78: 17–29, 1998. © Indian Institute of Science.



From the result shown in Figure 8.18 (b), we can see the high level of crosstalk in the upper-right quadrant.

From Figure 8.17, we see that this section maps to the angle band $[100^\circ, 165^\circ]$.

This is due to the Hough transform's tendency to identify several lines of varying orientation within a broad linear segment, as illustrated in Figure 8.16:

this is both a strength and a weakness of the Hough transform.

A filtering procedure may be used to reduce this effect.



8.6.3 Filtering and integrating the Hough-Radon space

The Hough-Radon transform lacks the means to eliminate elements that do not contribute coherently to a particular directional pattern.

Leavers and Boyce proposed a 3×3 filter to locate maxima in the Hough space that correspond to connected collinearities in an “edge image” space.

The filter is derived from the (ρ, θ) parameterization of lines and the expected shape of the distribution of counts in the accumulator of the Hough space.



For a linear element in an image, the expected shape is a characteristic “butterfly”; see Figure 8.17.

It was shown by Leavers and Boyce that, for any line in the image space, the extent of the corresponding butterfly in the Hough domain is limited to one radian or approximately 58° of the corresponding focal accumulator point.



$$\begin{bmatrix} 0 & -2 & 0 \\ 1 & +2 & 1 \\ 0 & -2 & 0 \end{bmatrix}. \quad (8.44)$$

This filter provides a high positive response to a distribution that has its largest value at the focal point, and falls off to approximately 50% on either side, and vanishes rapidly above and below the focal point.

A drawback of this filter is that it was designed for detecting peaks in the Hough space corresponding to lines of one pixel width.



In the example shown in Figure 8.18 (b), we can see that the broad directional components in the test image correspond to broad peaks in the Hough-Radon domain.

This results in the filter of Equation 8.44 detecting only the edges of the peaks in the Hough domain; an example of this effect is shown in Figure 8.18 (c).

The filter in Equation 8.44 is also sensitive to quantization of the θ increments.

This can be seen in the vertical streaks of intensity in Figure 8.18 (c).



In the method proposed by Rangayyan and Rolston, the Hough-Radon transform is first filtered using the filter in Equation 8.44.

The result is normalized to the range of 0.0 to 1.0 and then multiplied, point-by-point, with the shadow Hough transform.

This step is performed in order to obtain the relative strength of the numbers of pixels at each of the detected peaks.

This step also reduces the accumulated quantization noise from the Hough-Radon transformation and the filtering steps.



The final integration step is a simple summation along each of the columns of the filtered parameter space.

The Hough transform generates a parameter space that is indexed in the column space from 0° to 180° .

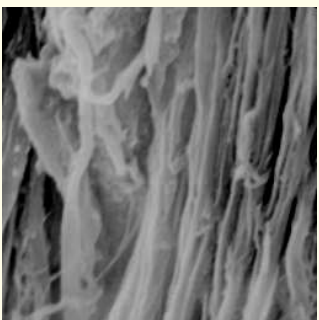
Each of the columns represents a fraction of a degree depending upon the quantization interval selected for the transform.

Because the Hough transform is a voting process, the peaks selected will contain some percentage of the pixels that are contained in the directional components.

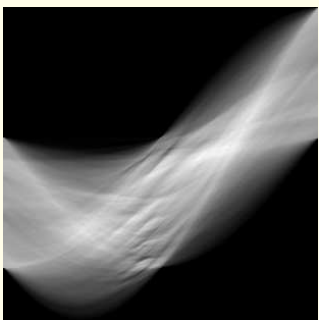


Examples: Figures 8.18 and 8.19.

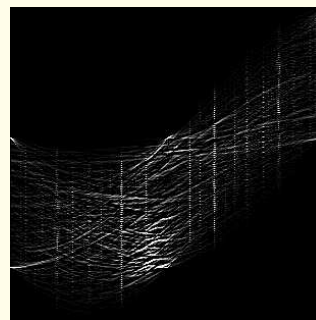
Rangayyan and Krishnan applied the Hough-Radon transform for the identification of linear, sinusoidal, and hyperbolic frequency-modulated components of signals in the time-frequency plane.



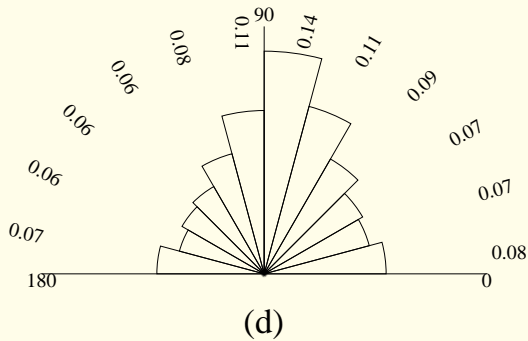
(a)



(b)



(c)



(d)

Figure 8.19: (a) An SEM image of a normal ligament with well-aligned collagen fibers. (b) The Hough-Radon space of the image. (c) Filtered Hough-Radon space. (d) Rose diagram of directional distribution. See also Figure 8.17. Reproduced with permission from R.M. Rangayyan and W.A. Rolston, “Directional image analysis with the Hough and Radon transforms”, *Journal of the Indian Institute of Science*, 78: 17–29, 1998. © Indian Institute of Science.



8.7 Application: Analysis of Ligament Healing

Ligaments are highly organized connective tissues that stabilize joints.

Ligaments normally consist of nearly parallel arrangements of collagen fibers that are attached to bone on both sides of a joint, serve to guide the joint through its normal motions, and prevent its surfaces from becoming separated.



Injuries to ligaments are common, with the normal, highly structured tissue being replaced by relatively disordered scar tissue.

The loose meshwork of the scar may not be able to resist tensile loads within the same limits of movement and deformation as a normal ligament.

The injured or healing joint, therefore, may become loose or unstable.



A critical factor thought to be important for the healing of a ligament is its blood supply, which exchanges oxygen, nutrients, and proteins with ligament tissue.

Blood vessels in the normal (uninjured) ligament tissue proper appear sparse, and are oriented parallel to the long axis of the ligament in an organized fashion,

whereas blood vessels in the normal epiligament appear more abundant, and are oriented in a less organized fashion.



In scar tissue soon after ligament injury, blood vessels have been described to be larger, more abundant, and more disorganized.

The need for a greater supply of materials to the ligament for early healing apparently leads to the formation of many new blood vessels,

but with longer term maturation of healing tissue, the vascular supply decreases and vascularity may eventually return to normal.



8.7.1 Analysis of collagen remodeling

Chaudhuri et al., Frank et al., and Liu et al. studied collagen alignment in SEM images of the medial collateral ligament (MCL) of the rabbit knee.

Directional analysis was performed using the sector-filtering methods described in Section 8.3.1.

Directional components were obtained over 12 angle bands spanning the full range of $[0^\circ, 180^\circ]$.

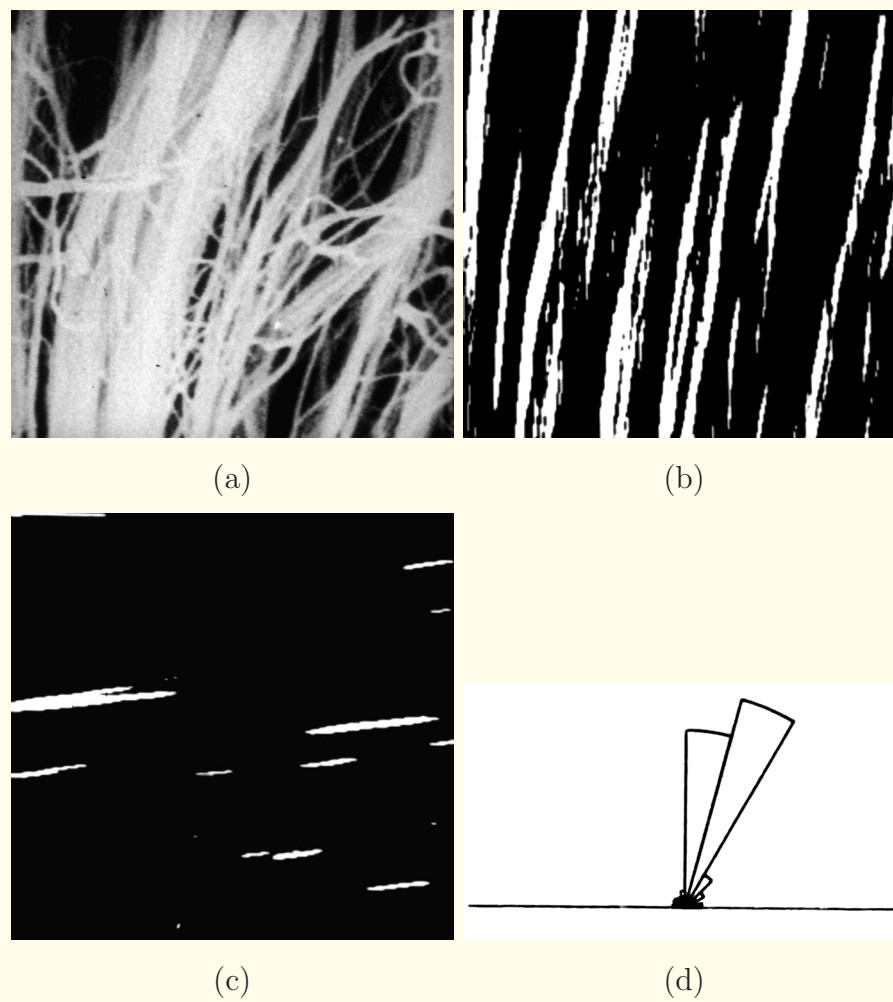


Figure 8.20: (a) A sample image showing collagen alignment in a normal ligament. Binarized directional components in the angle band (b) $75^\circ - 90^\circ$, and (c) $0^\circ - 15^\circ$. (d) Fractional fiber-covered areas in the form a rose diagram. Figure courtesy of S. Chaudhuri.

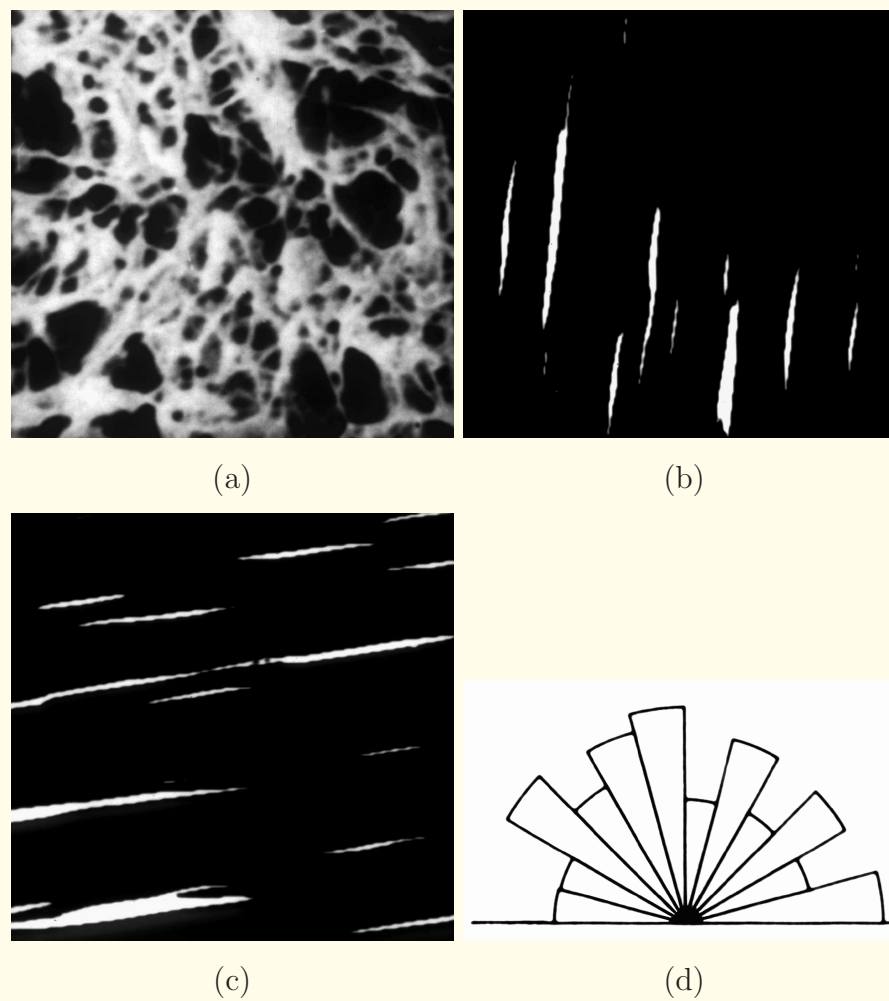


Figure 8.21: (a) A sample image showing collagen alignment in ligament scar tissue. Binarized directional components in the angle band (b) $75^\circ - 90^\circ$, and (c) $0^\circ - 15^\circ$. (d) Fractional fiber-covered areas in the form a rose diagram. Figure courtesy of S. Chaudhuri.

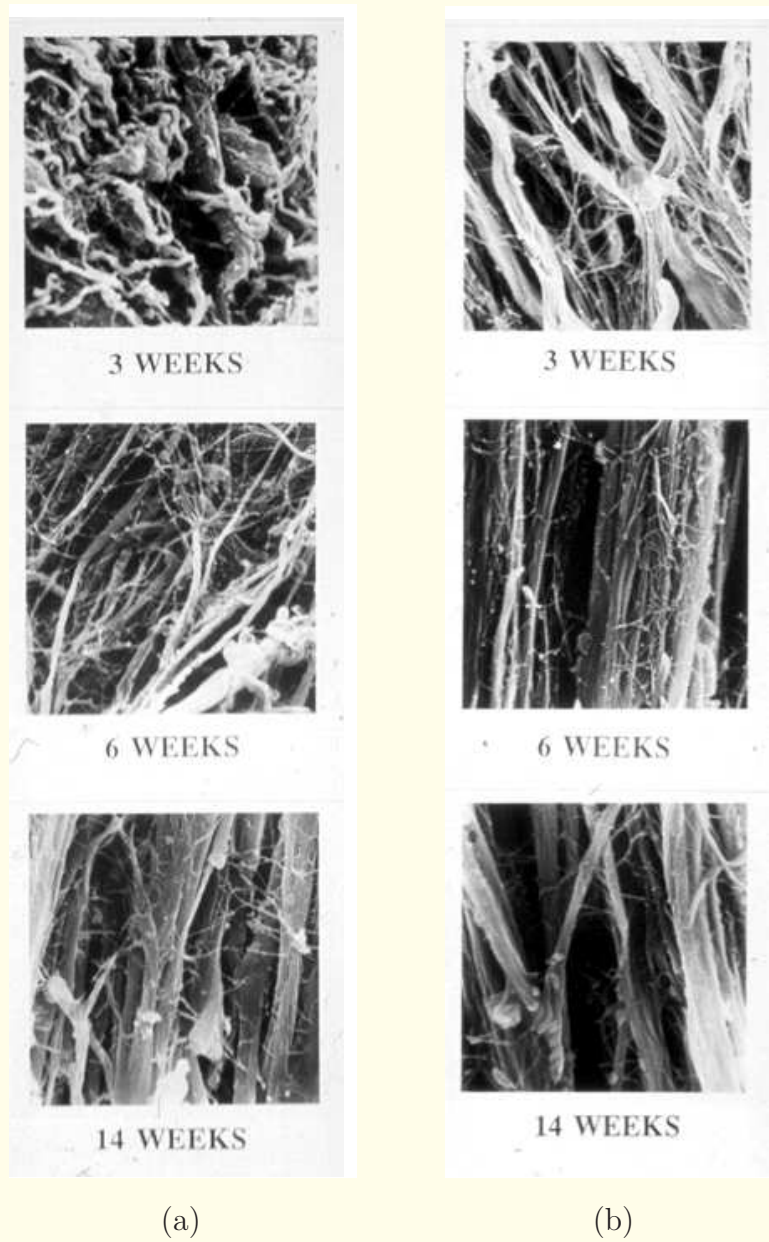


Figure 8.22: Sample images showing collagen alignment in ligament samples at three weeks, six weeks, and 14 weeks after injury: (a) without immobilization of the affected joint, (b) with immobilization of the affected joint for three weeks. Images courtesy of C.B. Frank. See also Figure 8.23.

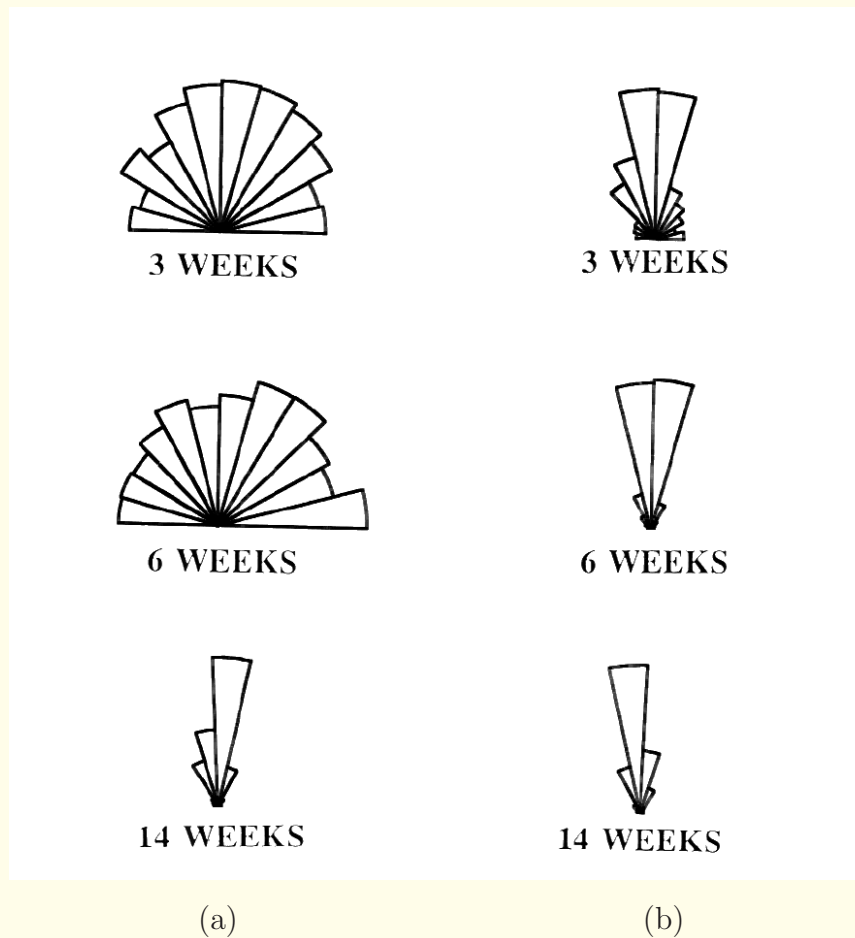


Figure 8.23: Composite rose diagrams showing collagen realignment in ligament samples at three weeks, six weeks, and 14 weeks after injury: (a) without immobilization of the affected joint, (b) with immobilization of the affected joint for three weeks. See also Figure 8.22. Reproduced with permission from C.B. Frank, B. MacFarlane, P. Edwards, R. Rangayyan, Z.Q. Liu, S. Walsh, and R. Bray, "A quantitative analysis of matrix alignment in ligament scars: A comparison of movement versus immobilization in an immature rabbit model", *Journal of Orthopaedic Research*, 9(2): 219 – 227, 1991. © Orthopaedic Research Society.

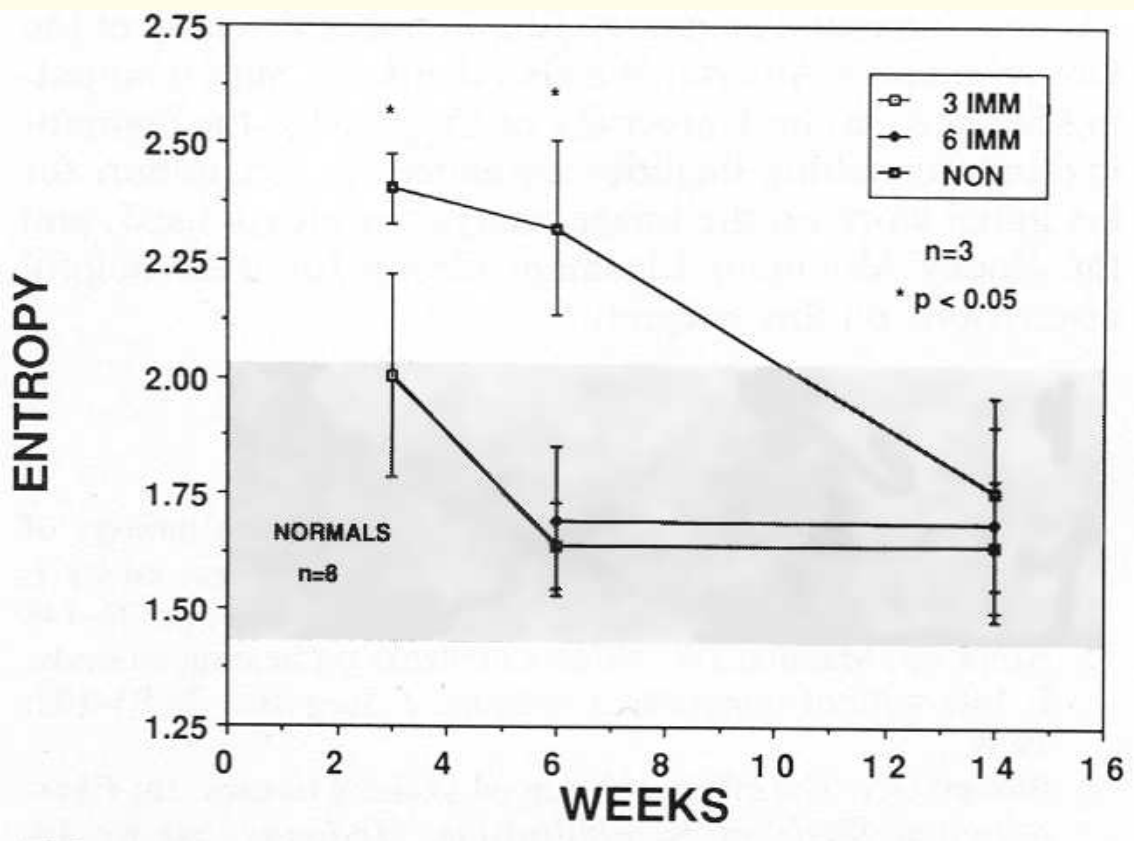


Figure 8.24: Variation of the entropy of composite rose diagrams with collagen realignment in ligament samples at three weeks, six weeks, and 14 weeks after injury. The vertical bars indicate \pm one standard deviation about the corresponding means. “NON”: without immobilization of the affected joint; “3 IMM”: with immobilization of the affected joint for three weeks; “6 IMM”: with immobilization of the affected joint for six weeks. The shaded region indicates the range of entropy for normal ligament samples. See also Figures 8.23 and 8.22. Reproduced with permission from C.B. Frank, B. MacFarlane, P. Edwards, R. Rangayyan, Z.Q. Liu, S. Walsh, and R. Bray, “A quantitative analysis of matrix alignment in ligament scars: A comparison of movement versus immobilization in an immature rabbit model”, *Journal of Orthopaedic Research*, 9(2): 219 – 227, 1991. © Orthopaedic Research Society.



The results demonstrate a reduction in entropy, indicating a return to orderly structure, as the healing time increases.

Immobilization of the affected joint for three weeks after injury resulted in entropy values that are close to the values at 14 weeks in all cases, and well within the range for normal ligaments (the shaded region in Figure 8.24).

The results indicate that immobilization of the affected joint for three weeks promotes the healing process, and that immobilization for the longer period of six weeks does not provide any further advantage.

The results provide important quantitative information that can assist in the understanding of ligament structure and healing.



8.7.2 *Analysis of the microvascular structure*

Eng et al. performed directional analysis of microscope images of ink-stained blood vessels in the rabbit MCL.

The normal ligament is relatively avascular; the blood vessels that exist are aligned along the length of the ligament.

Scar tissue has a more abundant network of blood vessels to facilitate the healing process, with extensive branching and lack of preferred orientation.

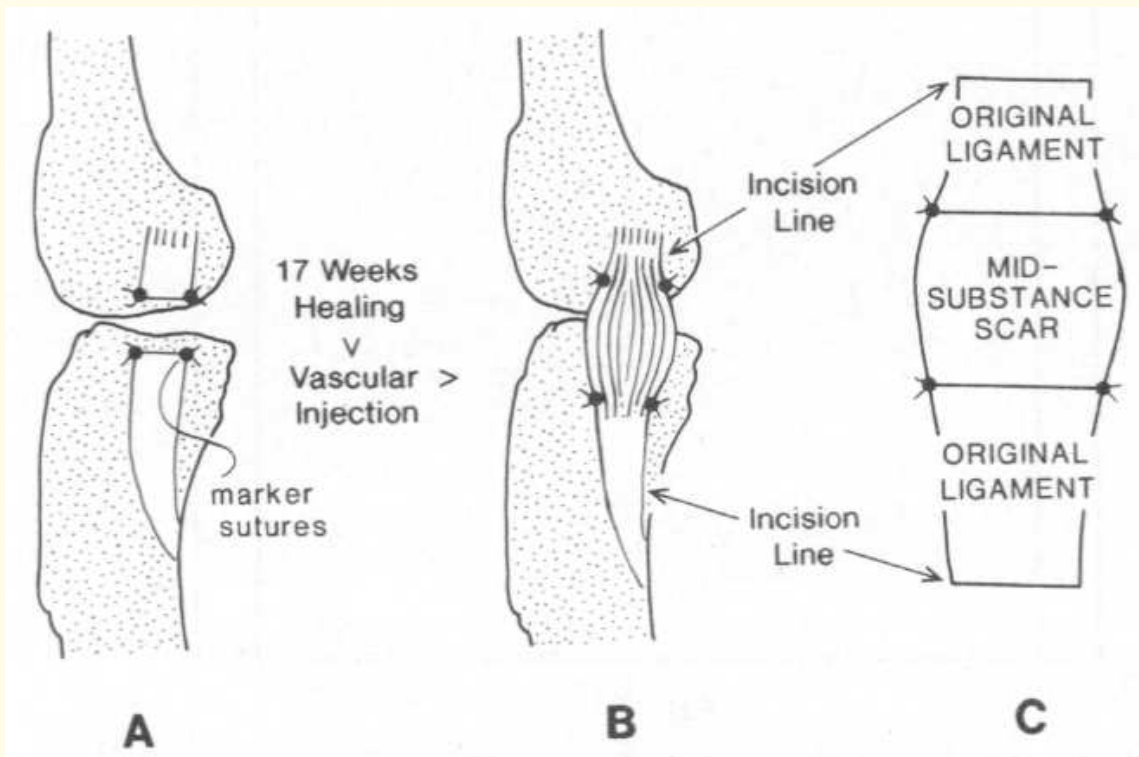


Figure 8.25: Gap-injury site in the ligament and the formation of scar. A: Gap injury created by removing a 4 mm section of the MCL. B: Scar after healing. C: Extracted ligament and its main regions. See also Figure 8.26. Reproduced with permission from K. Eng, R.M. Rangayyan, R.C. Bray, C.B. Frank, L. Anscomb, and P. Veale, “Quantitative analysis of the fine vascular anatomy of articular ligaments”, *IEEE Transactions on Biomedical Engineering*, 39(3): 296 – 306, 1992. © IEEE.

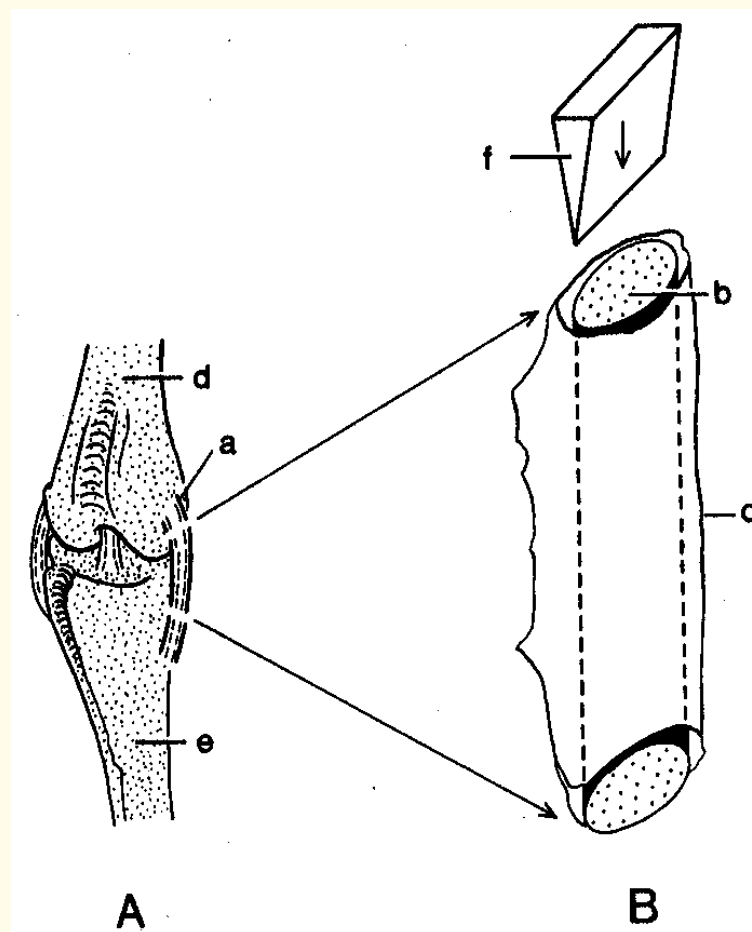
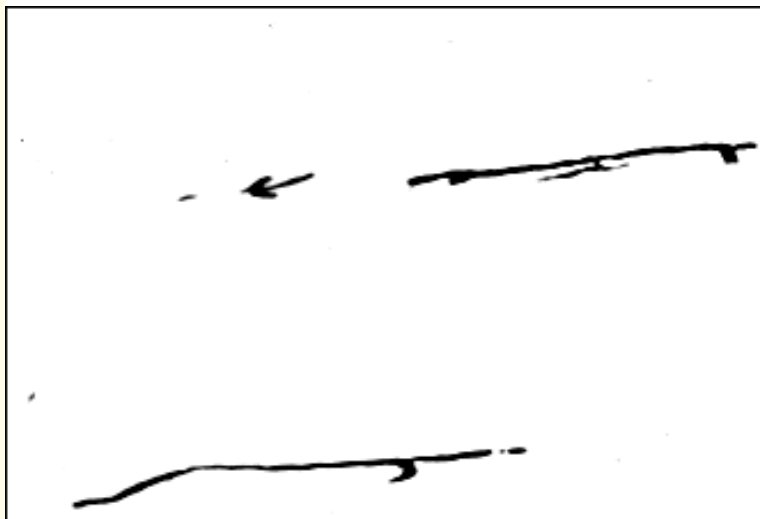


Figure 8.26: Ligament sectioning procedure for the imaging of vascular anatomy. A: knee joint. B: Extracted ligament and plane of sectioning. a: MCL complex. b: Ligament. c: Epiligament. d: Femur. e: Tibia. f: Sectioning (imaging) plane. See also Figure 8.25. Reproduced with permission from K. Eng, R.M. Rangayyan, R.C. Bray, C.B. Frank, L. Anscomb, and P. Veale, "Quantitative analysis of the fine vascular anatomy of articular ligaments", *IEEE Transactions on Biomedical Engineering*, 39(3): 296 – 306, 1992. © IEEE.



(a)



(b)

Figure 8.27: Microvascular structure in ligaments: (a) normal; (b) 17-week scar. Images courtesy of R.C. Bray.



Binarization of the images:

The gray-level histogram for a blood-vessel image was assumed to be bimodal, with the first peak representing the pixels of blood vessels, and the second one representing the background pixels.

Otsu's method (see Section 8.3.2) for threshold selection produced binary images with excessive artifacts.

Histogram concavity analysis locates the locally significant minima and maxima in the gray-level histogram of the image and produces a list of possible thresholds.

It was difficult to choose the threshold to use from the list.



The Rutherford–Appleton threshold-selection algorithm computes a threshold by using the gradient of the image.

The best threshold for the binarization of the blood-vessel images was obtained by using the Rutherford–Appleton algorithm to get a threshold estimate,

followed by histogram concavity analysis to fine tune the final threshold value.



The derivatives of the given image $f(m, n)$ were obtained in the x and y directions as

$$d_x(m, n) = f(m, n + 1) - f(m, n - 1), \quad (8.45)$$

$$d_y(m, n) = f(m + 1, n) - f(m - 1, n). \quad (8.46)$$

The larger of the two derivatives was saved as

$$d(m, n) = \max[|d_x(m, n)|, |d_y(m, n)|]. \quad (8.47)$$



Two sums were computed over the entire image as

$$S_d = \sum \sum d(m, n), \quad (8.48)$$

$$S_{df} = \sum \sum d(m, n) f(m, n). \quad (8.49)$$

The Rutherford–Appleton threshold is given as

$$T_o = \frac{S_{df}}{S_d}. \quad (8.50)$$



Another potential threshold was determined by finding the position of maximal histogram concavity.

A typical gray-level histogram consists of a number of significant peaks (local maxima) and valleys (local minima).

Significant peaks may be identified by constructing a convex hull of the histogram, which is defined as the smallest convex polygon $\bar{h}(l)$ containing the given histogram $h(l)$.

The convex hull consists of straight-line segments joining the significant peaks in the histogram.



The histogram concavity at any gray level is defined as the vertical distance between the convex hull and the histogram: $[\bar{h}(l) - h(l)]$.

Within each straight-line segment of the convex hull, the gray level at which the maximal concavity occurred was labeled as the optimal threshold for that segment.

Because the area covered by the blood vessels is small compared to the area covered by the background in the ligament section images, the gray-level histogram was first scaled logarithmically to make the histogram peak representing the blood vessels and the background peak closer in height.

A convex polygon of the scaled histogram was then constructed.



The problem of choosing between the thresholds of each of the segments of the convex polygon was addressed by finding a threshold T_o using the Rutherford–Appleton algorithm.

The threshold estimate T_o was found to lie between the background peak and the peak representing the blood-vessel pixels.

The threshold representing the maximal histogram concavity within the convex hull segment joining these two peaks was chosen to be the threshold value T_c .



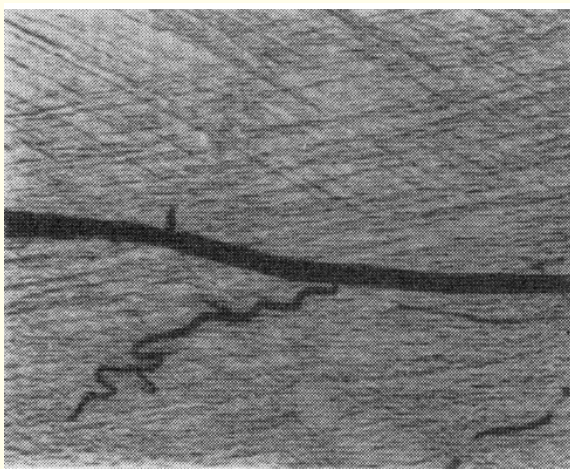
A threshold was also determined by finding the minimum point in the histogram between the peaks that represented the blood-vessel and background pixels.

This threshold, T_m , yielded a smaller value than T_c because of the height difference between the peaks.

T_c was often too high, resulting in an image with artifacts.

T_m was often too low, resulting in the loss of blood-vessel pixels.

Compromise: average of T_c and T_m .



(a)



(b)

Figure 8.28: Microvascular structure in a normal ligament sample. (a) original image; (b) binarized image. See Figure 8.29 for details on the selection of the threshold for binarization. Reproduced with permission from K. Eng, R.M. Rangayyan, R.C. Bray, C.B. Frank, L. Anscomb, and P. Veale, “Quantitative analysis of the fine vascular anatomy of articular ligaments”, *IEEE Transactions on Biomedical Engineering*, 39(3): 296 – 306, 1992. © IEEE.

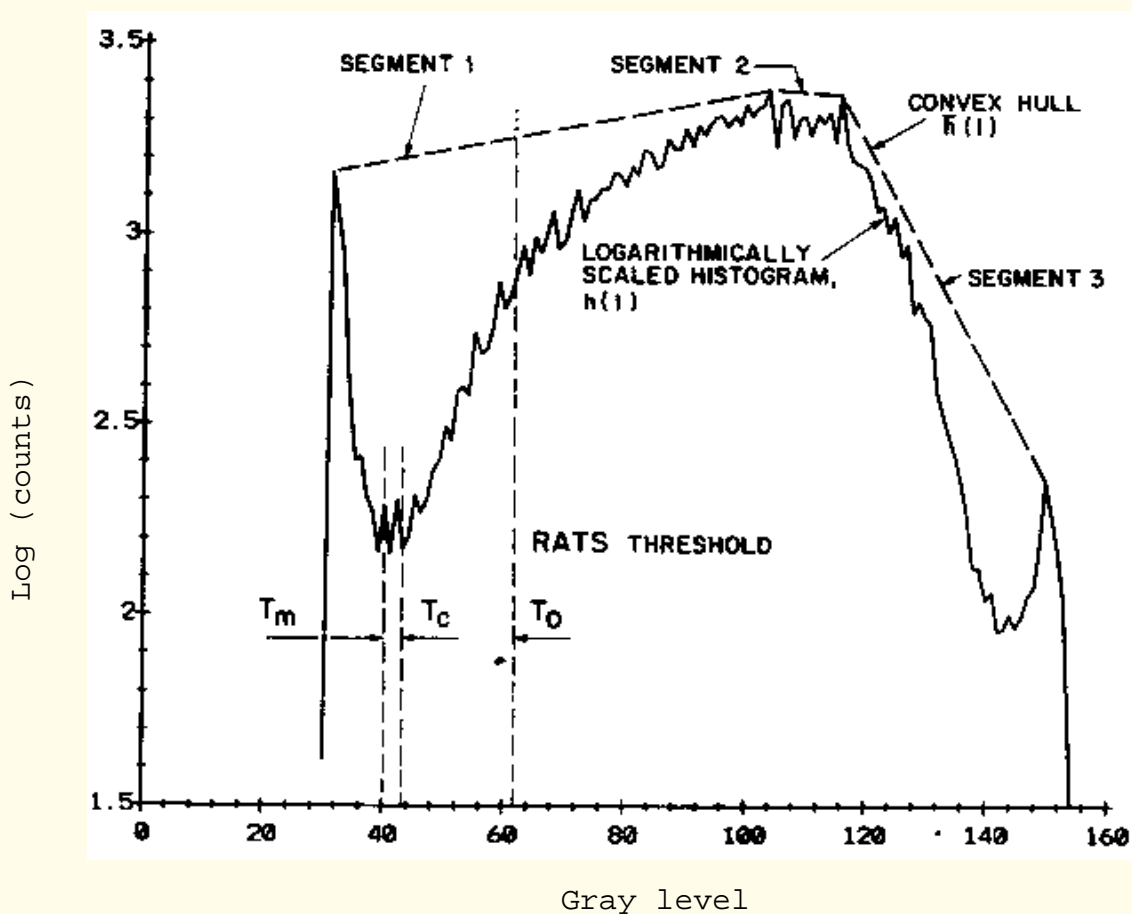


Figure 8.29: Logarithmically scaled histogram of the image in Figure 8.28 (a), along with its convex hull and several possible thresholds for binarization. RATS: Rutherford–Appleton threshold-selection algorithm. Reproduced with permission from K. Eng, R.M. Rangayyan, R.C. Bray, C.B. Frank, L. Anscomb, and P. Veale, “Quantitative analysis of the fine vascular anatomy of articular ligaments”, *IEEE Transactions on Biomedical Engineering*, 39(3): 296 – 306, 1992. © IEEE.



Skeletonization:

Skeletonization makes directional analysis easier by reducing the binary blood-vessel patterns to their skeletal patterns with one-pixel-thick lines (see Section 6.1.6).

In order to assist the analysis of both the directionality and the volume of vascularization, an image array containing the diameter of the blood vessel at each skeleton point was formed, and referred to as the diameter-proportional skeleton of the image.



The diameter at a skeleton point s_i was obtained as

$$\phi(x, y) = 2 \times \min[D(s_i, C)], \quad (8.51)$$

where C is the set of contour points of the binary image before skeletonization, and D is the Euclidean distance.

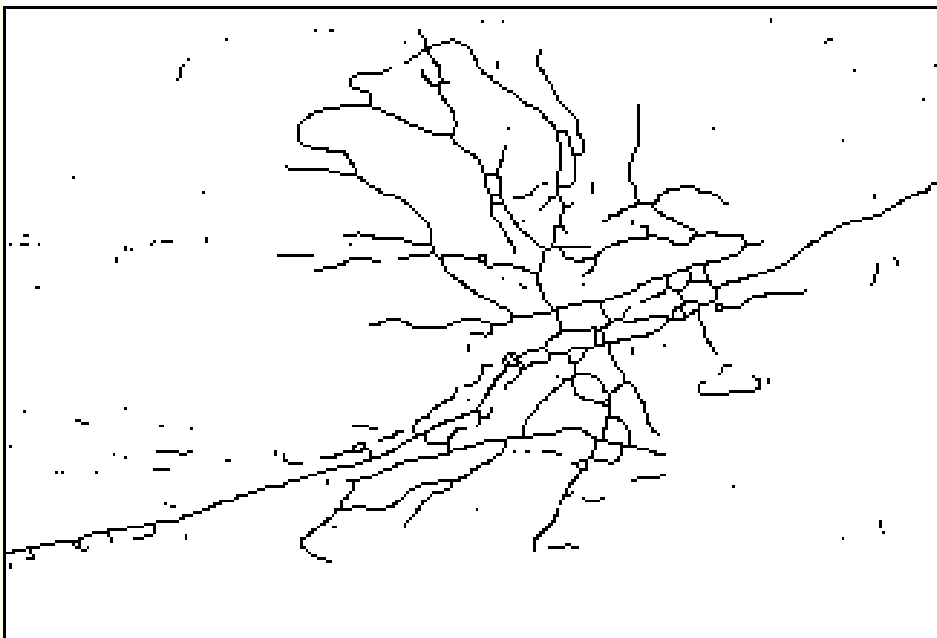


Figure 8.30: Skeleton of the image in Figure 8.27 (b). See also Figure 6.13.



Directional analysis:

Skeletonization allows the use of the simple method of least-squares linear regression to determine the angle of orientation of each blood-vessel segment in the image.

From each point (x, y) in the skeleton image, a line segment consisting of $N = 11$ points was extracted, with the center point located at (x, y) .

If (x_i, y_i) , $i = 1, 2, \dots, N$, represent the points in the line segment, the slope of the best-fitting straight line is

$$m = \frac{\sum_{i=1}^N x_i \sum_{i=1}^N y_i - \sum_{i=1}^N (x_i y_i)}{\left[\sum_{i=1}^N x_i \right]^2 - \sum_{i=1}^N (x_i)^2}. \quad (8.52)$$



When the slope becomes large for a nearly vertical line segment, slope estimation as above becomes inaccurate due to increasing y -axis errors.

This error can be obviated by adapting the least-squares formula to minimize the x -axis errors if the slope found by Equation 8.52 is greater than unity.

The inverse of the slope is then given by

$$\frac{1}{m} = \frac{\sum_{i=1}^N x_i - \sum_{i=1}^N (x_i y_i)}{\left[\sum_{i=1}^N y_i \right]^2 - \sum_{i=1}^N (y_i)^2}. \quad (8.53)$$

The angle of the skeleton at the point (x, y) is then given by $\theta = \arctan(m)$.



The elemental area of the blood vessel at the point (x, y) is

$$A(x, y) = \phi(x, y) W(\theta), \quad (8.54)$$

where $\phi(x, y)$ is the vessel thickness at (x, y) as given by Equation 8.51, and

$$W(\theta) = \begin{cases} \frac{1}{\cos(\theta)} & \text{if } |\theta| < 45^\circ \\ \frac{1}{\sin(\theta)} & \text{if } |\theta| > 45^\circ \end{cases}. \quad (8.55)$$

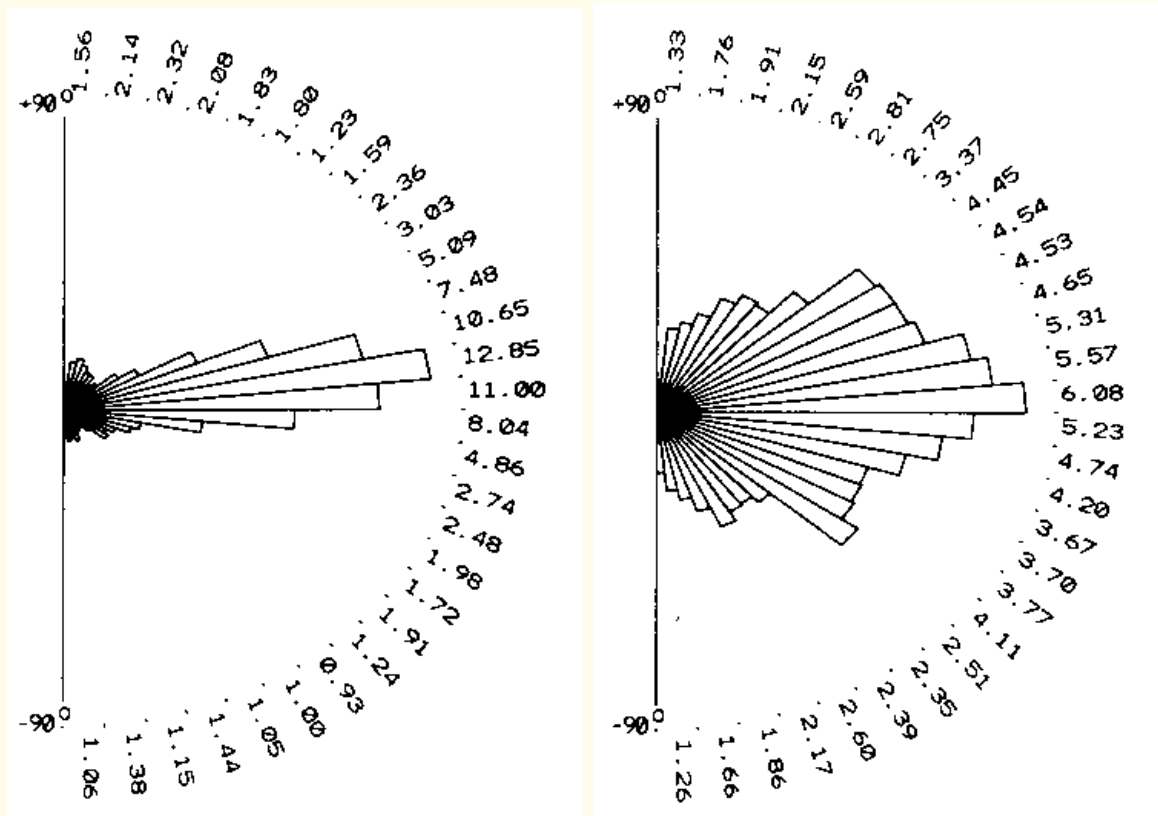


The factor W as above (in pixels), accounts for the fact that diagonally connected pixels are farther apart than vertically or horizontally connected pixels.

The elemental area was added to the corresponding angle of the histogram, and the process repeated for all points in the skeleton.

The overall accuracy of the directional analysis procedure as above was estimated to be $\pm 3^\circ$ by analyzing various test patterns.

For this reason, the blood-vessel angular distributions were computed in bins of width 6° .



(a)

(b)

Figure 8.31: Angular distributions of blood vessels in (a) normal ligaments (averaged over 82 images from four ligaments), and (b) 17-week scar tissues from three ligaments (115 images). Reproduced with permission from K. Eng, R.M. Rangayyan, R.C. Bray, C.B. Frank, L. Anscomb, and P. Veale, “Quantitative analysis of the fine vascular anatomy of articular ligaments”, *IEEE Transactions on Biomedical Engineering*, 39(3): 296 – 306, 1992. © IEEE.



In addition to the directional distributions and their statistics (entropy and angular dispersion or standard deviation), the relative volume of blood vessels in the various ligament samples analyzed were computed; see Table 8.2.

Using the two-sample t-test, several assertions were arrived at about the relative volume and organization of blood vessels in normal and healing ligaments; see Table 8.3.

Statistical analysis of the results indicated, with 96% confidence, that 17-week scars contain a greater volume of blood vessels than normal ligaments.

Using entropy as a measure of chaos in the angular distribution of the blood-vessel segments, statistical analysis indicated, with 99% confidence, that blood vessels in 17-week scars are more chaotic than in normal ligaments.



Table 8.2: Measures of Entropy and Standard Deviation (SD) of Composite Angular Distributions of Blood Vessels in Ligaments.

Tissue type	Ligaments	Images	Entropy	SD (°)	% Vasc.
NORMAL:					
Ligament	4	82	4.39	36.10	0.98
Epiligament	4	20	4.64	38.53	1.19
CONTRALATERAL:					
Ligament	3	93	4.33	34.79	1.05
Epiligament	3	36	4.79	42.98	2.40
SCAR:					
	3	115	4.79	42.52	2.50
ENDS:					
Ligament	3	80	4.59	36.55	2.24
Epiligament	3	20	4.78	44.08	3.10

The maximum possible value for entropy is 4.91. ‘SCAR’: midsubstance scar; ‘ENDS’: original ligament ends; see Figures 8.26 and 8.25. ‘% Vasc.’: percentage of the analyzed tissue volume covered by the blood vessels detected. Reproduced with permission from K. Eng, R.M. Rangayyan, R.C. Bray, C.B. Frank, L. Anscomb, and P. Veale, “Quantitative analysis of the fine vascular anatomy of articular ligaments”, *IEEE Transactions on Biomedical Engineering*, 39(3): 296 – 306, 1992. © IEEE.



Table 8.3: Results of Statistical Comparison of the Relative Volume of Vascularization (V) and the Entropy of the Angular Distribution (H) of Various Ligament Samples.

Assertion	Confidence (%)
LIGAMENT:	
V (normal) < V (contralateral)	70
V (normal) < V (midsubstance scar)	96
V (normal) < V (original ligament ends)	85
V (original ligament ends) < V (midsubstance scar)	55
H (contralateral) < H (normal)	73
H (normal) < H (midsubstance scar)	99
H (normal) < H (original ligament ends)	53
H (original ligament ends) < H (midsubstance scar)	96
EPILIGAMENT:	
V (normal) < V (contralateral)	99
V (normal) < V (original ligament ends)	70
H (normal) < H (contralateral)	90
H (normal) < H (original ligament ends)	82

Reproduced with permission from K. Eng, R.M. Rangayyan, R.C. Bray, C.B. Frank, L. Anscomb, and P. Veale, “Quantitative analysis of the fine vascular anatomy of articular ligaments”, *IEEE Transactions on Biomedical Engineering*, 39(3): 296 – 306, 1992. © IEEE.



A factor that affects the accuracy in the angular distributions derived as above is the width of the blood vessels.

As the thickness of a blood vessel increases, more material is lost at the ends of the vessels during skeletonization.

This loss, although corrected for by the addition of semicircular end pieces, could lead to reduced accuracy of the angular distribution.

Sampling and quantization errors become significant when the thickness of blood vessels is small.

The sectioning procedure used to obtain 2D slices imposes a limitation: segments of the blood vessels that traverse across the sectioning planes are lost.



8.8 Application: Detection of Breast Tumors

The differences in the density of breast tissues are captured in a mammogram as intensity and textural variations.

Mudigonda et al. proposed an unsupervised segmentation approach to localize suspicious mass regions in mammograms.

The approach aims to isolate the spatially interconnected structures in the image to form regions concentrated around prominent intensities.

It would then be possible to extract high-level information characterizing the physical properties of mass regions, and to short-list suspicious ROIs for further analysis.

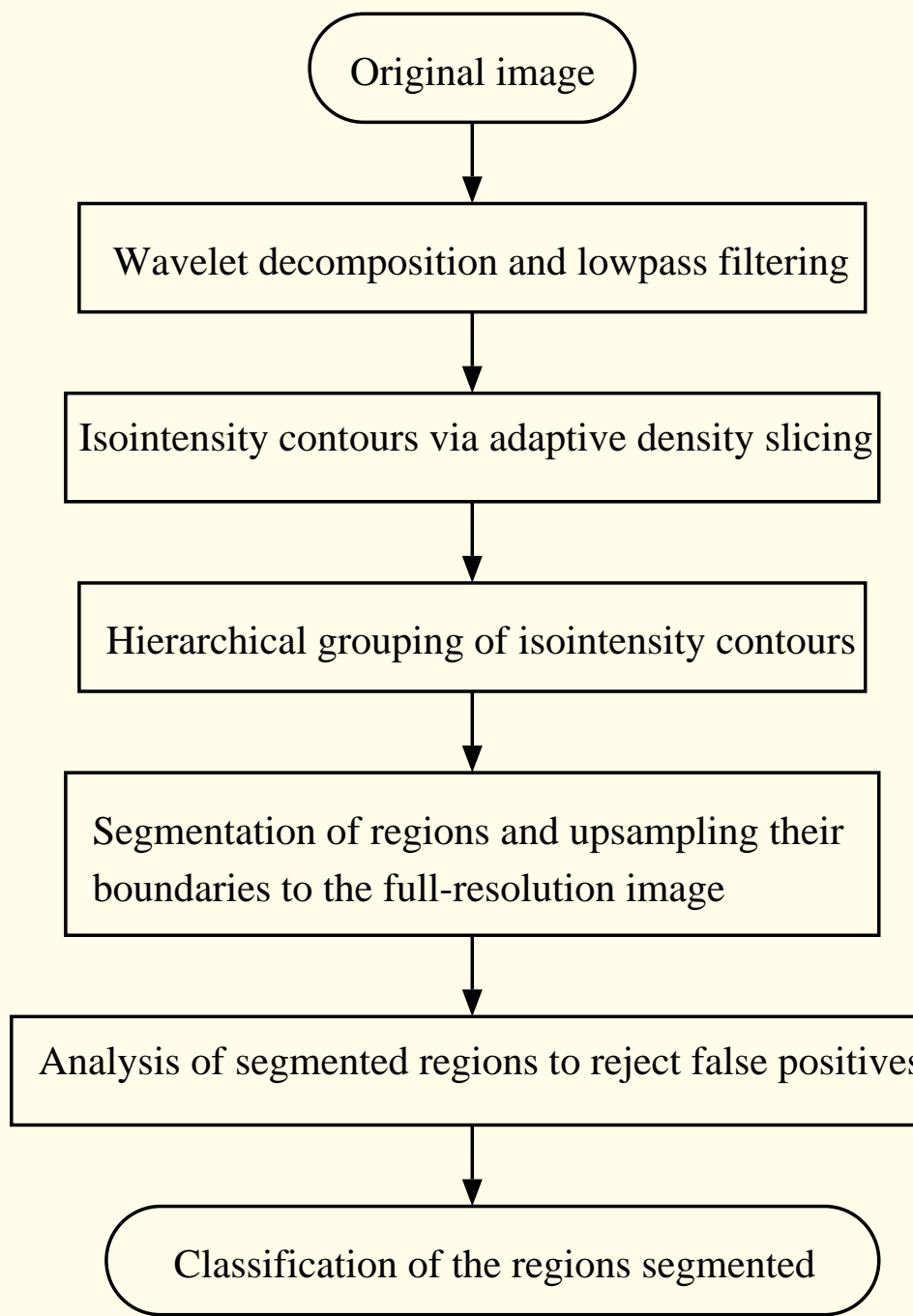


Figure 8.32: Block diagram of the mass-detection algorithm. Figure courtesy of N.R. Mudigonda.



8.8.1 *Framework for pyramidal decomposition*

Malignant tumors, due to their invasive nature, possess heterogeneous density distributions and margins causing distortion in the orientation of the surrounding tissues.

In order to detect such structures as single entities, prior smoothing of the image is required.

Mudigonda et al. employed recursive wavelet decomposition and Gaussian smoothing operations in a multiresolution pyramidal architecture as preprocessing steps to achieve the required level of smoothing of the image.



A pyramidal representation of the given image was obtained by iterative decimation operations on the full-resolution image, thereby generating a hierarchy of subimages with progressively decreasing bandwidth and increasing scale.

Wavelet decomposition divides the frequency spectrum of the original image f into its lowpass-subband-equivalent image f_L and highpass-equivalent detail image f_H at different scales.

The lowpass-subband image at each scale, produced by decimating its preceding higher-resolution image present in the hierarchy by an octave level, was further smoothed by a 3×3 Gaussian kernel, and the resulting image was stretched to the range of $0 - 60$ in pixel value.



The wavelet used was a symlet of eighth order.

Symlets are compactly supported wavelets with the least asymmetry and the highest number of vanishing moments for a given support width.

Figure 8.33 shows plots of the decomposition lowpass kernels used with symlets, at two different scales.

The wavelet decomposition was performed recursively to three octave levels using the symlets mentioned above.

The preprocessing steps of wavelet decomposition and Gaussian smoothing operations successively and cumulatively modulate the intensity patterns of mass regions to form smooth hills with respect to their surroundings in low-resolution images.

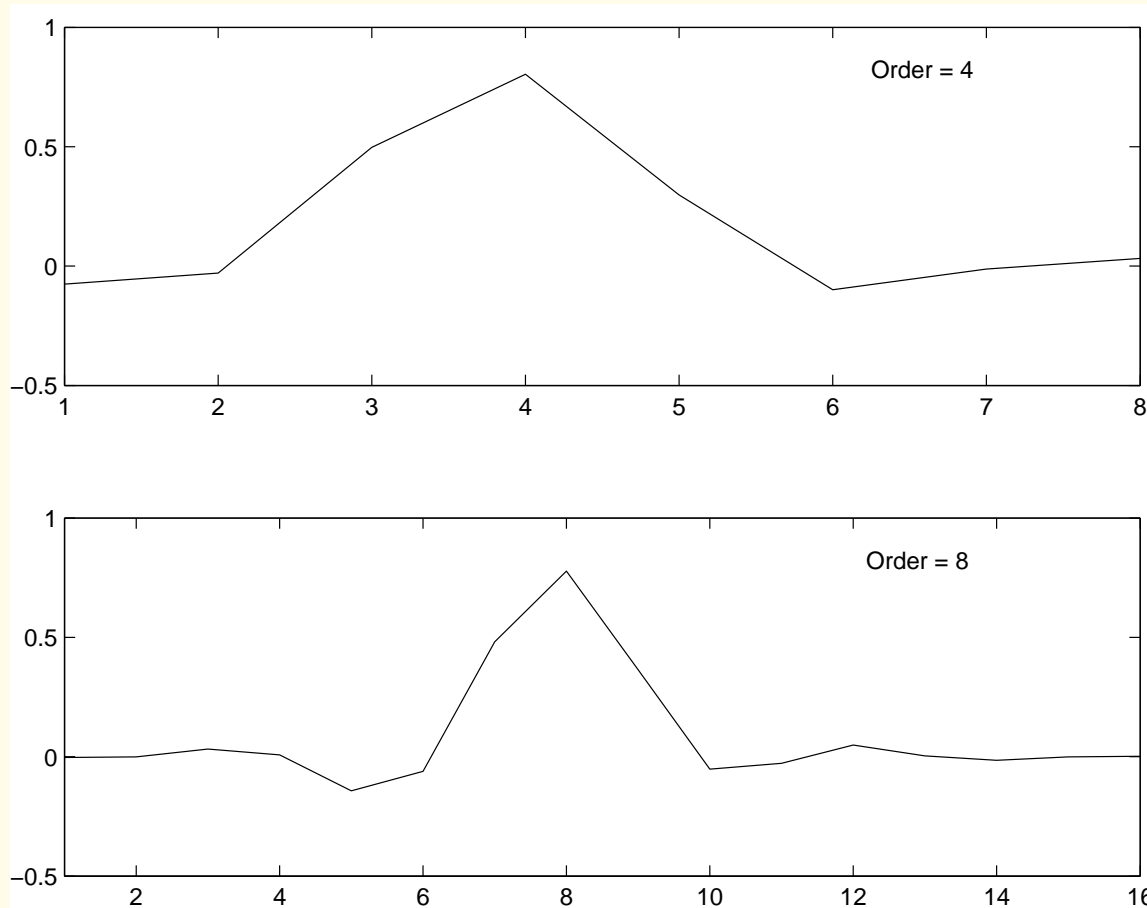


Figure 8.33: Plots of symlet decomposition lowpass filters at two scales. Figure courtesy of N.R. Mudigonda.

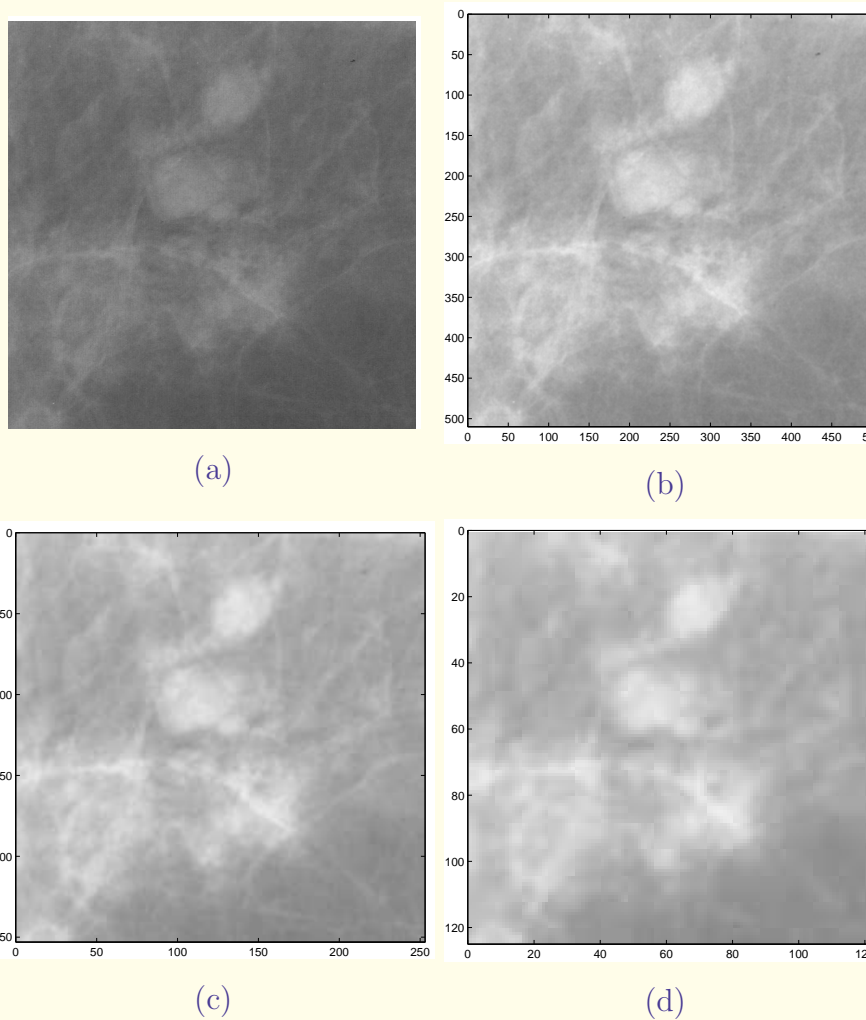


Figure 8.34: (a) A $1,024 \times 1,024$ section of a mammogram containing two circumscribed benign masses. Pixel size = $50 \mu\text{m}$. Image width = 51 mm . Low-resolution images obtained by wavelet filtering: (b) After the first level of decomposition; 512×512 pixels, $100 \mu\text{m}$ per pixel. (c) After two levels of decomposition; 256×256 pixels, $200 \mu\text{m}$ per pixel. (d) After three levels of decomposition; 128×128 pixels, $400 \mu\text{m}$ per pixel. The intensity of the filtered images has been enhanced by four times for display purposes. Figure courtesy of N.R. Mudigonda.



The choice of the wavelet, the width of the kernel used for lowpass filtering, and the degree or scale factor of decomposition can influence the smoothed results.

A scale factor of three, which causes the decomposition of the original $50 \mu\text{m}/\text{pixel}$ images to a resolution of $400 \mu\text{m}/\text{pixel}$, was found to be effective.



8.8.2 Segmentation based upon density slicing

The recursive smoothing and decimation operations result in a gradual modulation of intensity information about the local intensity maxima present in various isolated regions in the low-resolution image.

As a result, the intensity levels are expected to assume either unimodal or bimodal histogram distributions.

The next step is to threshold the image at varying levels of intensity to generate a map of isointensity contours.

The purpose of this step is to extract concentric groups of closed contours to represent the isolated regions in the image.



The density-slicing or intensity-slicing technique slices the given image (represented as a 2D intensity function) by using a plane that is placed parallel to the coordinate plane of the image.

A level curve (also known as an isointensity curve) is then formed by extracting the boundary of the area of intersection of the plane and the intensity function.

Each level curve obtained using the procedure explained above is guaranteed to be continuous and closed.

The number of levels of thresholding, starting with the maximum intensity in the image, and the step-size decrement for successive levels, were adaptively computed based upon the histogram distribution of the image under consideration.

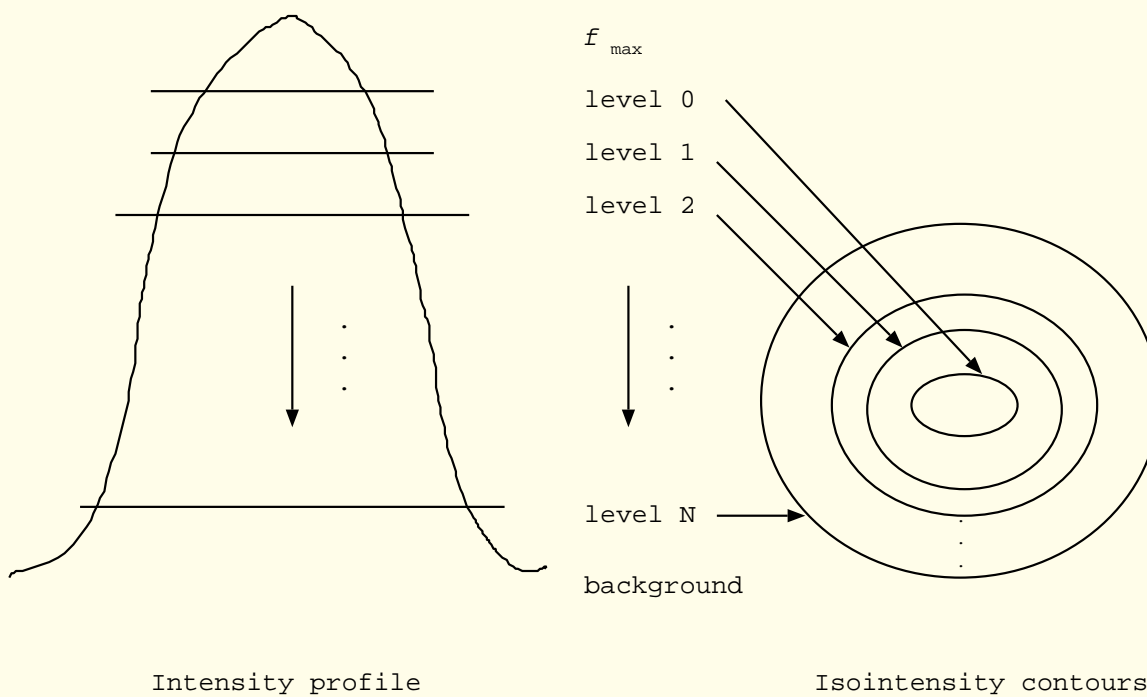


Figure 8.35: Schematic illustration of the density-slicing operation. f_{\max} represents the maximum intensity in the image, and levels $0, 1, 2, \dots, N$ represent a set of N threshold values used for density slicing. Figure courtesy of N.R. Mudigonda.



Let f_{\max} represent the maximum intensity level in the low-resolution image (which was scaled to 60).

Let f_{th} be the threshold representing the mass-to-background separation, which is to be derived from the histogram.

It is assumed that the application of the preprocessing smoothing operations results in exponentially decreasing intensity from the central core region of a mass to its background, represented as

$$f_{th} = f_{\max} \exp[-\mu N].$$



N is the number of steps required for the exponentially decreasing intensity function to attain the background level represented by f_{th} ,

$$N = (f_{\max} - f_{th}),$$

and μ is the intended variation in step size between the successive levels of thresholding.

The step size μ may be computed through a knowledge of the parameters f_{th} and N .



The threshold f_{th} was derived from the histogram, and corresponds to the intensity level representing the maximum number of occurrences when the histogram is unimodal.

It is essential to set bounds for f_{th} so as not to miss the detection of masses with low-density core regions, while maintaining the computational time of the algorithm at a reasonable level.

Initial estimates of f_{th} derived from the corresponding histograms of low-resolution images were observed to range between 50% and 90% of f_{max} .

N was observed to range between 10 and 30.

f_{th} was adaptively selected based upon the histogram.



1. If $0.5 f_{\max} < f_{th} \leq 0.9 f_{\max}$, f_{th} could be assumed to represent the mass-to-background transition, and the same threshold value is retained.
2. If $f_{th} > 0.9 f_{\max}$, the mass regions that are to be detected in the image are expected to be merged with the surrounding background, and no distinct central core regions would be present. In such cases, f_{th} is considered to be $0.9 f_{\max}$, and N is set to 30 (the maximum considered) to limit the step-size increments of the level function to a low value. These steps facilitate close tracking of difficult-to-detect mass-to-background demarcation.
3. If $f_{th} \leq 0.5 f_{\max}$, f_{th} might not represent the true mass-to-background transition, and hence, is ignored. An alternative search for f_{th} is initiated so that the value obtained will lie in the upper half of the histogram distribution.



8.8.3 Hierarchical grouping of isointensity contours

The next step is to perform grouping and elimination operations on the framework of closed contours generated in the low-resolution image, considering their parent-child nodal relations in a family-tree architecture.

The strategy adopted was to short-list at first the possible central dense-core portions, which are usually small in size but of higher density (represented by f_{\max} in each group of contours in Figure 8.36), and to identify the immediate low-density parent members encircling them.

The process was continued until all the members in the available set of closed contours in the image were visited.



Each of the closed contours was assigned to a specific group or family of concentric contours based upon nodal relations, thus leading to segmentation of the image into isolated regions.

A concentric group of contours represents the propagation of density information from the central core portion of an object in the image into the surrounding tissues.

In some images with dense and fatty backgrounds, the outermost contour members were observed to contain multiple regions of dissimilar structures.

For this reason, a specified number of outer contours were discarded to separate the groups of contours representing adjacent structures.

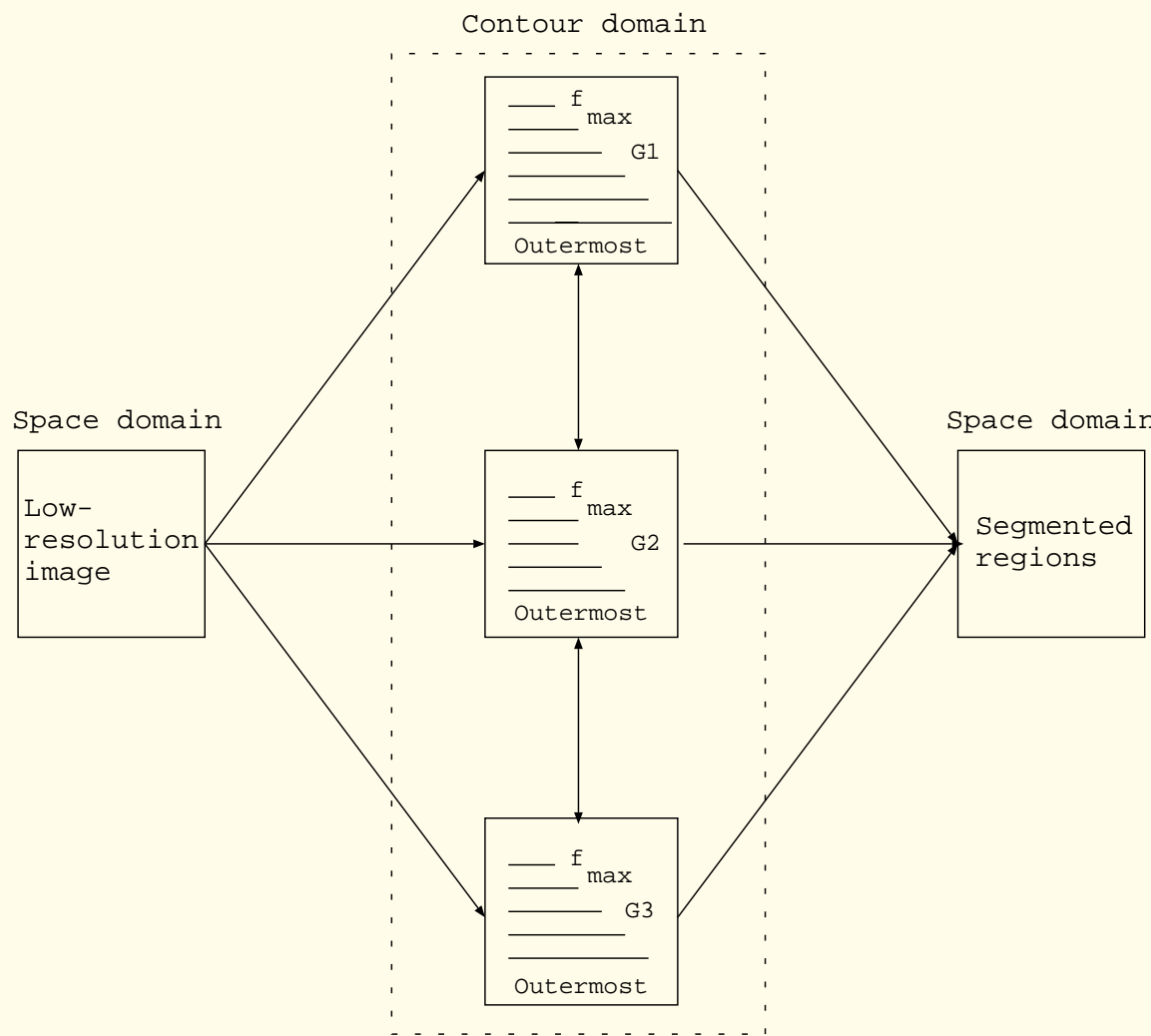


Figure 8.36: Schematic representation of hierarchical grouping of contours. G1, G2, and G3 are groups of contours that represent isolated regions in the image. Reproduced with permission from N.R. Mudigonda, R.M. Rangayyan, and J.E.L. Desautels, “Detection of breast masses in mammograms by density slicing and texture flow-field analysis”, *IEEE Transactions on Medical Imaging*, 20(12): 1215 – 1227, 2001. © IEEE.



The outermost contour in each family or group and the family count in terms of the number of contours present could be useful in the analysis of the regions segmented to reject false positives.

Masses, irrespective of their size, were observed to result in a higher family count as compared to elongated glandular tissues.

By setting a threshold on the family count, chosen to be five, dense glandular structures could be avoided from further analysis.

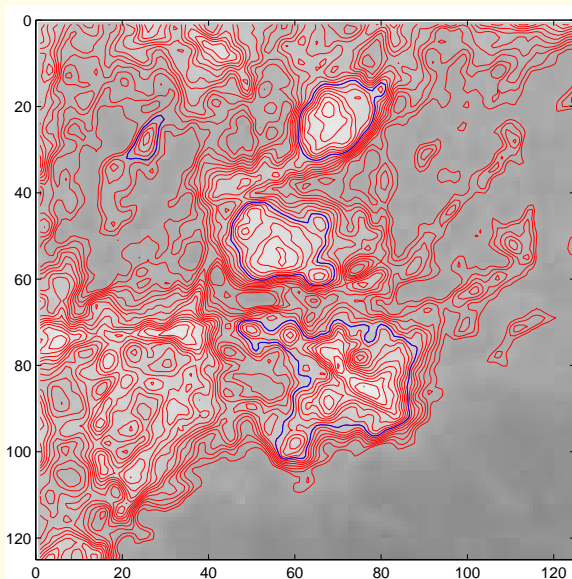
Finally, the outermost contour from each of the short-listed groups was upsampled to the full-resolution image to form the corresponding segmented area.



8.8.4 Results of segmentation of masses

The mass-detection algorithm was tested on segments of size up to $2,048 \times 2,048$ pixels of 39 mammographic images (28 benign and 11 malignant) from the MIAS database, with a spatial resolution of $50 \mu m \times 50 \mu m$.

In 29 of the 39 cases (19 benign and 10 malignant), the segmented regions were in agreement with the corresponding regions that were manually identified by the radiologist.



(a)

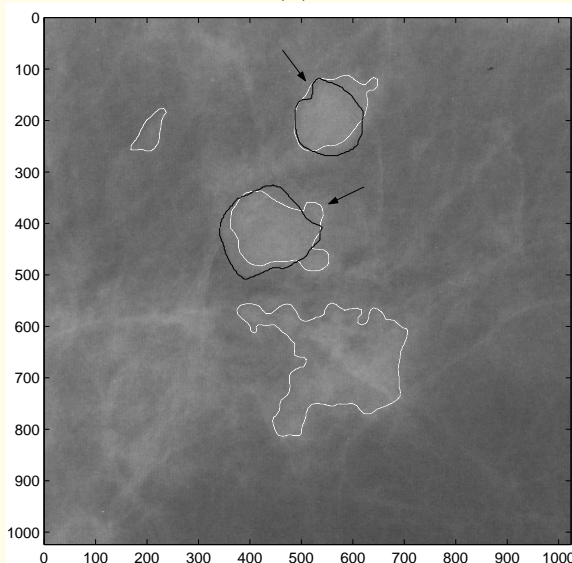


Figure 8.37 (b)



Figure 8.37: (a) Groups of isointensity contours and the outermost contour in each group in the third low-resolution image of the mammogram section of Figure 8.34 (d). (b) The contours (white) of two masses (indicated by arrows) and two false positives detected in the full-resolution image of Figure 8.34 (a), with the corresponding contours (black) of the masses drawn independently by a radiologist. Reproduced with permission from N.R. Mudigonda, R.M. Rangayyan, and J.E.L. Desautels, “Segmentation and classification of mammographic masses”, *Proceedings of SPIE Volume 3979, Medical Imaging 2000: Image Processing*, pp 55 – 67, 2000. © SPIE.

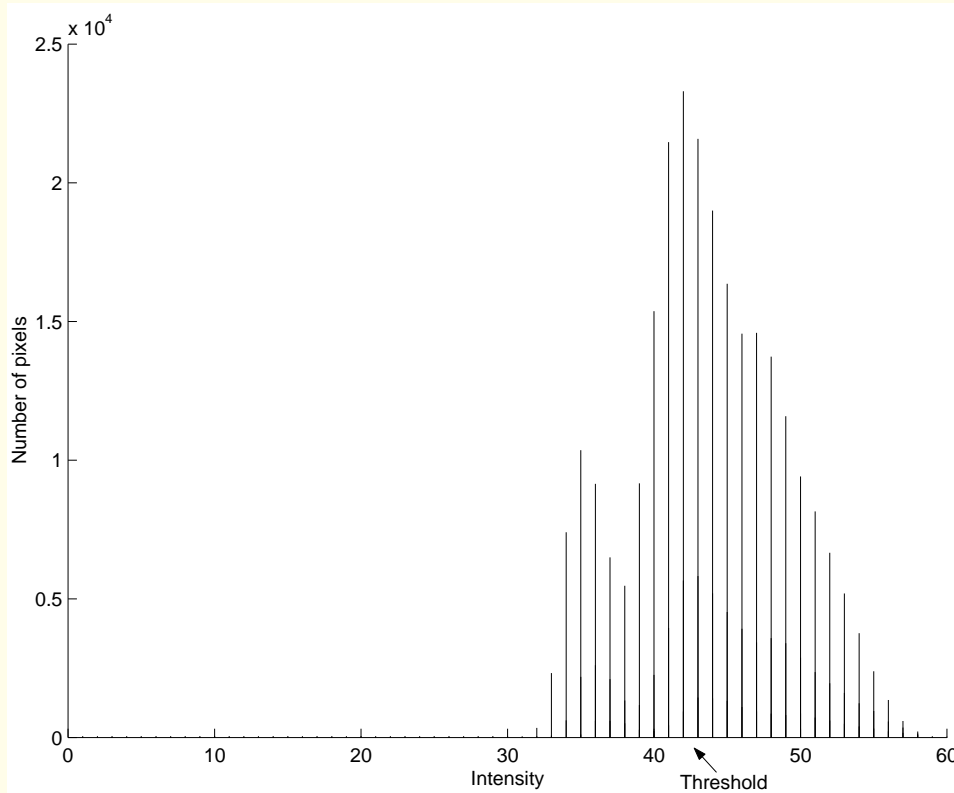
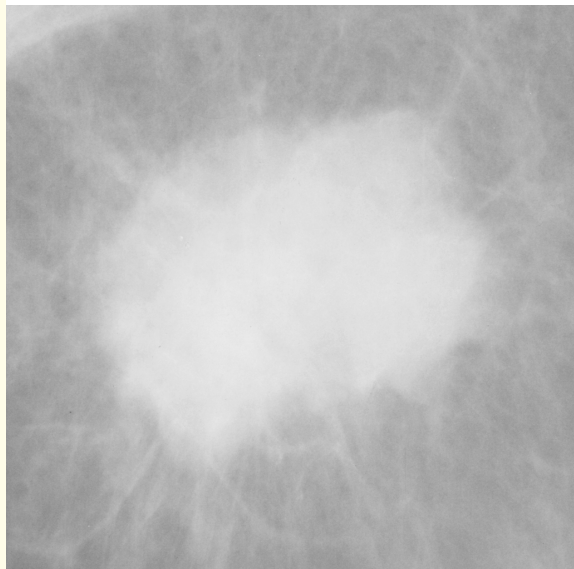


Figure 8.38: Histogram of the low-resolution and smoothed image shown in Figure 8.37 (a). Reproduced with permission from N.R. Mudigonda, R.M. Rangayyan, and J.E.L. Desautels, “Segmentation and classification of mammographic masses”, *Proceedings of SPIE Volume 3979, Medical Imaging 2000: Image Processing*, pp 55 – 67, 2000. © SPIE.



(a)

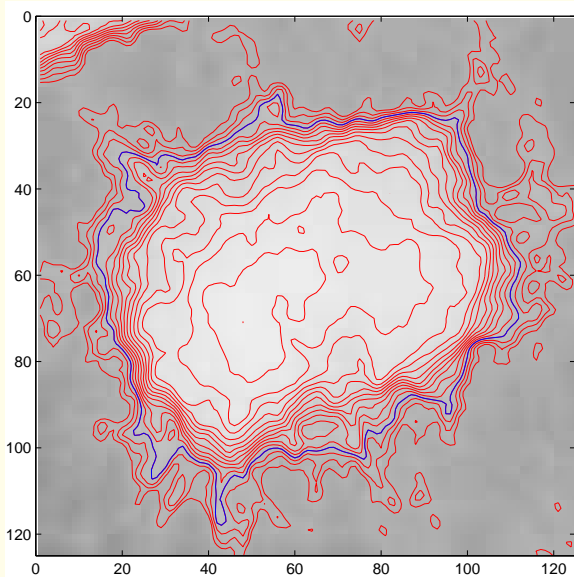
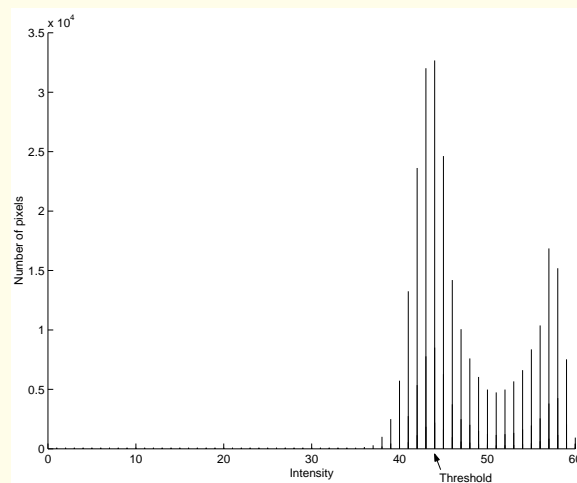


Figure 8.39 (b)



(c)

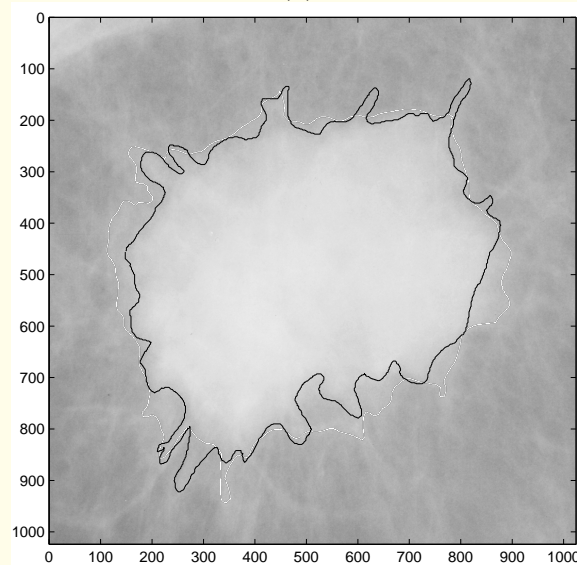


Figure 8.39 (d)



Figure 8.39: (a) A $1,024 \times 1,024$ section of a mammogram containing a spiculated malignant tumor. Pixel size = $50 \mu\text{m}$. Image width = 51 mm . (b) Group of iso-intensity contours and the outermost contour in the group in the third low-resolution image. (c) Histogram of the low-resolution and smoothed image shown. (d) The contour (white) of the spiculated malignant tumor detected in the full-resolution image, superimposed with the corresponding contour (black) drawn independently by a radiologist. Reproduced with permission from N.R. Mudigonda, R.M. Rangayyan, and J.E.L. Desautels, “Segmentation and classification of mammographic masses”, *Proceedings of SPIE Volume 3979, Medical Imaging 2000: Image Processing*, pp 55 – 67, 2000. © SPIE.



Benign-versus-malignant pattern classification was carried out using the BMDP 7M stepwise discriminant analysis program with texture features computed based upon averaged GCMs for the 29 masses (19 benign and 10 malignant) that were successfully segmented by the mass-detection procedure.

See Sections 7.3.2 and 7.9.1 for details on the computation of texture features using adaptive ribbons.

Four effective features including entropy, second moment, second difference moment, and correlation were short-listed.

The GCM-based texture features computed from the mass ribbons resulted in an average classification efficiency of 0.80.



8.8.5 *Detection of masses in full mammograms*

Masses containing important signs of breast cancer may be difficult to detect as they often occur in dense glandular tissue.

Successful identification of such difficult-to-detect masses often results in a large number of false positives.

Rejection of false positives forms an important part of algorithms for mass detection.



Algorithm of Mudigonda et al. to detect masses:

The pyramidal decomposition was extended for application to full mammogram.

The orientation information in the margins of the regions detected was analyzed using texture flow-field to reject false positives.

The methods constitute a comprehensive automated scheme for the detection of masses, analysis of false positives, and classification of mammographic masses as benign or malignant.

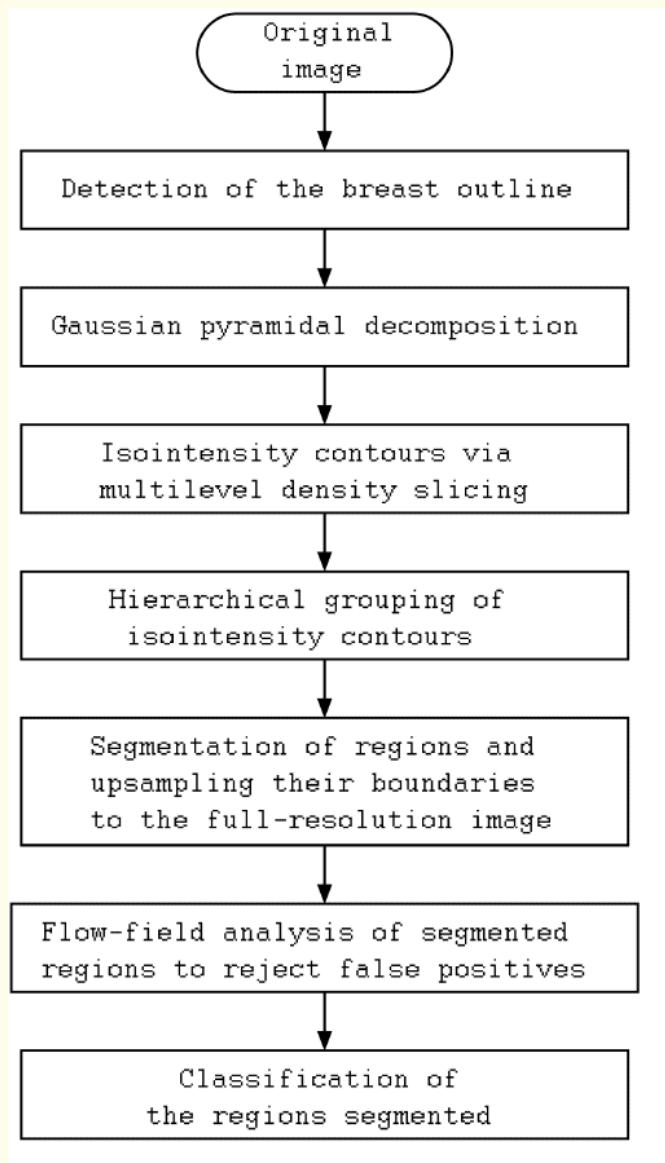


Figure 8.40: Block diagram of the algorithm for the detection of masses in full mammograms. Reproduced with permission from N.R. Mudigonda, R.M. Rangayyan, and J.E.L. Desautels, "Detection of breast masses in mammograms by density slicing and texture flow-field analysis", *IEEE Transactions on Medical Imaging*, 20(12): 1215 – 1227, 2001. © IEEE.



Detection of the breast boundary:

The image was smoothed with a separable Gaussian kernel of width 15 pixels (pixel width = $200 \mu\text{m}$, see Figure 8.41), and quantized to 64 gray levels.

A map of isointensity contours was generated by thresholding the image using a threshold close to zero.

From the map of isointensity contours, a set of closed contours was identified by employing the chain code.

The contour containing the largest area was then considered to be the outline of the breast.

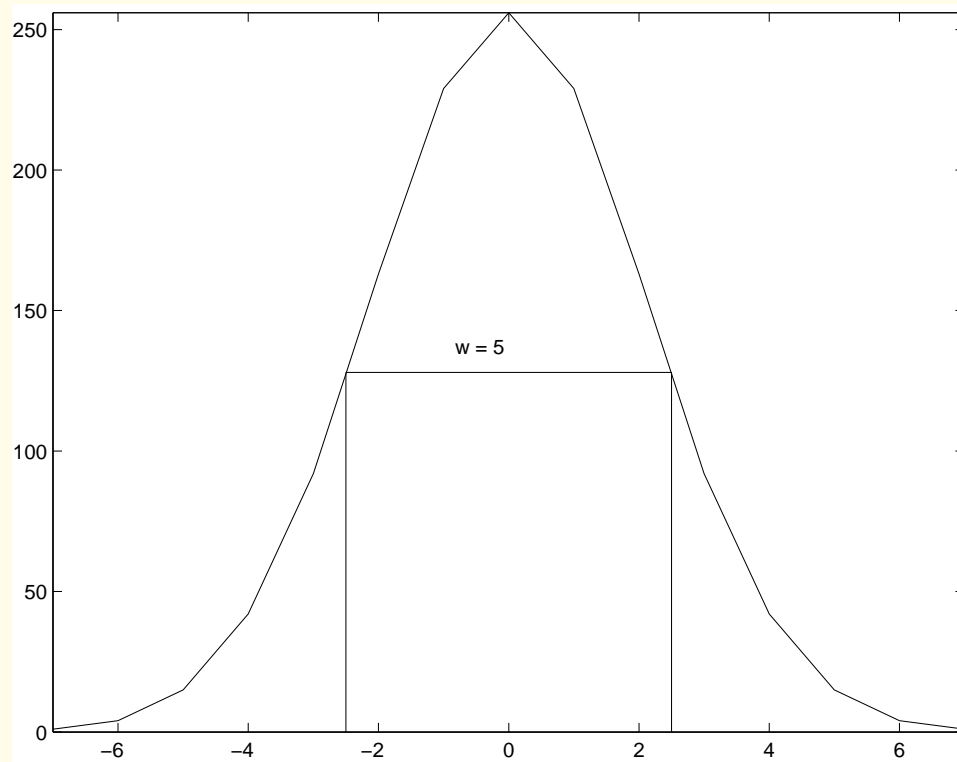


Figure 8.41: Plot of a Gaussian kernel with the support width of 15 pixels. The width at half-maximum height is five pixels. Figure courtesy of N.R. Mudigonda.

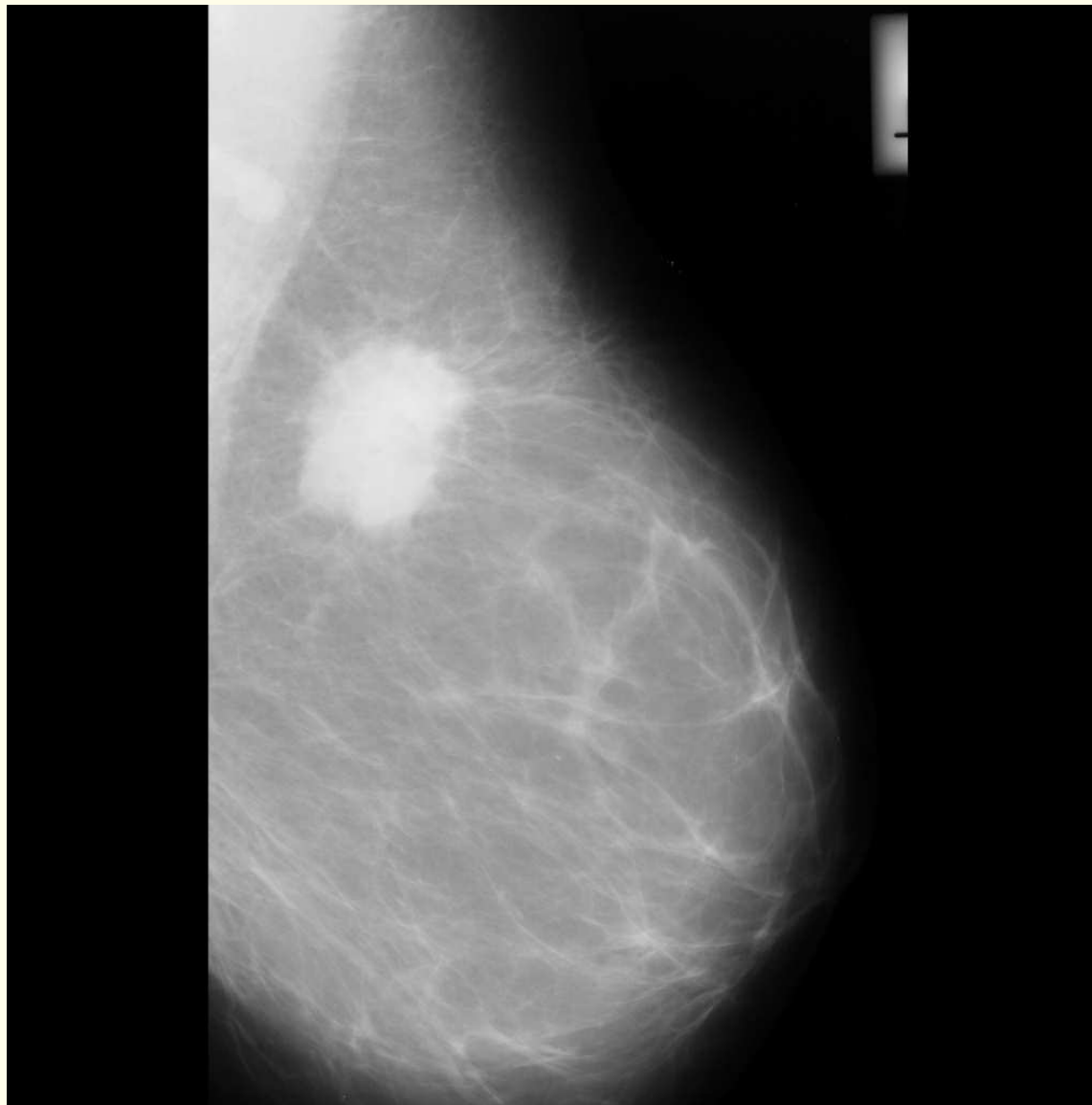


Figure 8.42: A mammogram (size $1,024 \times 1,024$ pixels, $200 \mu\text{m}$ per pixel) with a spiculated malignant tumor (radius = 2.28 cm). Case mdb184 from the MIAS database. Reproduced with permission from N.R. Mudigonda, R.M. Rangayyan, and J.E.L. Desautels, “Detection of breast masses in mammograms by density slicing and texture flow-field analysis”, *IEEE Transactions on Medical Imaging*, 20(12): 1215 – 1227, 2001. © IEEE.

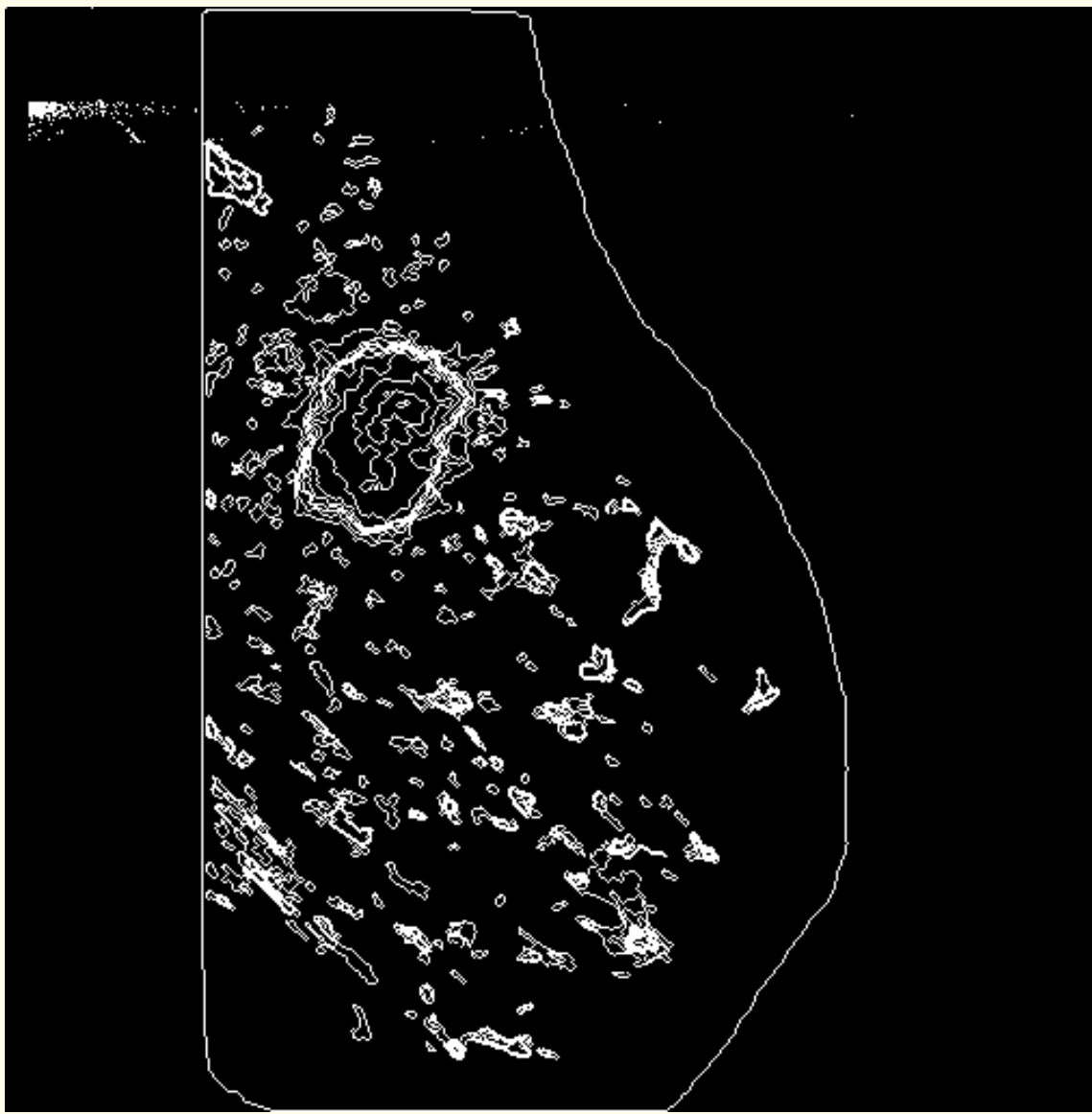


Figure 8.43: The map of isointensity contours extracted in the smoothed and subsampled version (size 512×512 pixels, $400 \mu\text{m}$ per pixel) of the mammogram shown in Figure 8.42. The breast outline detected is superimposed. In some cases, several contours overlap to produce thick contours in the printed version of the image. Reproduced with permission from N.R. Mudigonda, R.M. Rangayyan, and J.E.L. Desautels, “Detection of breast masses in mammograms by density slicing and texture flow-field analysis”, *IEEE Transactions on Medical Imaging*, 20(12): 1215 – 1227, 2001. © IEEE.



Detection of salient densities:

Gaussian pyramidal decomposition was employed to achieve the required smoothing instead of wavelet decomposition as in Section 8.8.1.

The original $8 b$ images with a spatial resolution of $200 \mu m$ were subsampled to a resolution of $400 \mu m$ after performing smoothing with a separable Gaussian kernel of width five pixels.

The width of the Gaussian kernel at half-maximum height is about $400 \mu m$.

Masses were assumed to be hyperdense, or at least of the same density, with respect to their background.



Multilevel thresholding:

In the procedure of Mudigonda et al., the low-resolution image is initially reduced to 64 gray levels in intensity and thresholded at $N = 30$ levels starting from the maximum intensity level $f_{\max} = 64$, with a step-size decrement of $\mu = 0.01 f_{\max}$.

The purpose of this step is to extract concentric groups of closed contours to represent the isolated regions in the image.

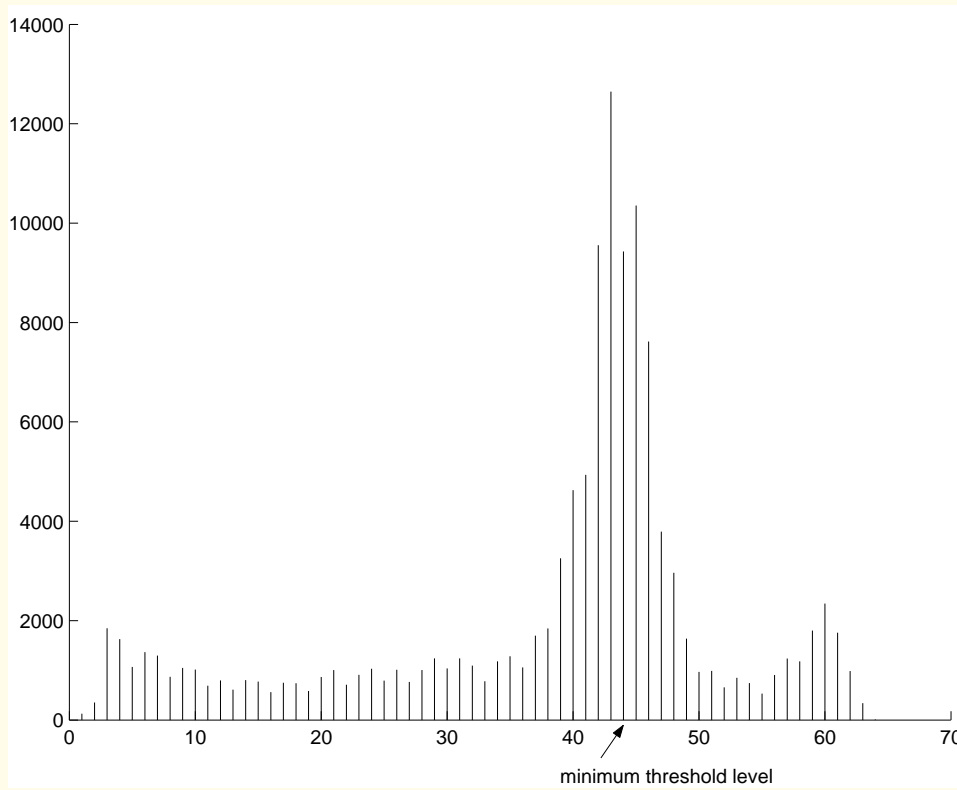


Figure 8.44: Histogram of the low-resolution image corresponding to the mammogram in Figure 8.42. Reproduced with permission from N.R. Mudigonda, R.M. Rangayyan, and J.E.L. Desautels, “Detection of breast masses in mammograms by density slicing and texture flow-field analysis”, *IEEE Transactions on Medical Imaging*, 20(12): 1215 – 1227, 2001. © IEEE.



Grouping of isointensity contours:

The scheme in Figure 8.36 was adopted to perform a two-step grouping and merging operation on the individual contours possessing a minimum circumference of 2 mm (five pixels at $400 \mu\text{m}$), to arrive at groups of concentric isointensity contours.

Initially, the contour members with intensity values ranging from $0.8 f_{\max}$ to f_{\max} , with $f_{\max} = 64$, were grouped to form a set of regions corresponding to high intensities in the image;

the remaining contour members were grouped into a separate set.

The undesired merging of adjoining regions was controlled by monitoring the running family count of each group for any abrupt fluctuations in terms of its family count.



The information from both the sets of groups of contours was combined by establishing correspondences among the outermost members of the various groups present in each set to arrive at the final set of segmented regions in the low-resolution image.

The largest contour in each group with a minimum family count of two members was upsampled into the full-resolution image to form the corresponding segmented area.



8.8.6 *Analysis of mammograms using texture flow-field*

In a mammogram of a normal breast, the fibroglandular tissues present oriented and flow-like or anisotropic textural information.

Mudigonda et al. proposed features to discriminate between masses and the strongly oriented fibroglandular tissues based upon the analysis of oriented texture in mammograms.

The method proposed by Rao and Schunck was used to characterize flow-like information in the form of intrinsic orientation angle and coherence images.



The intrinsic angle image reveals the direction of anisotropy or flow orientation of the texture at every point in the image.

Coherence is a measure of the degree or strength of anisotropy in the direction of flow.

The methodology to derive the intrinsic images begins with the computation of the gradient information at every point in the image by preprocessing the image with a gradient-of-Gaussian filter of a specified width.



The impulse response of a 2D Gaussian smoothing filter $g(x, y)$ of width σ , ignoring the scale factor, is

$$g(x, y) = \exp \frac{-(x^2 + y^2)}{2\sigma^2}, \quad (8.56)$$

The impulse response of the gradient-of-Gaussian filter $h(x, y)$ tuned to a specified orientation Θ is obtained using $g(x, y)$ as

$$h(x, y) = \left[\frac{\partial g}{\partial x}, \frac{\partial g}{\partial y} \right] \bullet [\cos \Theta, \sin \Theta], \quad (8.57)$$

where \bullet represents the dot product.



At each point in the given image, the filter $h(x, y)$, upon convolution with the image, yields the maximal response in the orientation (Θ) that is perpendicular to the orientation of the underlying texture (that is, the angle of anisotropy).

Based upon the above, and with the assumption that there exists a dominant orientation at every point in the given image, Rao and Schunck derived the optimal solution to compute the angle of anisotropy ψ_{pq} at a point (p, q) in the image as follows.



Let G_{mn} and θ_{mn} represent the gradient magnitude and gradient orientation at the point (m, n) in an image,

and $P \times P$ be the size of the neighborhood around (p, q) used for computing ψ_{pq} .

The gradient magnitude is computed as

$$G_{mn} = \sqrt{G_x^2(m, n) + G_y^2(m, n)}, \quad (8.58)$$

where $G_x(m, n)$ and $G_y(m, n)$ represent the outputs of the gradient-of-Gaussian filter at (m, n) in the x and y directions.



The gradient orientation is computed as

$$\theta_{mn} = \arctan \left[\frac{G_y(m, n)}{G_x(m, n)} \right]. \quad (8.59)$$

The projection of G_{mn} on to the gradient orientation vector at (p, q) at angle θ_{pq} is

$$G_{mn} \cos(\theta_{mn} - \theta_{pq}),$$

as illustrated schematically in Figure 8.45.

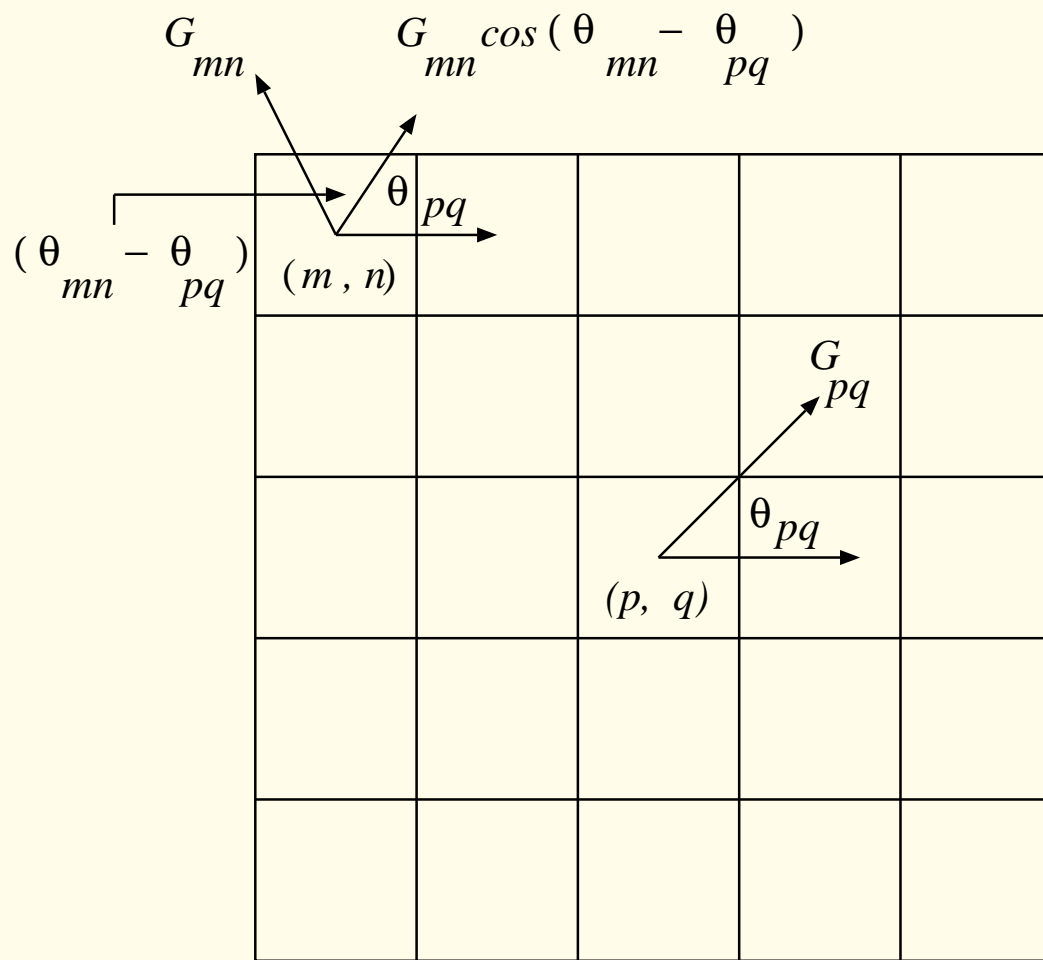


Figure 8.45: Schematic illustration of the projection of the gradient magnitude for computing the dominant orientation angle and coherence (the scheme of Rao and Schunck). G_{pq} and θ_{pq} indicate the gradient magnitude and orientation at (p, q) , respectively. The corresponding parameters at (m, n) are G_{mn} and θ_{mn} . The size of the neighborhood shown is $P \times P = 5 \times 5$ pixels. Figure courtesy of N.R. Mudigonda.



The sum-of-squares S of the projections of the gradient magnitudes computed at the various points of the neighborhood in a reference orientation specified by Θ is given by

$$S = \sum_{m=1}^P \sum_{n=1}^P G_{mn}^2 \cos^2(\theta_{mn} - \Theta) . \quad (8.60)$$

The sum S varies as the orientation Θ is varied, and attains its maximal value when Θ is perpendicular to the dominant orientation of the texture in the given set of points.



$$\frac{dS}{d\Theta} = 2 \sum_{m=1}^P \sum_{n=1}^P G_{mn}^2 \cos(\theta_{mn} - \Theta) \sin(\theta_{mn} - \Theta). \quad (8.61)$$

By setting $\frac{dS}{d\Theta} = 0$, we obtain the solution for $\Theta = \Theta_{pq}$ that maximizes S at the point (p, q) in the image as

$$\Theta_{pq} = \frac{1}{2} \arctan \left(\frac{\sum_{m=1}^P \sum_{n=1}^P G_{mn}^2 \sin 2\theta_{mn}}{\sum_{m=1}^P \sum_{n=1}^P G_{mn}^2 \cos 2\theta_{mn}} \right). \quad (8.62)$$

$$\frac{d^2S}{d\Theta^2} = -2 \sum_{m=1}^P \sum_{n=1}^P G_{mn}^2 \cos(2\theta_{mn} - 2\Theta). \quad (8.63)$$



The value of Θ_{pq} obtained using Equation 8.62 represents the direction of the maximal gradient output, because the second derivative shown in Equation 8.63 is negative at $\Theta = \Theta_{pq}$ when the texture has only one dominant orientation.

The estimated orientation angle of flow ψ_{pq} at (p, q) is

$$\psi_{pq} = \Theta_{pq} + \frac{\pi}{2}; \quad (8.64)$$

the gradient vector is perpendicular to the direction of flow.

The angles computed as above range between 0 and π radians.



The original image was smoothed using a separable Gaussian kernel, and the gradients in the x and y directions were computed using finite differences.

The width of the Gaussian affects the gradient computation;

a width of 2.2 mm (11 pixels) was used by Mudigonda et al.

The filter has a width of about 1 mm at its half-maximum height.

This filter size is appropriate given that mammograms may demonstrate lumps that are as small as 3 mm in diameter.

The gradient estimates were smoothed using a 15×15 pixels ($3 \times 3\text{ mm}$) neighborhood.



The coherence γ_{pq} was computed as the cumulative sum of the projections of the gradient magnitudes of the pixels in a window of size $P \times P$, in the direction of the dominant orientation at the point (p, q) , as

$$\gamma_{pq} = G_{pq} \frac{\sum_{m=1}^P \sum_{n=1}^P G_{mn} \cos(\theta_{mn} - \psi_{pq})}{\sum_{m=1}^P \sum_{n=1}^P G_{mn}}. \quad (8.65)$$

The result was normalized with the sum of the gradient magnitudes in the window and multiplied with the gradient magnitude to obtain high coherence values at the points in the image having high visual contrast.

Glandular tissues, ligaments, ducts, and spicules corresponding to architectural distortion are expected to possess high coherence.

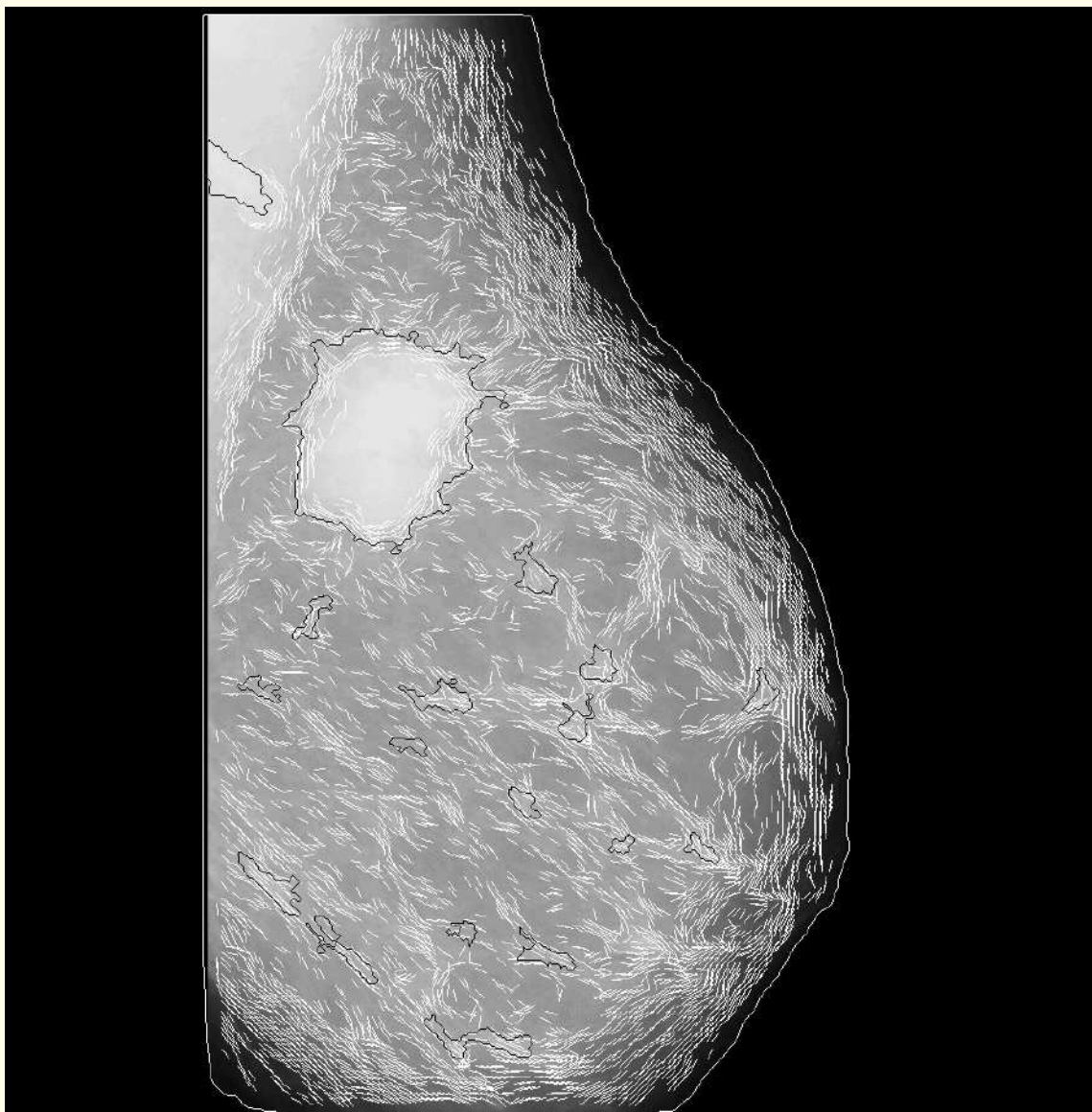


Figure 8.46: Intrinsic angle information (white lines) for the mammogram shown in Figure 8.42. The boundaries (black) represent the mass and false-positive regions segmented at the initial stage of the mass-detection algorithm. The breast outline detected is superimposed. Reproduced with permission from N.R. Mudigonda, R.M. Rangayyan, and J.E.L. Desautels, “Detection of breast masses in mammograms by density slicing and texture flow-field analysis”, *IEEE Transactions on Medical Imaging*, 20(12): 1215 – 1227, 2001. © IEEE.



Figure 8.47: Intrinsic coherence image of the mammogram shown in Figure 8.42. Reproduced with permission from N.R. Mudigonda, R.M. Rangayyan, and J.E.L. Desautels, “Detection of breast masses in mammograms by density slicing and texture flow-field analysis”, *IEEE Transactions on Medical Imaging*, 20(12): 1215 – 1227, 2001. © IEEE.



8.8.7 Adaptive computation of features in ribbons

The regions detected by the method described above vary greatly in size and shape.

A method was devised to compute adaptively the width of the ribbon for the derivation of features (see Section 7.9.1), or equivalently, the diameter of the circular morphological operator for a particular region based upon the region's size and shape.

Figure 8.48 shows a schematic representation of the method used to compute adaptively the size of the ribbon.



Initially, the diameter of the bounding circle enclosing a given candidate region was found by computing the maximal distance between any two points on its boundary.

Then, the areas of the region (A_r) and the bounding circle (A_c) enclosing the region were computed.

The width of the ribbon was computed as

$$R_w = R_c \frac{A_r}{A_c}, \quad (8.66)$$

where R_c is the radius of the bounding circle.

$\frac{A_r}{A_c}$ is a measure of narrowness and shape complexity.



The size of the ribbon computed above was limited to a maximum of 8 mm or 40 pixels.

The regions for which the sizes of ribbons computed was less than 0.8 mm or four pixels were rejected.

The ribbons of pixels (white) extracted across the boundaries (black) of the various regions detected in the image shown in Figure 8.42 are illustrated in Figure 8.49.

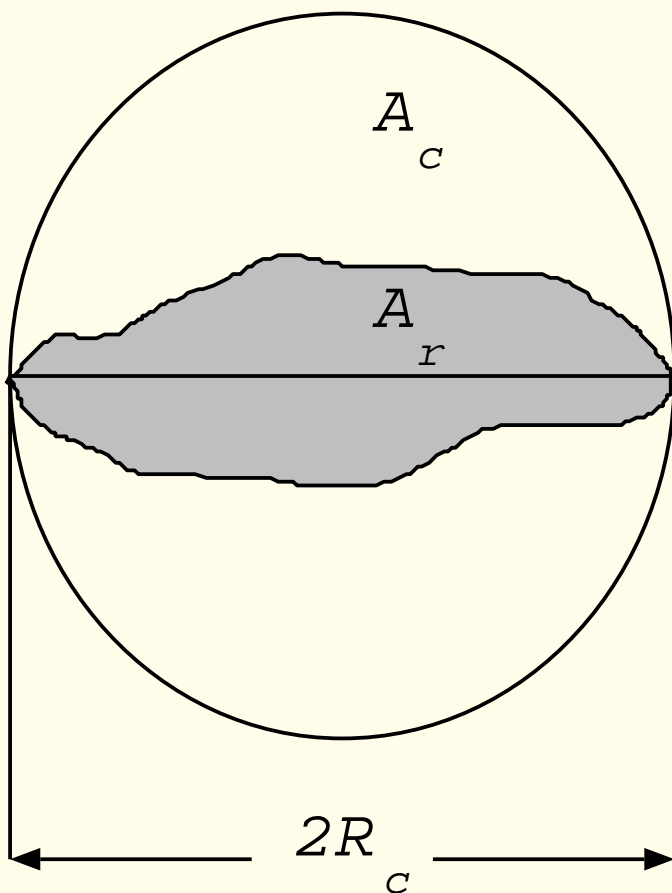


Figure 8.48: Schematic representation of the adaptive computation of the width of the ribbon. A_r : area of the candidate region, A_c : area of the bounding circle, and R_c : radius of the bounding circle. Figure courtesy of N.R. Mudigonda.

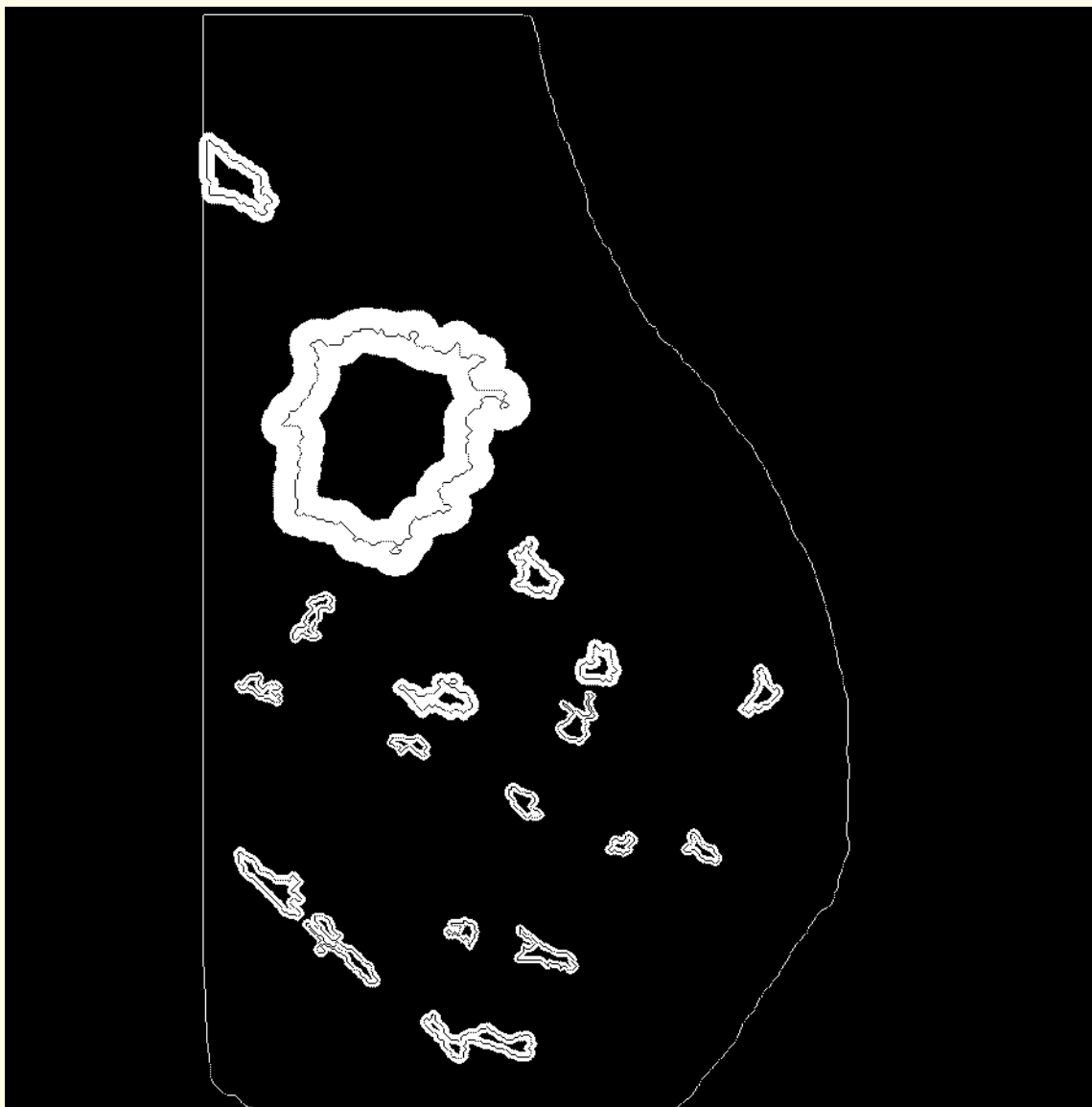


Figure 8.49: Ribbons of pixels (white) extracted adaptively across the boundaries (black) of the regions detected in the mammogram shown in Figure 8.42. Reproduced with permission from N.R. Mudigonda, R.M. Rangayyan, and J.E.L. Desautels, “Detection of breast masses in mammograms by density slicing and texture flow-field analysis”, *IEEE Transactions on Medical Imaging*, 20(12): 1215 – 1227, 2001. © IEEE.



Features for mass-versus-false-positive classification:

- Contrast (C_{fg}) : Masses in mammograms may be presumed to be hyperdense, or at least isodense, with respect to their surroundings.

The contrast (C_{fg}) of a region was computed as the difference between the mean intensities of the foreground region or ROI, and a background region defined as the region enclosed by the extracted ribbon of pixels excluding the ROI.

Regions possessing negative contrast values were rejected from further analysis.



- Coherence ratio (γ_r): The interior regions of masses are expected to be less coherent than their edges.
The ratio (γ_r) of the mean coherence of the ROI (excluding the ribbon of pixels) to the mean coherence in the ribbon of pixels was computed.



- Entropy of orientation estimates (H_o): The orientation of spicules in the margins of spiculated masses is usually random. The orientation estimates computed in the margins of circumscribed masses could cover a wide range of angles between zero and π radians, and may not possess any dominant orientation.

Fibroglandular tissues are highly directional.

For these reasons, the entropy (H_o) of the orientation estimates was computed in the ribbon of pixels of each region detected.



- Variance of coherence-weighted angle estimates (σ_h^2):

A coherence-weighted angular histogram was computed for each region by incrementing the numbers of occurrence of angles with the corresponding magnitudes of coherence values, after resampling the angle values in the ribbon to $Q = 6$ equally spaced levels between zero and π .

The histogram was normalized with the sum of the coherence values in the corresponding ribbon.

$$\sigma_h^2 = \frac{1}{Q} \sum_{i=1}^Q (\alpha i - \mu_h)^2, \quad (8.67)$$

where αi , $i = 1, 2, \dots, Q$, are the normalized values of the histogram, and

$$\mu_h = \frac{1}{Q} \sum_{i=1}^Q \alpha i. \quad (8.68)$$



Features for benign-versus-malignant classification:

Five GCM-based texture features: entropy, second moment, difference moment, inverse difference moment, and correlation (see Section 7.3.2), were computed in the ribbon of pixels extracted adaptively from each segmented mass margin.

GCMs constructed by scanning each mass ribbon in the 0° , 45° , 90° , and 135° directions were averaged to obtain a single GCM.



8.8.8 Results of mass detection in full mammograms

Mudigonda et al. tested their methods with 56 images ($1,024 \times 1,024$ pixels at a resolution of $200 \mu\text{m}$), including 30 benign masses, 13 malignant tumors, and 13 normal cases.

The dataset included circumscribed and spiculated cases in both of the benign and malignant categories.

The mean values of the sizes of the masses were $1.07 \pm 0.77 \text{ cm}$ and $1.22 \pm 0.85 \text{ cm}$ for the benign and malignant categories.

The overall detection accuracy was 74% at 11 false-positive regions per image in the initial stage of detection.



Mass-versus-false-positive classification:

The four features C_{fg} , γ_r , H_o , and σ_h^2 , described in Section 8.8.7, were computed in the ribbons of the candidate regions that were detected in all of the 56 cases tested.

A linear discriminant classifier was used to identify the true mass regions and false positives.

First, a mass-versus-normal-tissue classification was conducted with the 671 regions detected in the 56 cases tested.

Next, malignant-tumor-versus-normal-tissue classification was performed using the features computed from the 343 regions detected in the 13 malignant and the 13 normal cases tested.



Pattern classification was carried out using the BMDP 7M stepwise discriminant analysis program with the leave-one-out scheme.

The efficiency in the classification of malignant tumors versus normal tissue was 0.9.

The efficiency in discriminating between masses (both benign and malignant) and normal tissue was 0.87.

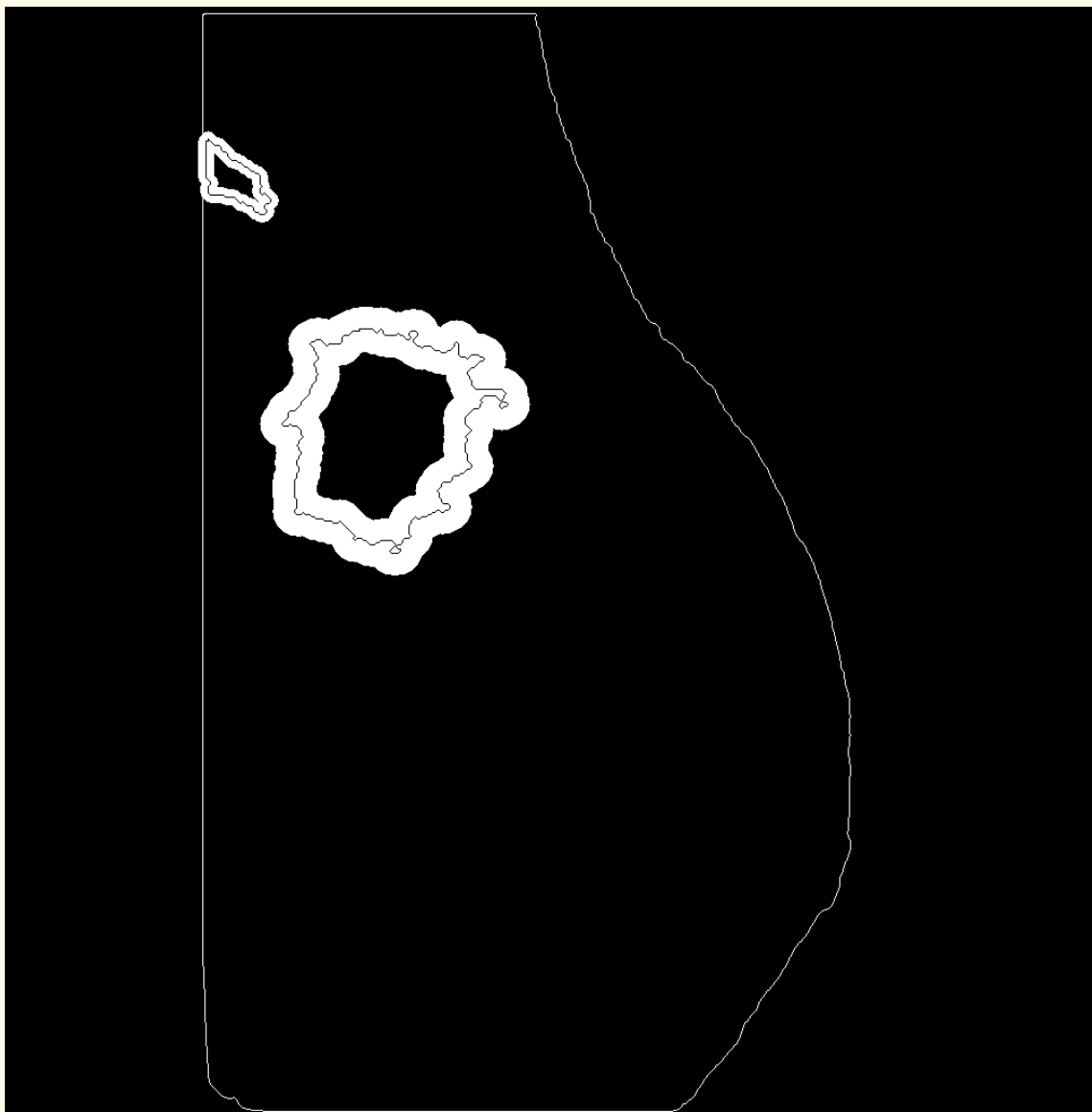


Figure 8.50: Adaptive ribbons of pixels (white) and boundaries (black) of the regions retained in the mammogram shown in Figure 8.42 after the false-positive analysis stage. The larger region corresponds to the malignant tumor; the other region is a false positive. See also Figure 8.49. Reproduced with permission from N.R. Mudigonda, R.M. Rangayyan, and J.E.L. Desautels, “Detection of breast masses in mammograms by density slicing and texture flow-field analysis”, *IEEE Transactions on Medical Imaging*, 20(12): 1215 – 1227, 2001. © IEEE.



The mass-versus-normal-tissue classification experiment, involving the 32 mass regions (19 benign and 13 malignant) that the algorithm successfully detected and 639 false positives from a total of 56 images (including 13 normal cases), resulted in an overall classification efficiency of 0.87, with a sensitivity of 81% at 2.2 false positives per image.

A total of six masses (four benign and two malignant) were misclassified as normal tissue.

If the fact that the algorithm missed 11 benign masses during the initial stage of detection itself is taken into consideration, the true detection sensitivity of the algorithm with the database of 30 benign and 13 malignant masses reduces to 60% (26/43).



In malignant-tumor-versus-normal-tissue classification, a high overall efficiency of 0.9 was achieved;

the dataset included 13 malignant tumors and 330 false positives from a total of 26 images (including 13 normal cases).

A sensitivity of 85% was obtained at 2.46 false positives per image.

Although all of the 13 tumors were successfully detected in the initial stage, two of the malignant tumors that were detected were misclassified later as normal tissue, yielding a small proportion (2/13) of false negatives.

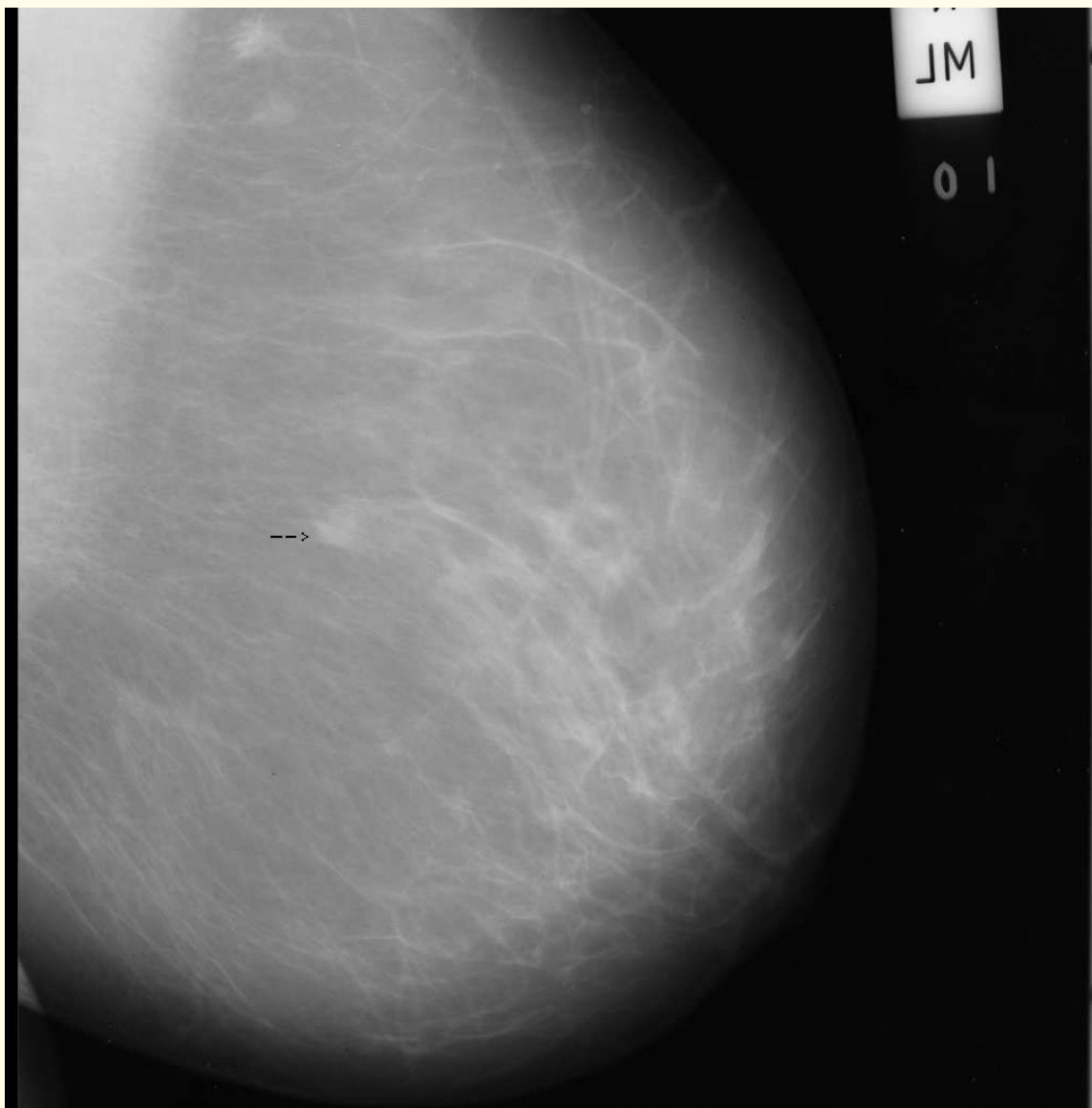


Figure 8.51: A mammogram (size $1,024 \times 1,024$ pixels, $200 \mu\text{m}$ per pixel) with a spiculated malignant tumor (pointed by the arrow, radius = 0.54 cm). Case mdb144 from the MIAS database. Reproduced with permission from N.R. Mudigonda, R.M. Rangayyan, and J.E.L. Desautels, “Detection of breast masses in mammograms by density slicing and texture flow-field analysis”, *IEEE Transactions on Medical Imaging*, 20(12): 1215 – 1227, 2001. © IEEE.

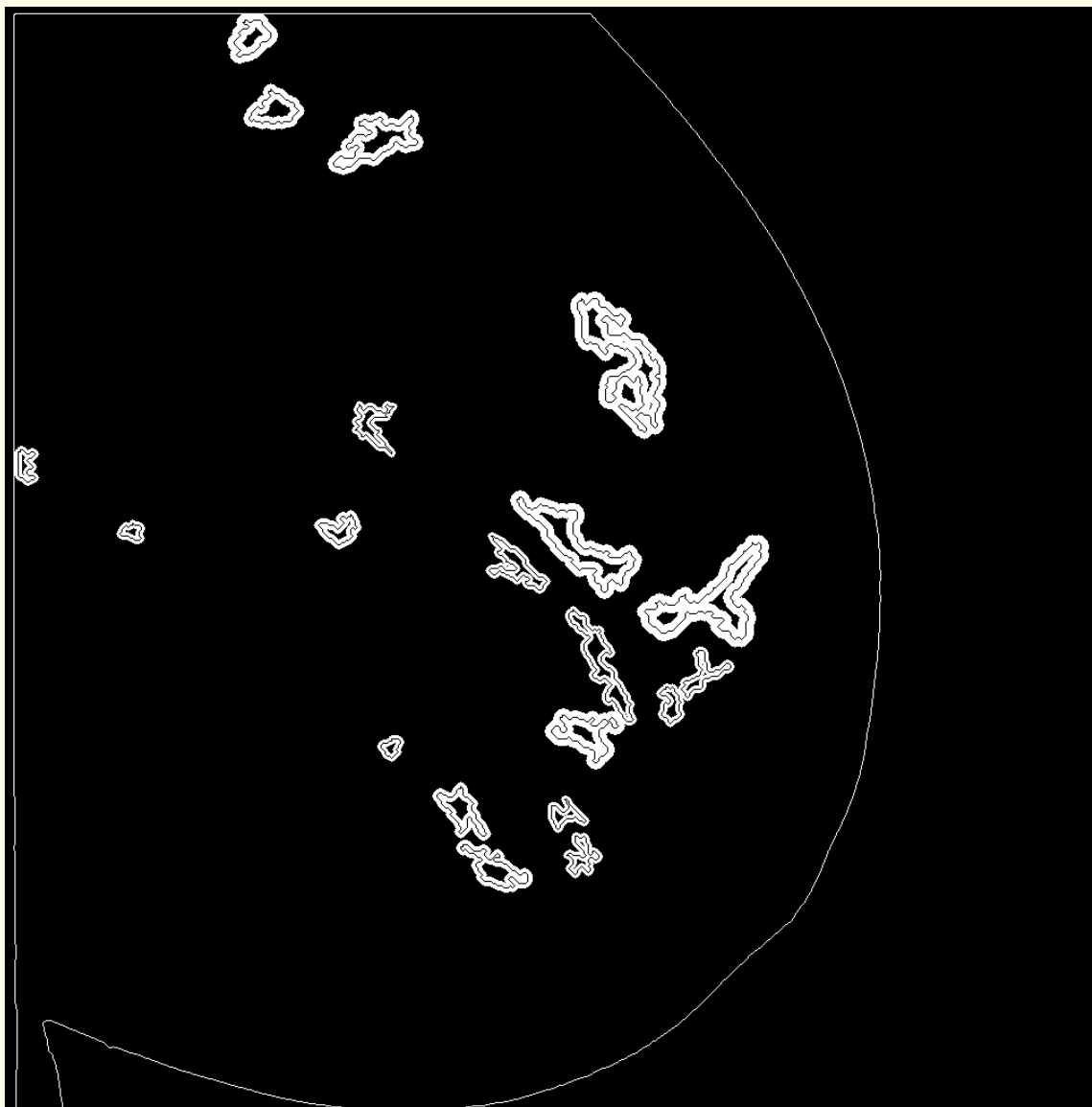


Figure 8.52: Ribbons of pixels (white) extracted adaptively across the boundaries (black) of the regions detected in the mammogram shown in Figure 8.51. Reproduced with permission from N.R. Mudigonda, R.M. Rangayyan, and J.E.L. Desautels, “Detection of breast masses in mammograms by density slicing and texture flow-field analysis”, *IEEE Transactions on Medical Imaging*, 20(12): 1215 – 1227, 2001. © IEEE.

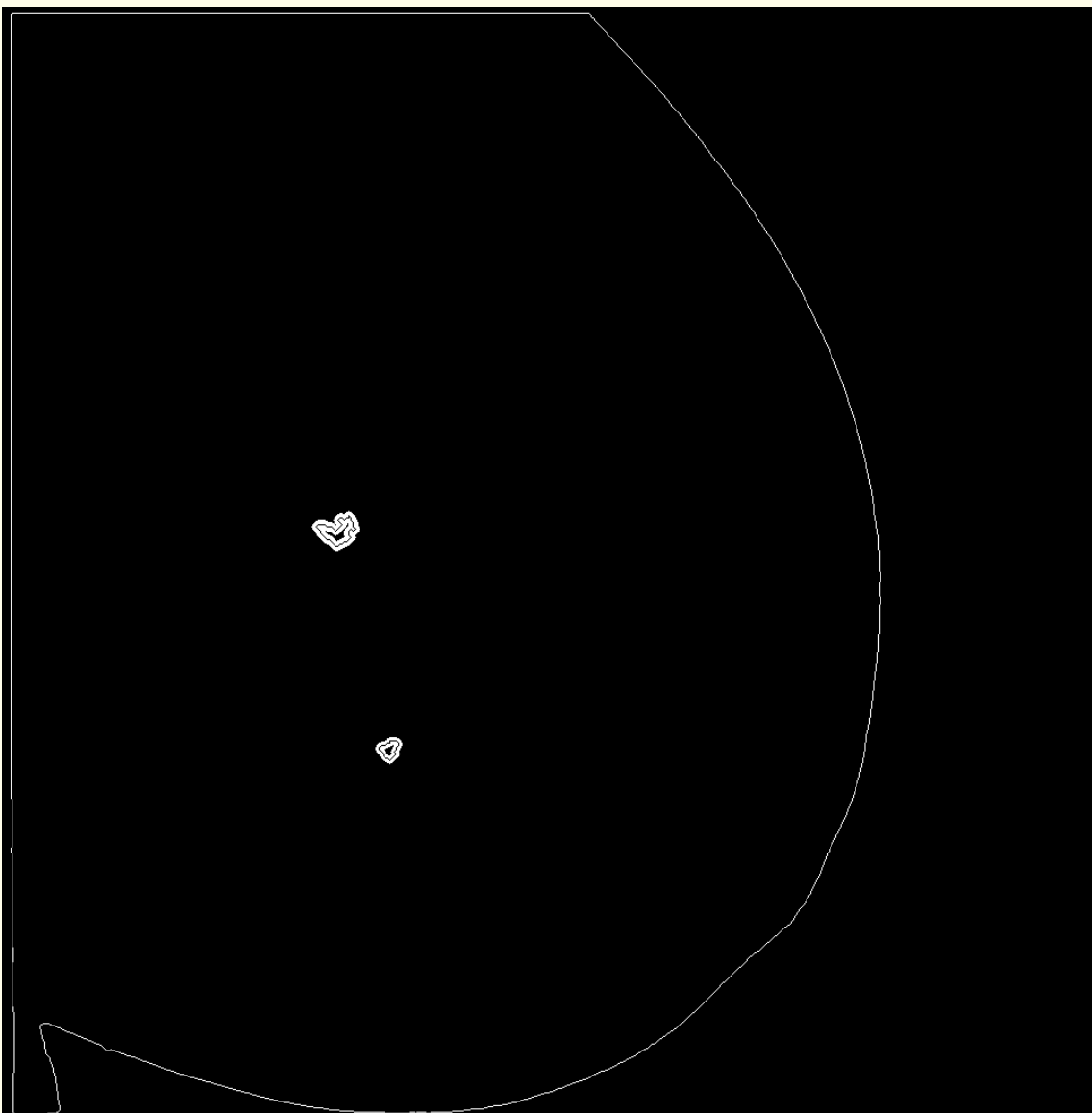


Figure 8.53: Adaptive ribbons of pixels (white) and boundaries (black) of the regions retained in the mammogram shown in Figure 8.51 after the false-positive analysis stage. The larger region corresponds to the malignant tumor; the other region is a false positive. See also Figure 8.52. Reproduced with permission from N.R. Mudigonda, R.M. Rangayyan, and J.E.L. Desautels, “Detection of breast masses in mammograms by density slicing and texture flow-field analysis”, *IEEE Transactions on Medical Imaging*, 20(12): 1215 – 1227, 2001. © IEEE.



Benign-versus-malignant classification:

The five GCM-based texture features described earlier were computed for the 32 cases (19 benign and 13 malignant) that were successfully segmented by the mass-detection procedure.

Pattern classification was carried out using the BMDP stepwise logistic regression program.

The overall classification efficiency was 0.79.

The results indicate that the mass regions segmented in images of resolution $200 \mu\text{m}$ possess adequate discriminant information for classification as benign or malignant with texture features.



8.9 Application: Bilateral Asymmetry in Mammograms

Asymmetry between the left and right mammograms is an important sign used by radiologists to diagnose breast cancer.

Ferrari et al. proposed a procedure based upon directional analysis using Gabor wavelets to analyze global disturbance between the left and right mammograms of an individual in the normally symmetrical flow of mammary structures.

The analysis was focused on the fibroglandular disc of the mammograms, segmented in a preprocessing step.



8.9.1 *The fibroglandular disc*

The fibroglandular disc is an anatomical region of the breast characterized by dense tissues, ligaments, vessels, and ducts.

Segmentation of the fibroglandular disc is an important stage in the detection of asymmetry between the left and right mammograms or for monitoring breast density changes.

Breast cancer occurs most frequently in the upper and outer quadrant of the breast.

Breast cancer is associated more commonly with glandular than fatty tissues.



Ferrari et al. proposed a method to segment the fibroglandular disc in mammograms.

Prior to the detection of the fibroglandular disc, the breast boundary and the pectoral muscle are detected using the methods described in Sections 5.9 and 5.10.

The fibroglandular disc is detected using a breast density model.

The parameters of the model are estimated by using the EM algorithm and the minimum-description length (MDL) principle.

A reference value computed by using information from the pectoral muscle region is used along with the breast density model to identify the fibroglandular disc.



8.9.2 Gaussian mixture model of breast density

The breast density model used by Ferrari et al. is based upon a Gaussian mixture model estimated by using the gray-level intensity distribution that represents categories or classes with different density values in mammograms.

It was assumed that the number of tissue classes in the effective region of the breast (after extracting the pectoral muscle) may vary from two to four.



1. Uncompressed fatty tissues — represented by fatty tissues localized in the periphery of the breast.
2. Fatty tissues — composed by fatty tissues that are localized next to the uncompressed fatty tissues, and surround the denser areas of the fibroglandular disc.
3. Nonuniform density tissues — including the density region that surrounds the high-density portions of the fibroglandular disc extending close to the chest wall.
4. High-density tissues — represented by the high-density portions of the fibroglandular disc.



The marginal probability of a gray level x is the sum of the probability over all of the mixture components, represented by a linear superposition of multiple weighted Gaussians as

$$p(x|\Theta) = \sum_{i=1}^K W_i p(x|\theta_i), \quad (8.69)$$

where x represents the gray-level values in the image;

W_i are the normalized mixing parameters,

$$\sum_{i=1}^K W_i = 1 \text{ with } 0 \leq W_i \leq 1;$$



$p(x|\overline{\theta}_i)$ is the Gaussian PDF parameterized by $\overline{\theta}_i = [\mu_i, \sigma_i]$,

that is, the mean value μ_i and the standard deviation σ_i of the i^{th} Gaussian kernel;

the vector $\overline{\Theta}$ represents the collection of the parameters of the mixture model $(W_1, W_2, \dots, W_K, \overline{\theta}_1, \overline{\theta}_2, \dots, \overline{\theta}_K)$;

K is the number of Gaussian kernels (tissue categories).



The Gaussian kernel is represented as

$$p(x|\bar{\theta}_i) = \frac{1}{\sqrt{2\pi\sigma_i^2}} \exp\left[-\frac{(x - \mu_i)^2}{2\sigma_i^2}\right]. \quad (8.70)$$

In the case of using features other than the gray-level values of the image, such as texture features, a multivariate Gaussian must be used instead of a univariate Gaussian.

Then, the mean value and the standard deviation of the gray-level values are replaced by the mean vector and the covariance matrix of the feature vectors.



In the model, the Bayesian assumption is made:

that the PDF associated with a pixel in the image is independent of that of the other pixels given a class of tissue,

and furthermore, independent of its position in the image.

Estimation of the parameters is performed using the EM algorithm, which is an iterative procedure that maximizes the log-likelihood of the parameters of the model for a dataset representing a PDF.

Estimation is performed in two consecutive steps:

the E-step and the M-step.



In the E-step, the current set of parameters is used to compute the model, which is assumed to be correct and the most likely distribution of the data with respect to the model is found.

In the M-step, the parameters of the model are reevaluated with respect to the new data distribution by maximizing the log-likelihood, given as

$$\log L(\bar{\Theta}|\chi) = \log \prod_{i=1}^N p(x_i|\bar{\Theta}), \quad (8.71)$$

where N is the number of pixels in the effective region of the breast (the region demarcated by the breast boundary without the pectoral muscle), and χ represents the data sample.

The procedure is iterated until the values of $\log L(\bar{\Theta}|\chi)$ between two consecutive estimation steps increase by less than 1%, or the number of iterations reaches a specified limit (200 cycles).



Initialization of the model parameters:

The parameters of the model were initialized by setting the center and weight of each Gaussian as

$$\mu_i = \eta \text{ and } W_i = 1/K,$$

where $i = 1, 2, \dots, K$ is the index of the Gaussian kernel,

and η is a random value within the range defined by the minimum and maximum gray-level values present in the effective area of the breast.



The variance σ_i^2 of each Gaussian was initialized to the nearest distance to the other Gaussian kernels.

If the variance σ_i^2 became less than unity during the maximization step (the M-step), it was reinitialized with a large random value.

This procedure was intended to avoid shrinkage of the variance to a small value.

The EM estimation procedure was initialized and repeated three times to minimize the chance of convergence to a local minimum.



Model selection:

The MDL principle was used to select the number K of the Gaussian kernels of the model so as to maximize the quantity

$$\log L(\bar{\Theta}|\chi) - \frac{N(K)}{2} \log K, \quad (8.72)$$

where $N(K) = K(2d + 1)$ is the number of free parameters in the mixture model with K Gaussian kernels.

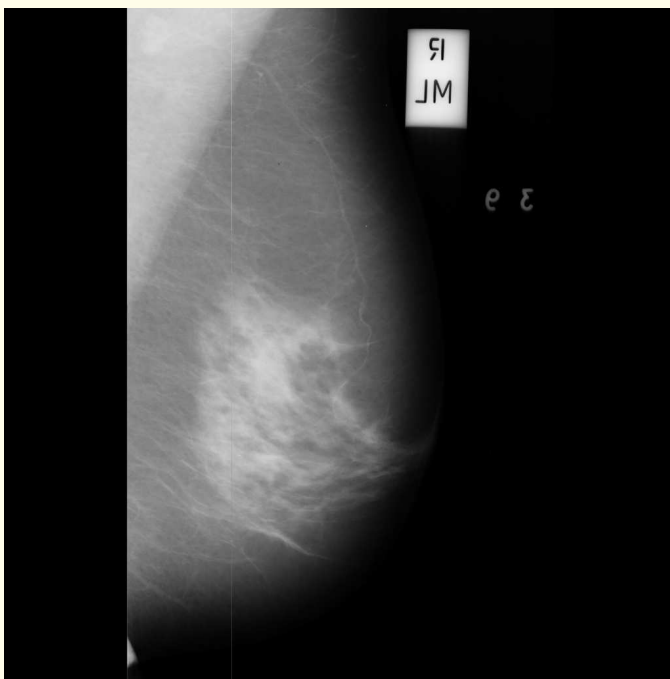
The value of K ranges from two to four, and $d = 1$ represents the dimension of the feature space.



8.9.3 *Delimitation of the fibroglandular disc*

After computing the parameters of the Gaussian mixture model, the maximum-likelihood method was applied to the original image to produce a K -level image.

The image encoded at each pixel cluster membership with the highest likelihood among the K estimated Gaussian kernels.



(a)

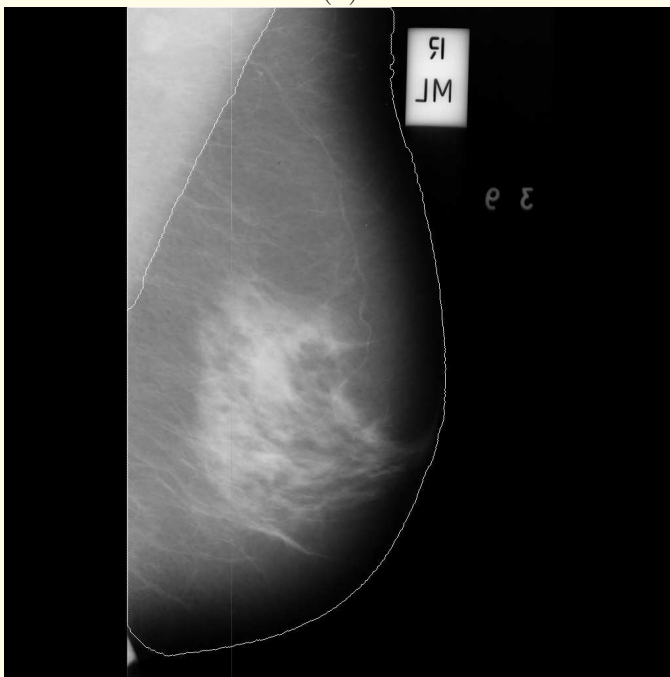
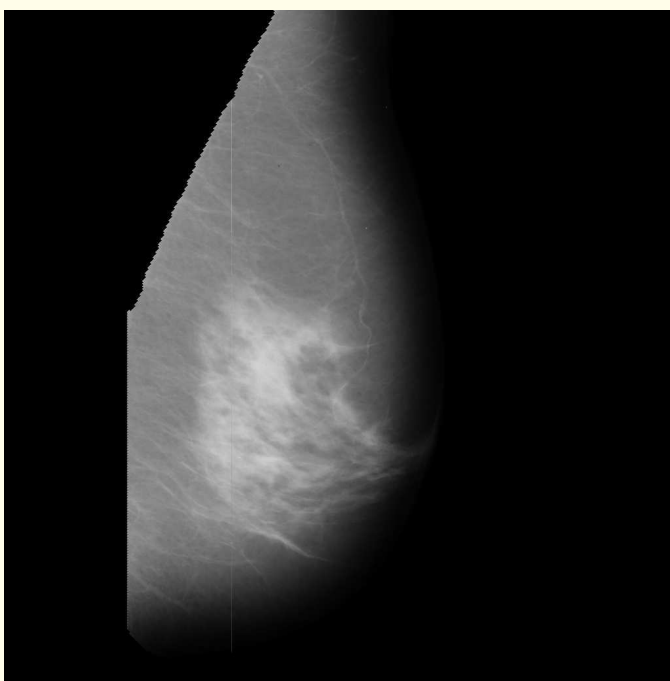


Figure 8.54 (b)



(c)

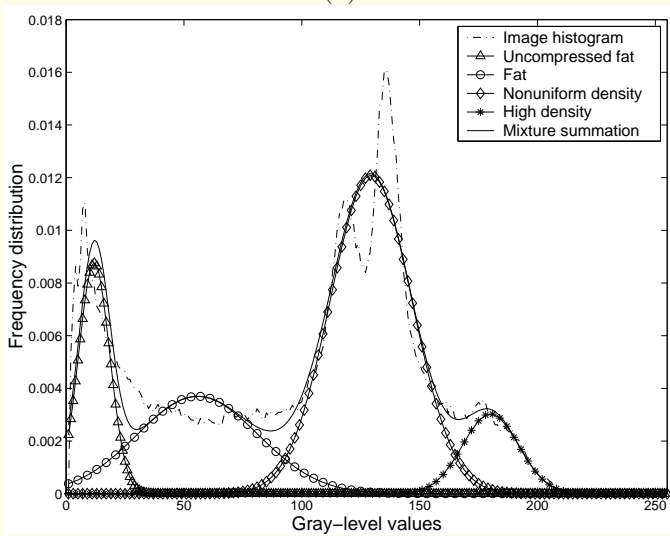
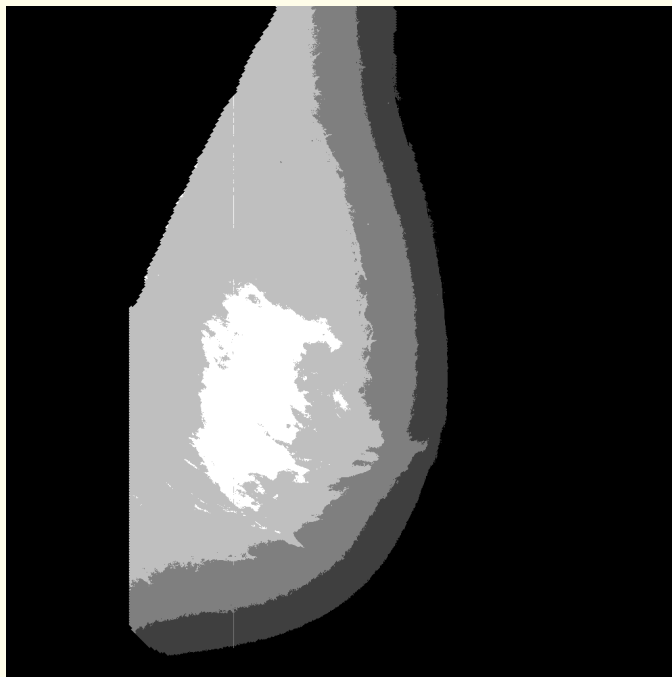


Figure 8.54 (d)



(e)

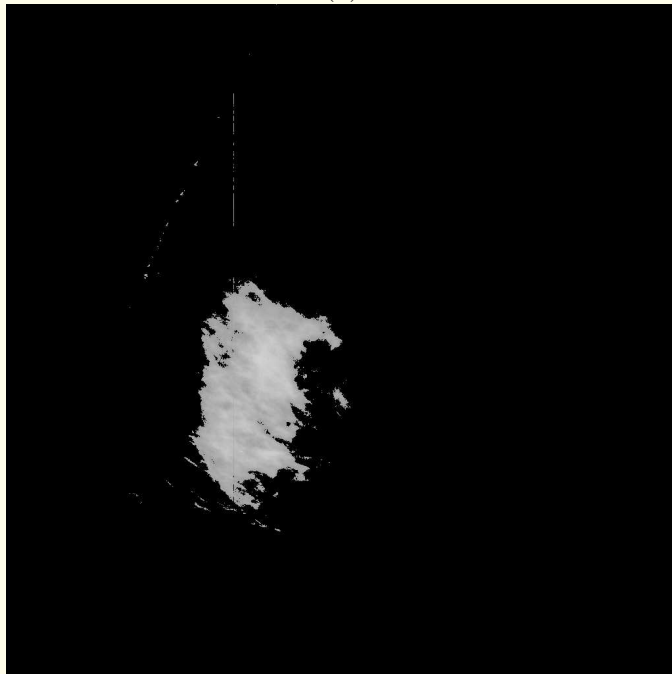


Figure 8.54 (f)



Figure 8.54: (a) Original mammographic image mdb042 from the Mini-MIAS database. (b) Breast contour and pectoral muscle edge detected automatically. (c) Effective region of the mammogram obtained after performing the segmentation steps. (d) Histogram of the effective area of the mammogram and the mixture of Gaussian components. (e) Four-level image resulting from the EM algorithm. (f) Fibroglandular disc obtained after thresholding. Reproduced with permission from R.J. Ferrari, R.M. Rangayyan, R.A. Borges, and A.F. Frère, “Segmentation of the fibro-glandular disc in mammograms using Gaussian mixture modelling”, *Medical and Biological Engineering and Computing*, 42: 378 – 387, 2004. © IFMBE.



The density of the pectoral muscle can be used as a reference in the interpretation of densities in the breast tissue:

regions of similar brightness or density will most likely correspond to fibroglandular tissue.

The K -level cluster was classified as the fibroglandular region

if $\mu_K \geq \mu_P - \sigma_P$,

where μ_P and σ_P are the mean and standard deviation of the gray-level values of the pectoral muscle region,

and μ_K is the mean gray level of the cluster K computed from the effective region of the given image.



A simplified description of the methods is as follows:

1. Initialize the Gaussian mixture model parameters

$$\overline{\Theta}(\mu_i, \sigma_i^2, W_i, i = 1, 2, \dots, K).$$

2. Repeat:

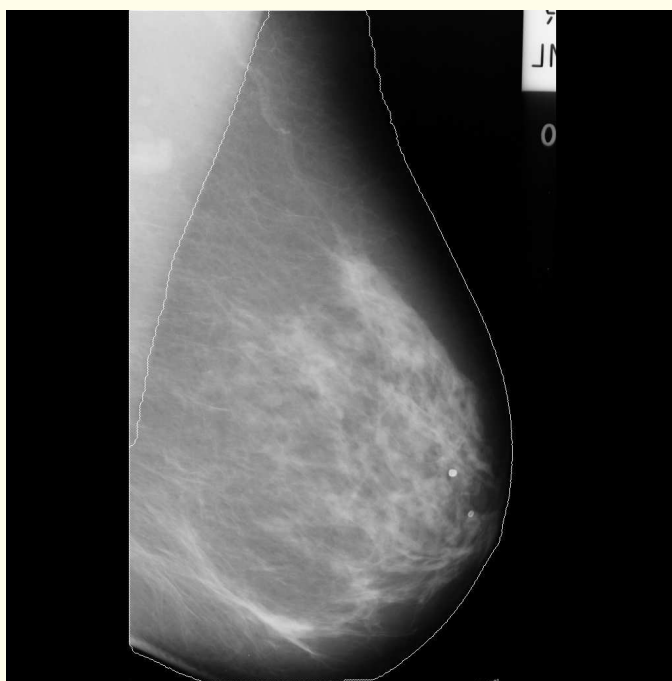
(a) E-step: Compute the model $p(x|\overline{\Theta})$ by maximizing the log-likelihood and assuming the parameter vector Θ to be correct.

(b) M-step: Reevaluate Θ based upon the new data distribution computed in the previous step.

Until $\log L(\overline{\Theta}|\chi) - \frac{N(K)}{2} \log K$ increases by less than 1%.

3. Obtain the K -level image by encoding in each pixel the cluster membership with the highest likelihood.

4. Delimit the fibroglandular disc based upon the density of the pectoral muscle.



(a)

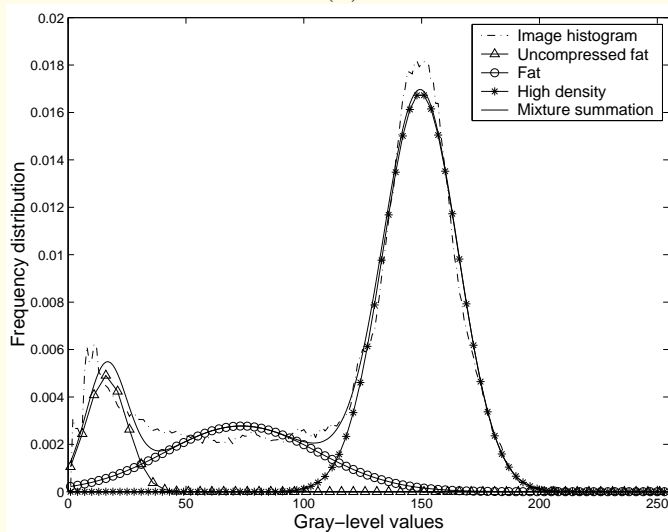
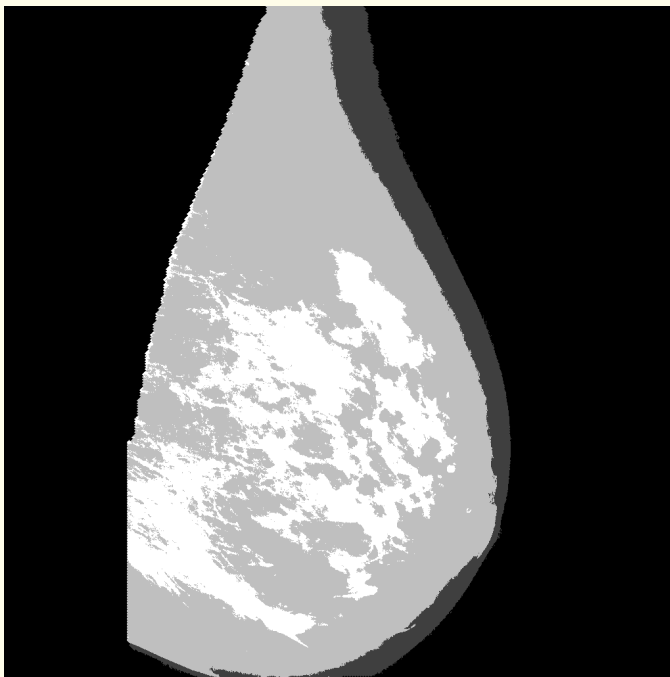


Figure 8.55 (b)



(c)

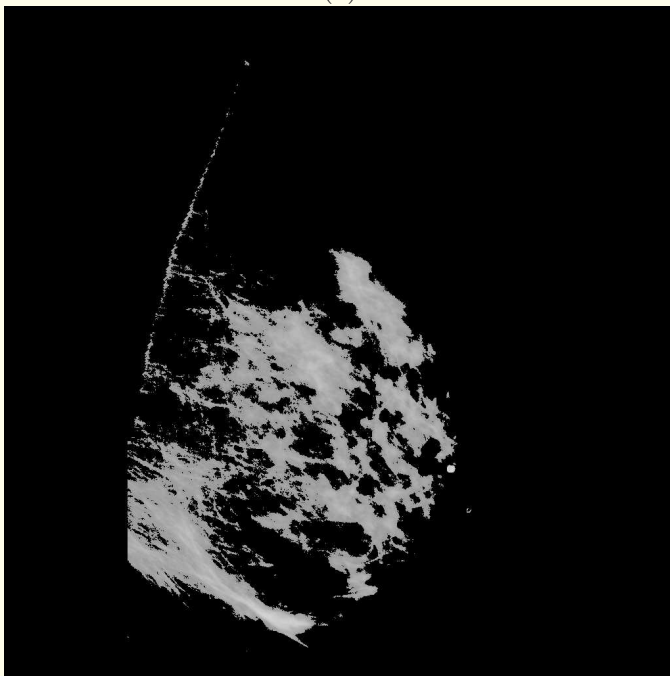


Figure 8.55 (d)



Figure 8.55: (a) Breast contour and pectoral muscle edge superimposed on the original image mdb008. (b) Histogram of the effective area of the mammogram and the mixture of Gaussian components. (c) Three-level image resulting from the EM algorithm. (d) Fibroglandular disc obtained after thresholding. Reproduced with permission from R.J. Ferrari, R.M. Rangayyan, R.A. Borges, and A.F. Frère, “Segmentation of the fibro-glandular disc in mammograms using Gaussian mixture modelling”, *Medical and Biological Engineering and Computing*, 42: 378 – 387, 2004. © IFMBE.



Evaluation of the results of segmentation:

Ferrari et al. used 84 images from the Mini-MIAS database to test the methods for segmentation of the fibroglandular disc.

The results for approximately 81% of the cases (68 images) were rated as acceptable.



8.9.4 *Motivation for directional analysis of mammograms*

Ferrari et al. proposed a scheme based upon a bank of Gabor functions and the KLT to analyze directional components of images.

The method was applied to detect global signs of asymmetry in the fibroglandular discs of the left and right mammograms of a given subject.



8.9.5 *Directional analysis of fibroglandular tissue*

Ferrari et al. used the formulation of 2D Gabor functions as a Gaussian modulated by a complex sinusoid, specified by the frequency of the sinusoid W and the standard deviations σ_x and σ_y of the Gaussian envelope as

$$\psi(x, y) = \frac{1}{2\pi\sigma_x\sigma_y} \exp \left[-\frac{1}{2} \left(\frac{x^2}{\sigma_x^2} + \frac{y^2}{\sigma_y^2} \right) + j 2\pi Wx \right]. \quad (8.73)$$



Gabor wavelets were obtained by dilation and rotation of $\psi(x, y)$:

$$\psi_{m,n}(x, y) = a^{-m} \psi(x', y'), \quad a > 1, \quad m, n = \text{integers},$$

$$\begin{aligned} x' &= a^{-m} [(x - x_0) \cos \theta + (y - y_0) \sin \theta], \\ y' &= a^{-m} [-(x - x_0) \sin \theta + (y - y_0) \cos \theta], \end{aligned} \tag{8.74}$$

(x_0, y_0) is the center of the filter in the spatial domain,
 $\theta = \frac{n\pi}{K}$, K is the total number of orientations desired,
 m and n indicate the scale and orientation.

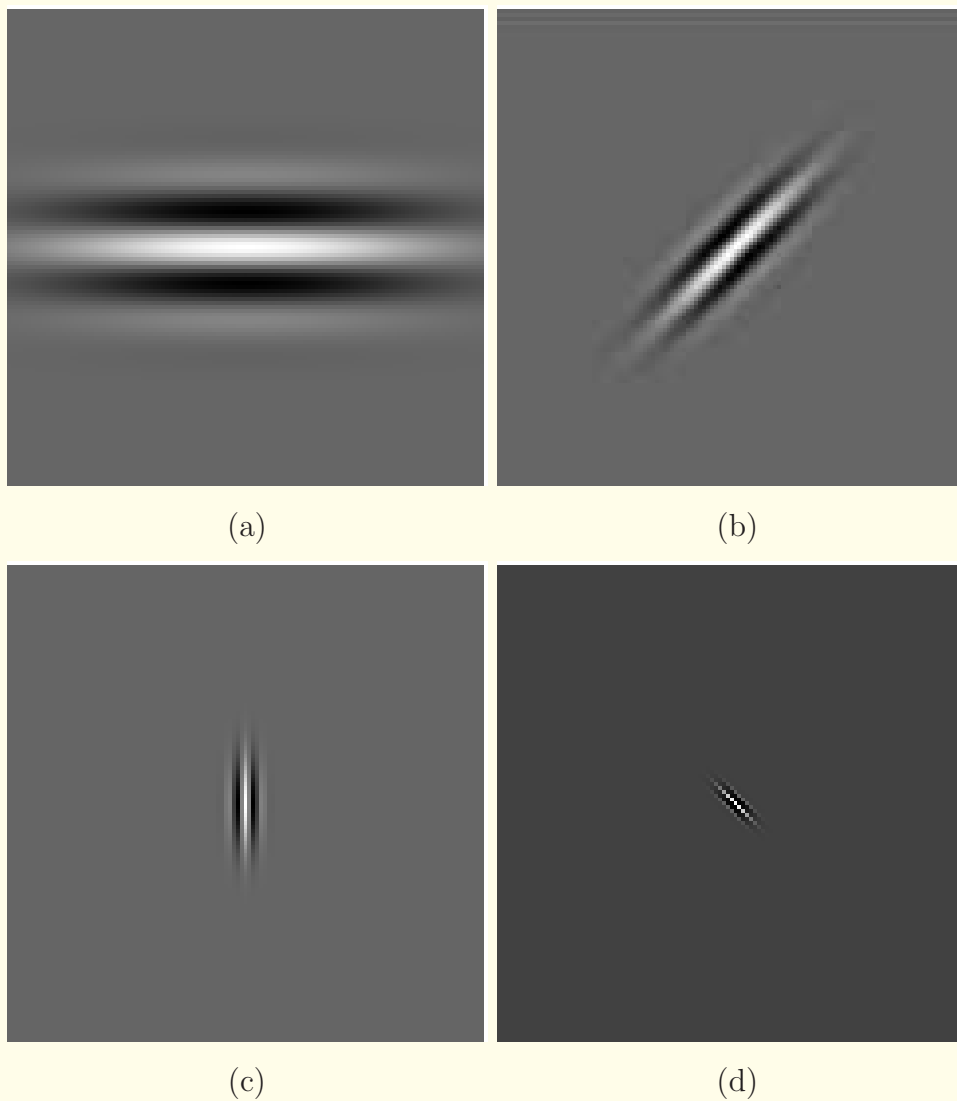


Figure 8.56: Examples of Gabor wavelets in the space domain, with four orientations ($\theta = 0^\circ, 45^\circ, 90^\circ$, and 135°) and four scales ($\sigma_x = 11, 5, 2, 1$, and $\sigma_y = 32, 16, 7, 4$ pixels). The size of each wavelet image shown is 121×121 pixels. Reproduced with permission from R.J. Ferrari, R.M. Rangayyan, J.E.L. Desautels, and A.F. Frère, “Analysis of asymmetry in mammograms via directional filtering with Gabor wavelets”, *IEEE Transactions on Medical Imaging*, 20(9): 953 – 964, 2001. © IEEE.



The Gabor function in Equation 8.73 can be written in the frequency domain as

$$\Psi(u, v) = \frac{1}{2\pi\sigma_u\sigma_v} \exp \left\{ -\frac{1}{2} \left[\frac{(u - W)^2}{\sigma_u^2} + \frac{v^2}{\sigma_v^2} \right] \right\}, \quad (8.75)$$

where $\sigma_u = \frac{1}{2\pi\sigma_x}$ and $\sigma_v = \frac{1}{2\pi\sigma_y}$.

A design strategy used is to project the filters so as to ensure that the half-peak magnitude supports of the filter responses in the frequency spectrum touch one another, as shown in Figure 8.57.

In this manner, it can ensured that the filters will capture most of the information with minimal redundancy.

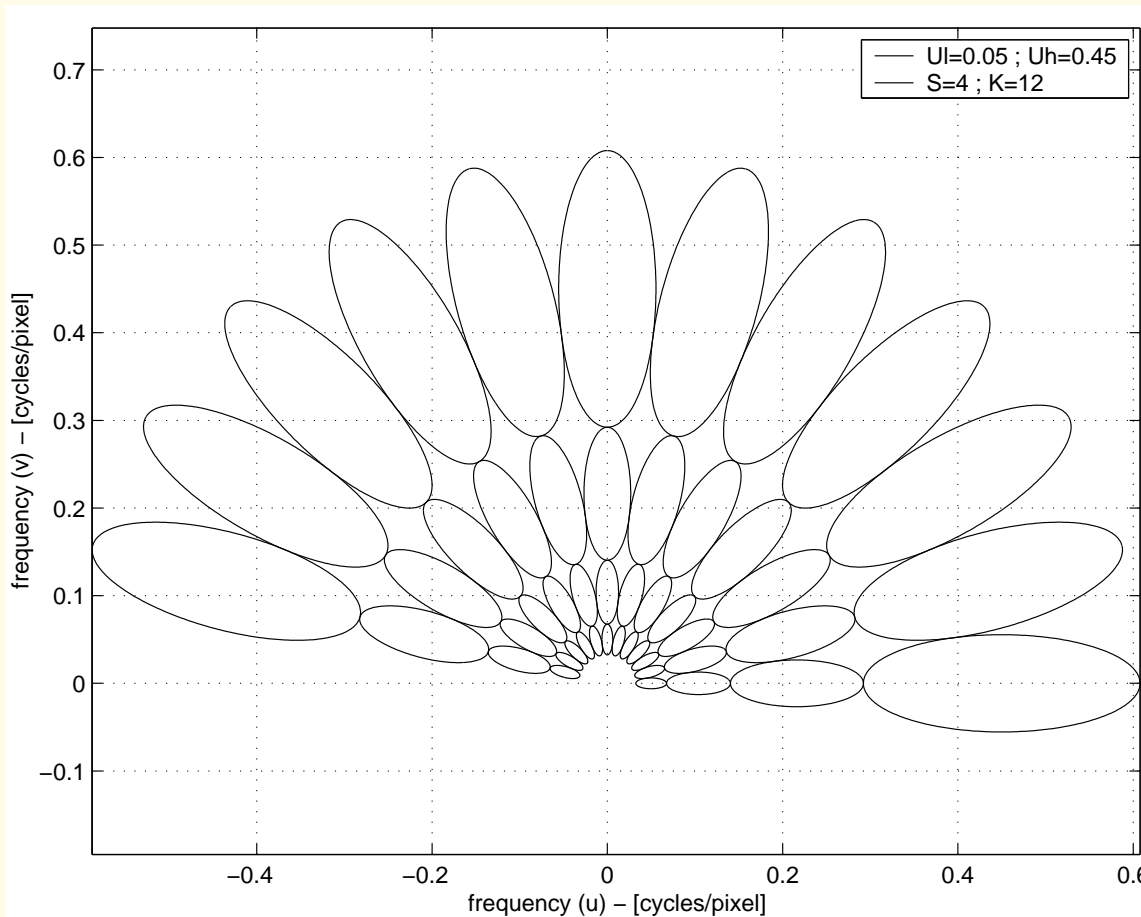
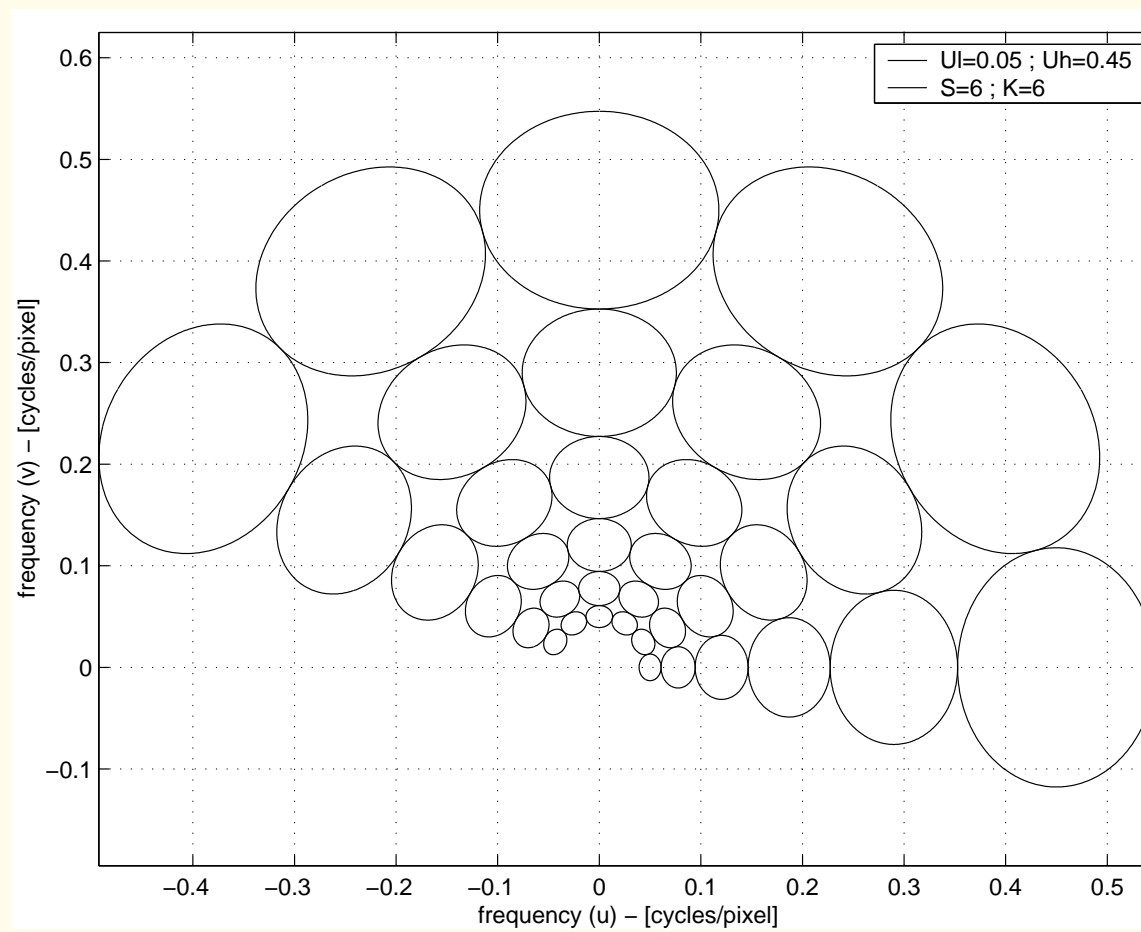


Figure 8.57 (a)



(b)

Figure 8.57: Examples of Gabor filters in the frequency domain. Each ellipse represents the range of the corresponding filter response from 0.5 to 1.0 in squared magnitude. The plots (a) and (b) illustrate two ways of dividing the frequency spectrum by changing the U_l , U_h , S , and K parameters of the Gabor representation. Plot (a) represents the filter bank used in the work of Ferrari et al. for the analysis of mammograms. The redundancy in the representation is minimized by ensuring that the half-peak magnitude supports of the filter responses touch one another. Reproduced with permission from R.J. Ferrari, R.M. Rangayyan, J.E.L. Desautels, and A.F. Frère, “Analysis of asymmetry in mammograms via directional filtering with Gabor wavelets”, *IEEE Transactions on Medical Imaging*, 20(9): 953 – 964, 2001. © IEEE.



In the formulation of Ferrari et al., the Gabor wavelet representation uses only real-valued, even-symmetric filters oriented over a range of 180° .

To ensure that the bank of Gabor filters designed as above is a family of admissible 2D Gabor wavelets, the filters $\psi(x, y)$ must satisfy the admissibility condition of finite energy;

their Fourier transforms are pure bandpass functions having zero response at DC.

This condition was achieved by setting the DC gain of each filter as $\Psi(0, 0) = 0$, which ensures that the filters do not respond to regions with constant intensity.



The approach described above results in the following formulas for computing the filter parameters σ_u and σ_v :

$$a = \left(\frac{U_h}{U_l} \right)^{\frac{1}{S-1}}, \quad (8.76)$$

$$\sigma_u = \frac{(a - 1)U_h}{(a + 1)\sqrt{2 \ln 2}}, \quad (8.77)$$

$$\sigma_v = \frac{\tan\left(\frac{\pi}{2K}\right) \left[U_h - \left(\frac{\sigma_u^2}{U_h}\right) 2 \ln 2 \right]}{\sqrt{2 \ln 2 - \frac{(2 \ln 2)^2 \sigma_u^2}{U_h^2}}}. \quad (8.78)$$



U_l and U_h denote the lower and upper center frequencies of interest.

K and S are the number of orientations and the number of scales in the desired multiresolution decomposition procedure.

The frequency of the sinusoid W is set equal to U_h ,

and $m = 0, 1, \dots, S - 1$.



The expansion coefficients

$$\begin{aligned} c_{m,n} &= \langle f(x, y), \psi_{m,n}(x, y) \rangle \\ &= \int_x \int_y f(x, y) \psi_{m,n}(x, y) dx dy, \end{aligned} \quad (8.79)$$

are the projections of the image $f(x, y)$ onto the Gabor functions, where \langle , \rangle denotes the inner product.

In this case, the analysis and synthesis windows are the same, and the original image can be reconstructed as

$$f(x, y) = \sum_m \sum_n \langle f(x, y), \psi_{m,n}(x, y) \rangle \psi_{m,n}(x, y). \quad (8.80)$$



In the dual-frame approach, the projection coefficients

$$c_{m,n} = \langle f(x, y), \tilde{\psi}_{m,n}(x, y) \rangle$$

are obtained by minimizing the cost function

$$\kappa = \left| f(x, y) - \sum_m \sum_n c_{m,n} \psi_{m,n}(x, y) \right|^2, \quad (8.81)$$

where $\tilde{\psi}_{m,n}$ is the dual frame.



In directional filtering and analysis, the interest lies in image analysis without the requirement of exact reconstruction (synthesis) of the image.

Therefore, instead of using the wavelet coefficients, Ferrari et al. used the magnitude of the filter response, computed as

$$a_{m,n} = |f(x, y) * \psi^{even}_{m,n}(x, y)|, \quad (8.82)$$

where $\psi^{even}_{m,n}(x, y)$ indicates the even-symmetric part of the complex Gabor filter, and $*$ represents 2D convolution.



By adjusting the parameters U_l and U_h in the Gabor representation of Manjunath and Ma, the range of the frequency spectrum to be used for multiresolution analysis may be selected.

The area of each ellipse in Figure 8.57 represents the spectrum of frequencies covered by the corresponding Gabor filter.

Once the range of the frequency spectrum is adjusted, the choice of the number of scales and orientation may be made to cover the range of the spectrum as required.

The choice of the number of scales (S) and orientations (K) used in the work of Ferrari et al. was based upon the resolution required for detecting oriented information with high selectivity.



By selecting $U_l = 0.05$, $U_h = 0.45$, $S = 4$, and $K = 12$, Ferrari et al. set the Gabor representation to have a frequency bandwidth of approximately one octave and an angular bandwidth of 15° .

The effects of changing the U_l , U_h , S , and K parameters of the Gabor representation as above on frequency localization are shown in Figure 8.57.

The KLT was used to select the principal components of the filter outputs, preserving only the most relevant directional elements present at all of the scales considered.

The results were combined as in Figure 8.58, to form an S -dimensional vector (\bar{x}) for each pixel from each set of the corresponding pixels in the filtered images ($S = 4$).

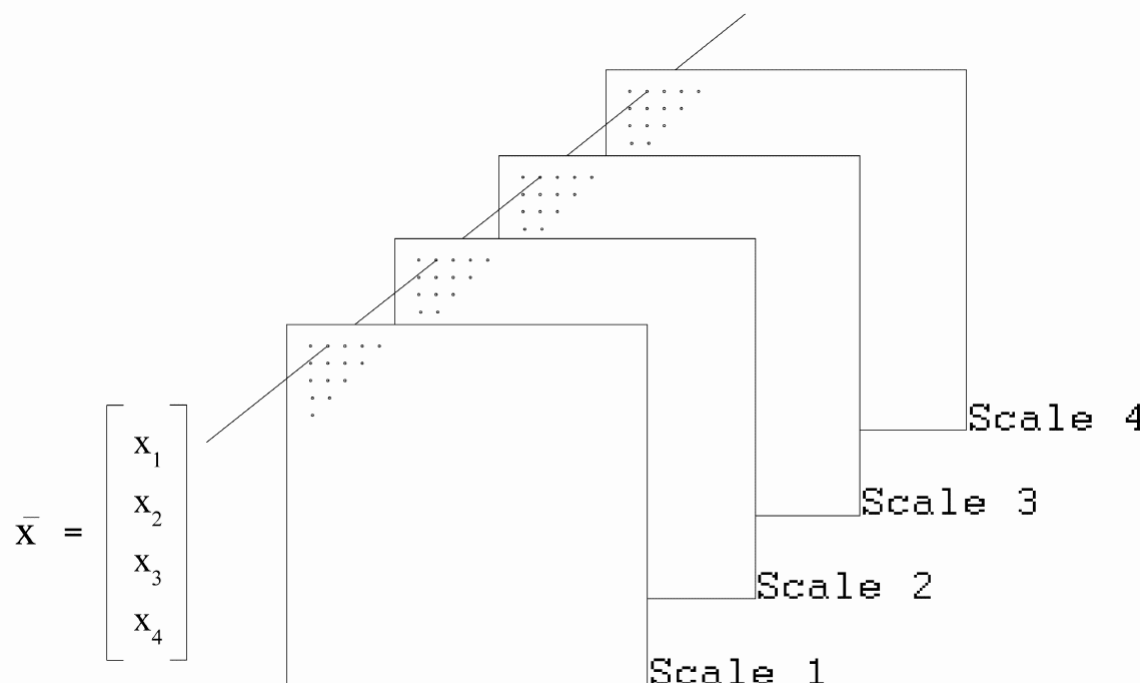


Figure 8.58: Formation of the vector $\mathbf{x} = \bar{x}$ from the corresponding pixels of the same orientation and four scales. Reproduced with permission from R.J. Ferrari, R.M. Rangayyan, J.E.L. Desautels, and A.F. Frère, “Analysis of asymmetry in mammograms via directional filtering with Gabor wavelets”, *IEEE Transactions on Medical Imaging*, 20(9): 953 – 964, 2001. © IEEE.



The vectors corresponding to each position in the filter responses were used to compute the mean vector μ and the covariance matrix σ .

The eigenvectors of the covariance matrix were computed and arranged in a matrix A in descending order of the corresponding eigenvalues.

The first N principal components corresponding to 95% of the total variance were selected, and used to represent the oriented components at each specific orientation.

The principal components were computed as $y = A(x - \mu)$.



Analysis of variance was performed by evaluating the eigenvalues of the matrix \mathbf{A} .

The KLT method is optimal in the sense that it minimizes the MSE between the vectors \mathbf{x} and their resulting approximations \mathbf{y} .

The result of application of the KLT to all orientations is a set of K images, where K is the number of orientations.



The images resulting from the KLT were thresholded by using the maximum of Otsu's threshold value (see Section 8.3.2) computed for the K images.

Phase and magnitude images, indicating the local orientation and intensity, were composed by vector summation of the K filtered images, as illustrated in Figure 8.10.

Rose diagrams were composed from the phase and magnitude images to represent the directional distribution of the fibroglandular tissue in each mammogram.

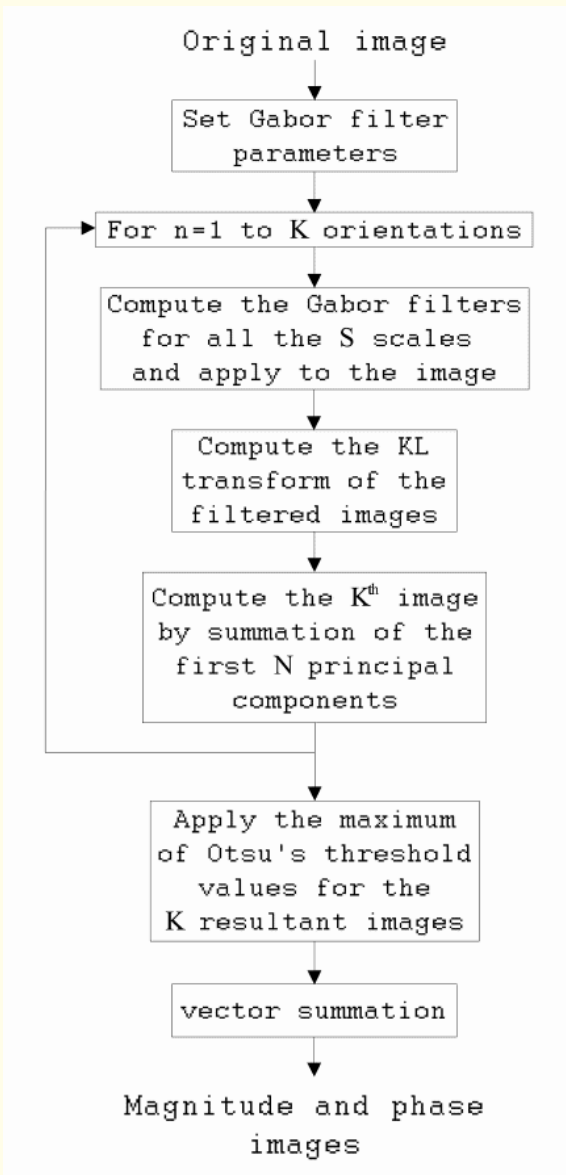


Figure 8.59: Block diagram of the procedure for directional analysis using Gabor wavelets. Reproduced with permission from R.J. Ferrari, R.M. Rangayyan, J.E.L. Desautels, and A.F. Frère, "Analysis of asymmetry in mammograms via directional filtering with Gabor wavelets", *IEEE Transactions on Medical Imaging*, 20(9): 953 – 964, 2001. © IEEE.

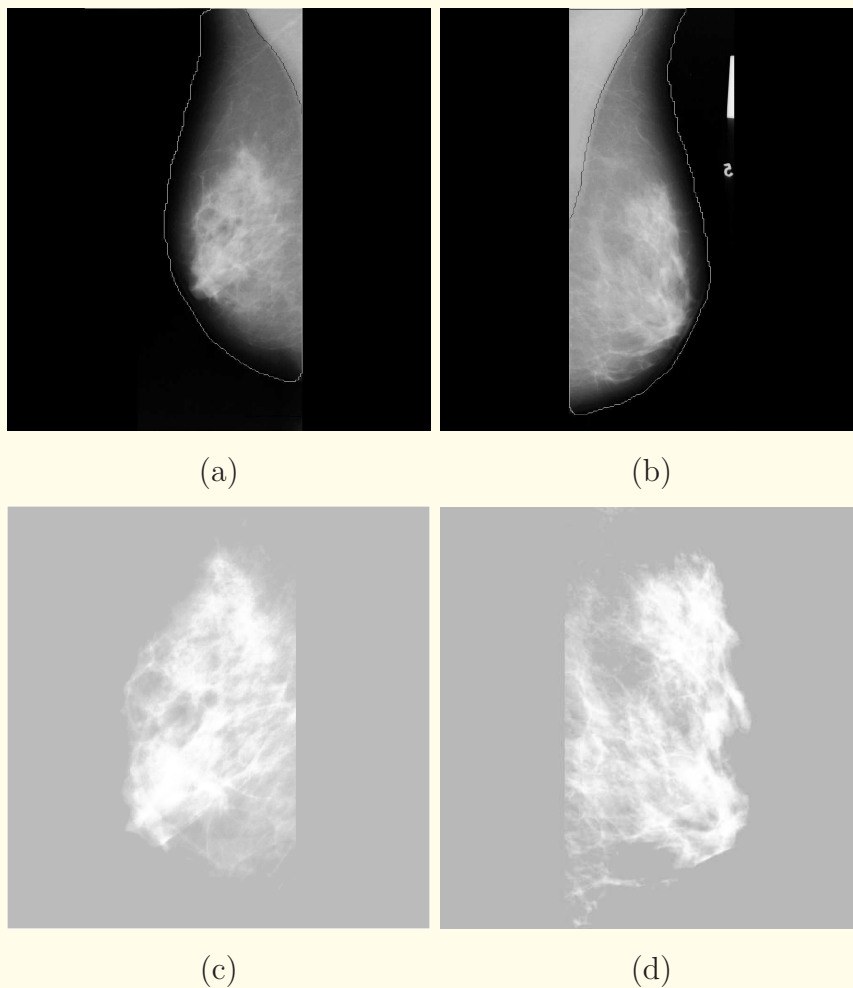


Figure 8.60: Images mdb043 and mdb044 of a normal case. (a) and (b) Original images ($1,024 \times 1,024$ pixels at $200 \mu\text{m}/\text{pixel}$). The breast boundary (white) and pectoral muscle edge (black) detected are also shown. (c) and (d) Fibroglandular discs segmented and enlarged (512×512 pixels). Histogram equalization was applied to enhance the global contrast of each ROI for display purposes only. Reproduced with permission from R.J. Ferrari, R.M. Rangayyan, J.E.L. Desautels, and A.F. Frère, “Analysis of asymmetry in mammograms via directional filtering with Gabor wavelets”, *IEEE Transactions on Medical Imaging*, 20(9): 953 – 964, 2001. © IEEE.

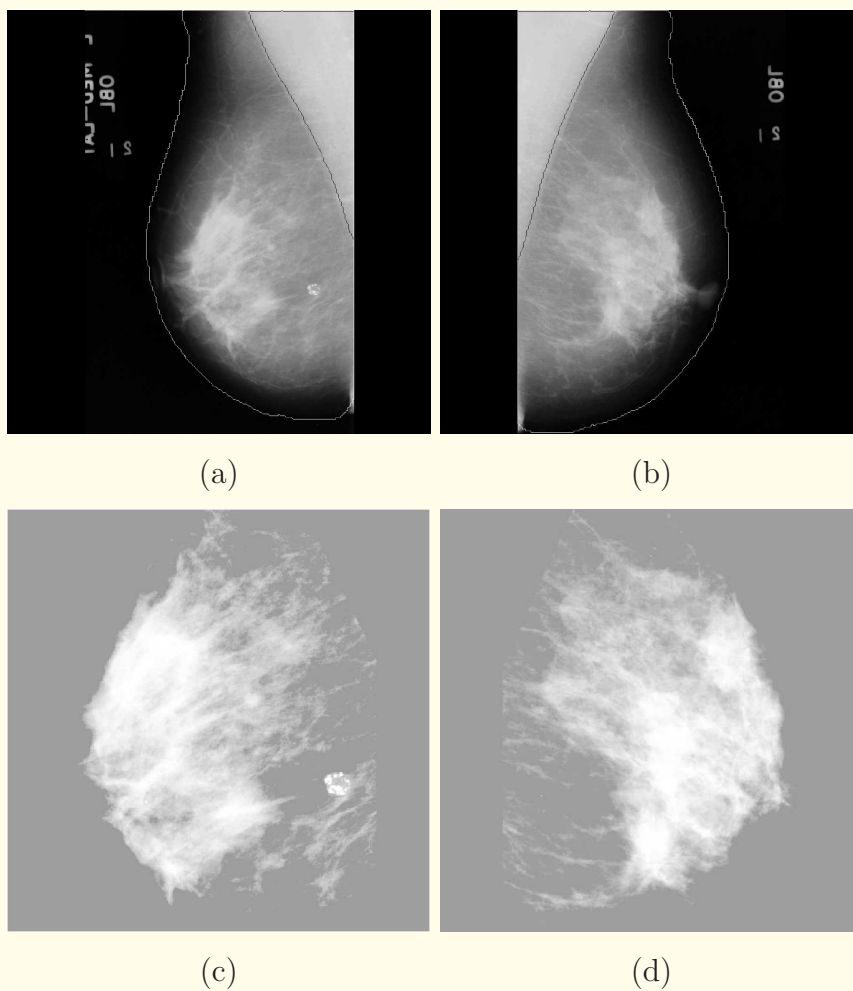


Figure 8.61: Images mdb119 and mdb120 of a case of architectural distortion. (a) and (b) Original images ($1,024 \times 1,024$ pixels at $200 \mu\text{m}/\text{pixel}$). The breast boundary (white) and pectoral muscle edge (black) detected are also shown. (c) and (d) Fibroglandular discs segmented and enlarged (512×512 pixels). Histogram equalization was applied to enhance the global contrast of each ROI for display purposes only. Reproduced with permission from R.J. Ferrari, R.M. Rangayyan, J.E.L. Desautels, and A.F. Frère, “Analysis of asymmetry in mammograms via directional filtering with Gabor wavelets”, *IEEE Transactions on Medical Imaging*, 20(9): 953 – 964, 2001. © IEEE.

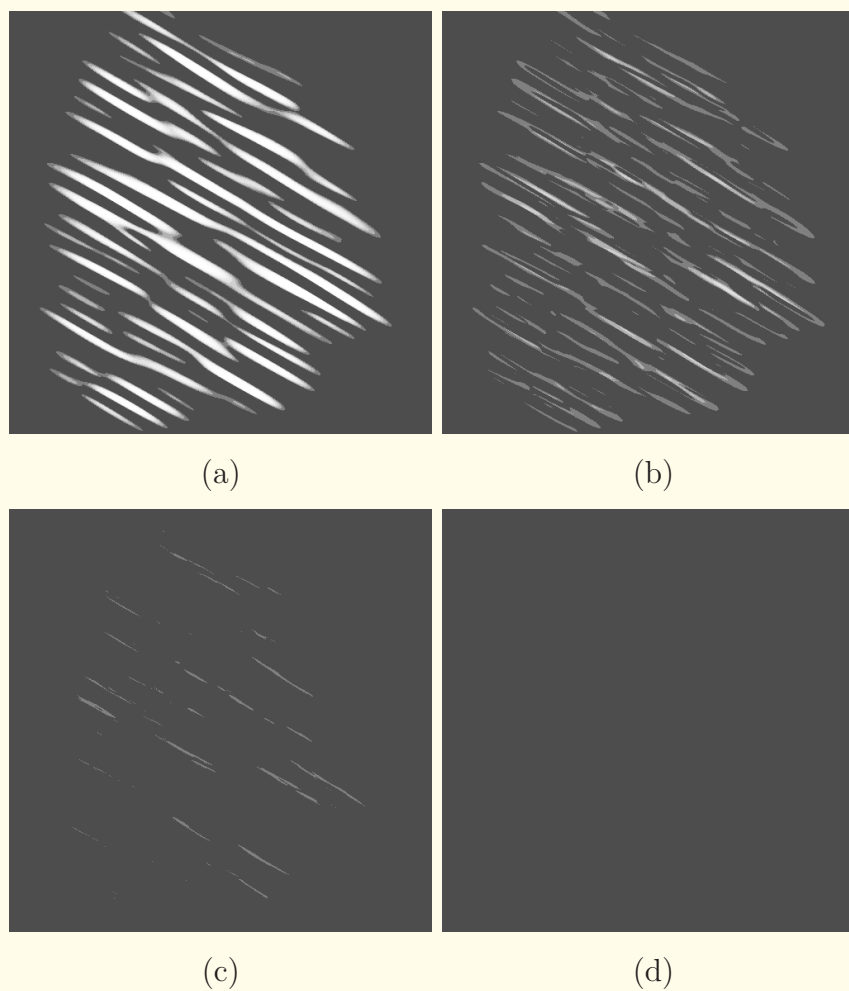


Figure 8.62: The images (a), (b), (c), and (d) are, respectively, the first, second, third, and fourth components resulting from the KLT applied to the Gabor filter responses with orientation 135° to the ROI of the image mdb120 shown in Figure 8.61 (d). The eigenvalues of the four components above are: $\lambda_1 = 10.80$, $\lambda_2 = 0.89$, $\lambda_3 = 0.09$, and $\lambda_4 = 0.01$. The images were full brightness-contrast corrected for improved visualization. Reproduced with permission from R.J. Ferrari, R.M. Rangayyan, J.E.L. Desautels, and A.F. Frère, “Analysis of asymmetry in mammograms via directional filtering with Gabor wavelets”, *IEEE Transactions on Medical Imaging*, 20(9): 953 – 964, 2001. © IEEE.

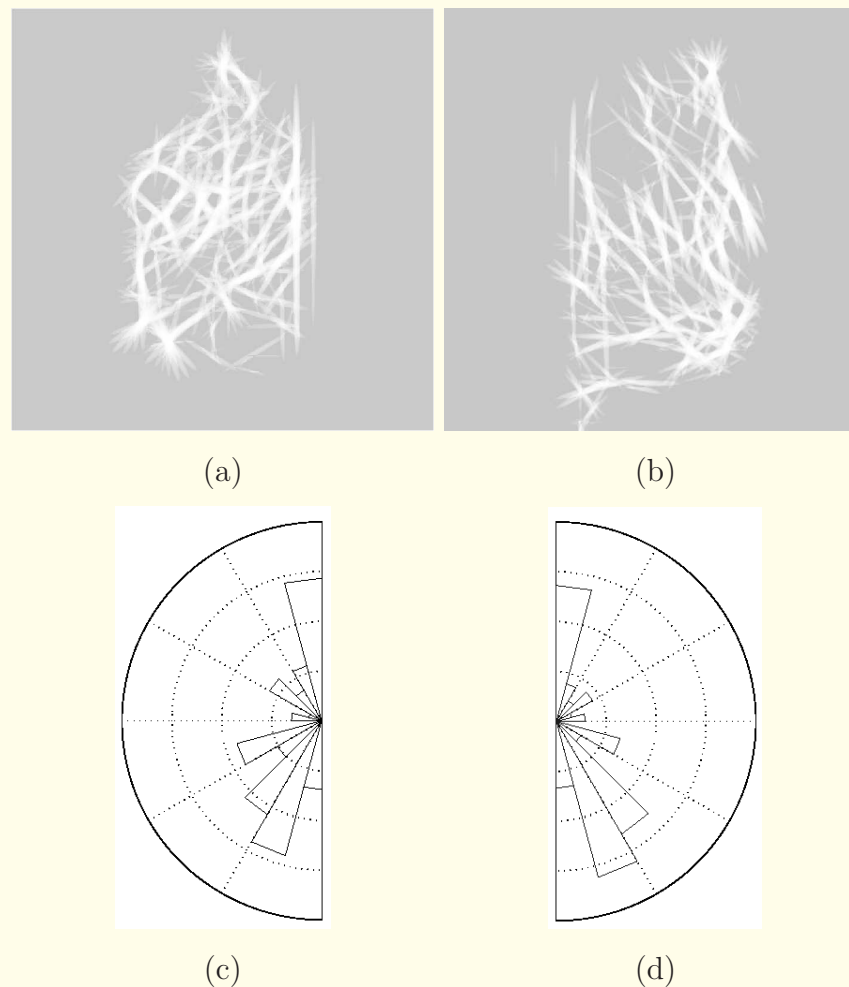


Figure 8.63: Results obtained for the normal case in Figure 8.60. (a) and (b) Magnitude images. (c) and (d) Rose diagrams. The magnitude images were histogram-equalized for improved visualization. The rose diagrams have been configured to match the mammograms in orientation. Reproduced with permission from R.J. Ferrari, R.M. Rangayyan, J.E.L. Desautels, and A.F. Frère, “Analysis of asymmetry in mammograms via directional filtering with Gabor wavelets”, *IEEE Transactions on Medical Imaging*, 20(9): 953 – 964, 2001. © IEEE.

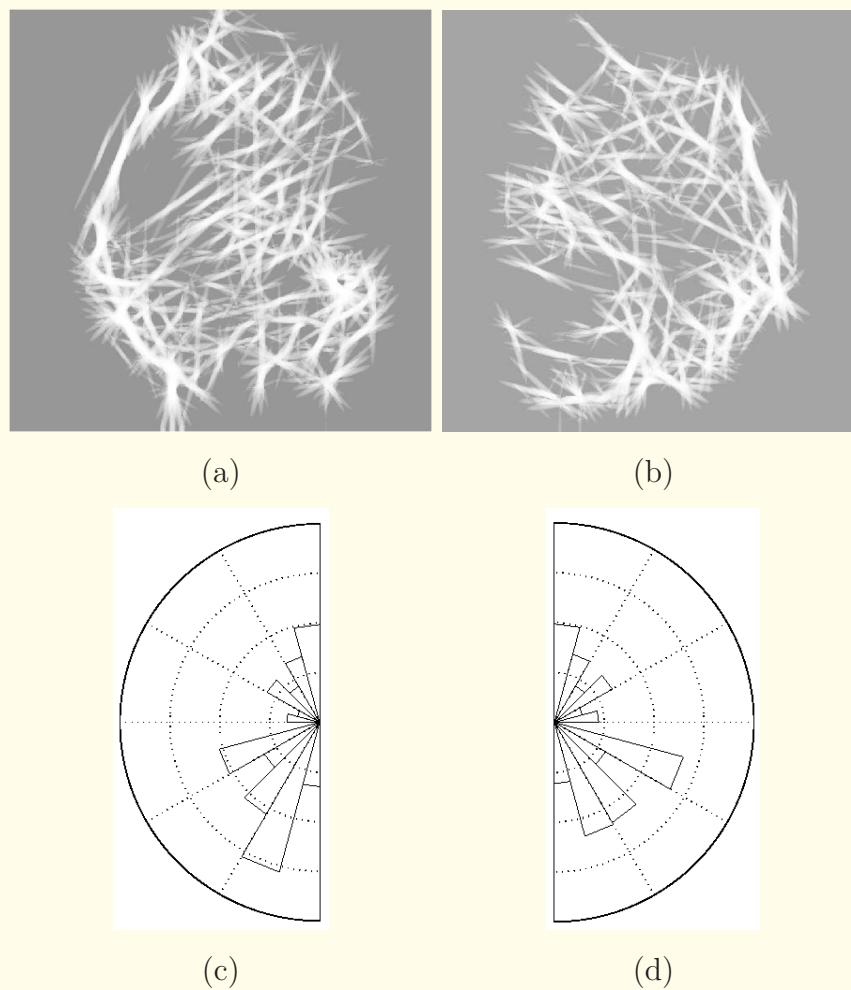


Figure 8.64: Results obtained for the case of architectural distortion in Figure 8.61. (a) and (b) Magnitude images. (c) and (d) Rose diagrams. The magnitude images were histogram-equalized for improved visualization. The rose diagrams have been configured to match the mammograms in orientation. Reproduced with permission from R.J. Ferrari, R.M. Rangayyan, J.E.L. Desautels, and A.F. Frère, “Analysis of asymmetry in mammograms via directional filtering with Gabor wavelets”, *IEEE Transactions on Medical Imaging*, 20(9): 953 – 964, 2001. © IEEE.



8.9.6 *Characterization of bilateral asymmetry*

Feature extraction and pattern classification:

To characterize bilateral asymmetry in an objective manner, three features were derived:

the entropy H (Equation 8.10),

the first moment M_1 (Equation 8.6),

and the second central moment or variance M_2 (Equation 8.7) of the rose diagram given by the difference between the rose diagrams computed for the left and right mammograms.



Classification of the normal and asymmetric cases was conducted by using the Bayesian linear classifier.

The Gaussian distribution was assumed in order to model the PDF, and the parameters of the model were estimated by using the training samples.

The prior probabilities of the normal and asymmetry classes were assumed to be equal, and the covariance matrix was calculated in a pooled manner by averaging the covariance matrices of the normal and asymmetric classes.

The leave-one-out methodology was used to estimate the classification accuracy.



The directional analysis scheme was applied to 80 images: 20 normal cases, 14 cases of asymmetry, and six cases of architectural distortion from the Mini-MIAS database.

An exhaustive combination approach was used to select the best set of features.

The selection was conducted based upon the classification results obtained by using the leave-one-out method.

The best result, by using only one feature in the classification process, was achieved by the first-order angular moment (M_1), with the sensitivity, specificity, and average accuracy values equal to 77.3%, 71.4%, and 74.4%.



When using two features, the best result was achieved with the combination of the first-order angular moment (M_1) and the entropy (H) features: 80% of the asymmetric and distortion cases, and 65% of the normal cases were correctly classified.

The average rate of correct classification in this case was 72.5%.

The low rate of specificity may be explained by the fact that even normal cases present natural signs of mild asymmetry;

the mammographic imaging procedure may also distort the left and right breasts in different ways.



In a subsequent study, Rangayyan et al. revised the directional analysis procedures as shown in Figure 8.65.

The rose diagrams of the left and right mammograms were aligned such that their mean angles corresponded to the straight line perpendicular to the pectoral muscle, and then subtracted to obtain the difference rose diagram.

In addition to the features H , M_1 , and M_2 of the difference rose diagram as described above, the dominant orientation θ_R and circular variance s_θ^2 were computed.



$$X_R = \sum_{i=1}^N R_i \cos \theta_i, \quad (8.83)$$

$$Y_R = \sum_{i=1}^N R_i \sin \theta_i, \quad (8.84)$$

$$\theta_R = \arctan \left(\frac{Y_R}{X_R} \right), \quad (8.85)$$

$$s_\theta^2 = 1 - \sqrt{X_R^2 + Y_R^2}, \quad (8.86)$$

where R_i is the normalized value and θ_i is the central angle of the i^{th} angle band of the difference rose diagram,

and N is the number of bins in the rose diagram.

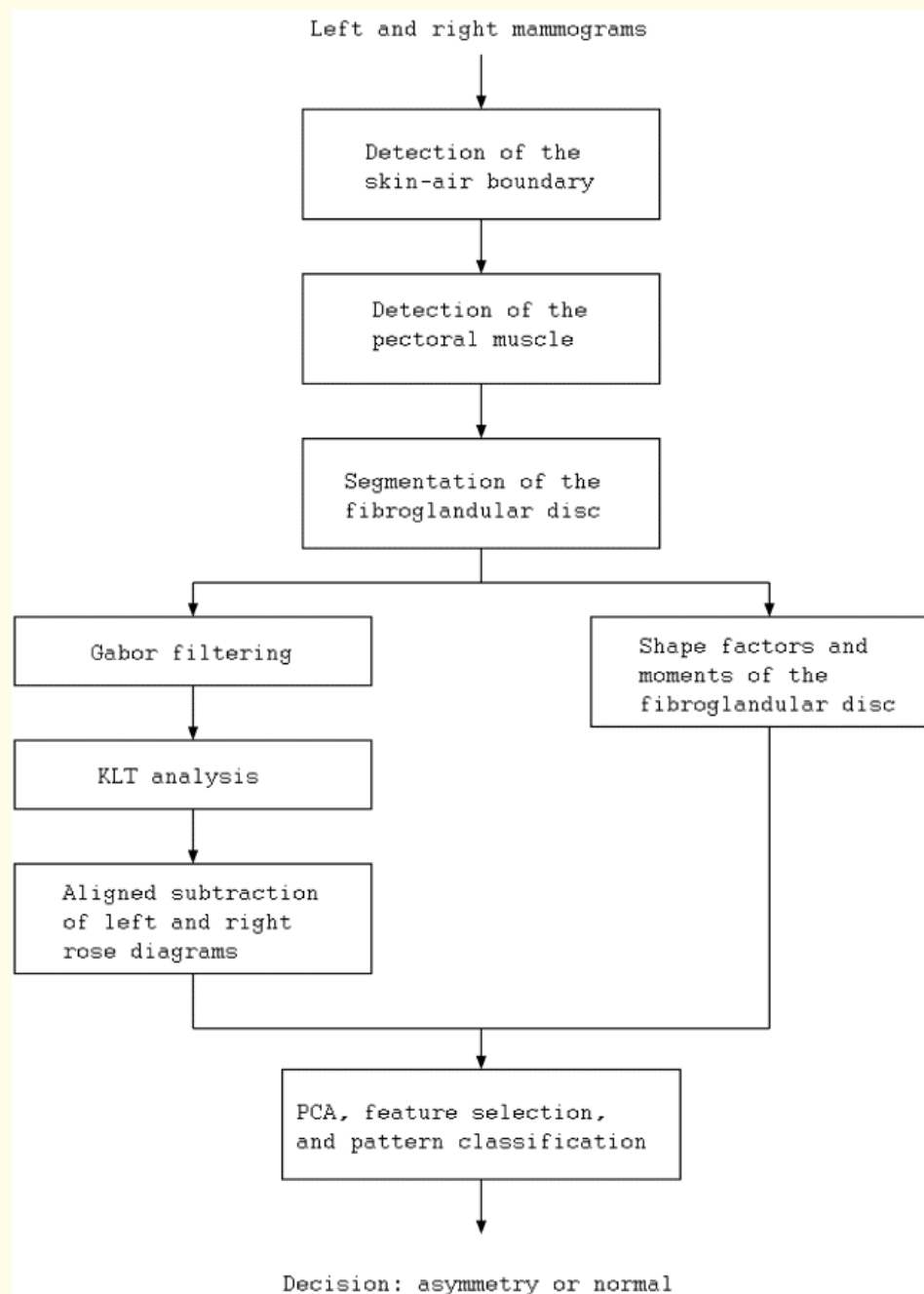


Figure 8.65: Block diagram of the revised procedure for the analysis of bilateral asymmetry.



In addition, a set of 11 features including seven of Hu's moments (see Section 6.2.2 and Equation 8.3) and the area, average density, eccentricity η , and stretch ρ were computed to characterize the shape of the segmented fibroglandular discs.

Eccentricity was computed as

$$\eta = \frac{(m_{20} - m_{02})^2 + 4m_{11}^2}{(m_{20} + m_{02})^2}, \quad (8.87)$$

where m_{pq} are the geometric invariant moments as described in Section 6.2.2.



The stretch parameter was computed as

$$\rho = \frac{x_{\max} - x_{\min}}{y_{\max} - y_{\min}}, \quad (8.88)$$

where x_{\max} , x_{\min} , y_{\max} , and y_{\min} are the corner coordinates of the rectangle delimiting the fibroglandular disc.

Feature selection was performed by PCA and exhaustive combination techniques.

With PCA, only the components associated with 98% of the total variance were used in the classification step.



Classification was performed using linear and quadratic Bayesian classifiers with the leave-one-out method.

The revised directional analysis scheme was applied to 88 images: 22 normal cases, 14 cases of asymmetry, and eight cases of architectural distortion from the Mini-MIAS database.

The best overall classification accuracy of 84.4% (with a sensitivity of 82.6% and specificity of 86.4%) was obtained using the four features θ_R , M_1 , M_2 , and H computed from the aligned-difference rose diagrams using the quadratic classifier.

The morphometric measures and moments, after PCA-based feature selection, resulted in an overall classification accuracy of only 71.1% with the linear classifier.



The combination of all of the directional statistics, morphometric measures, and moments, after PCA-based feature selection, resulted in an overall classification accuracy of 82.2%, with a sensitivity of 78.3% and specificity of 86.4% with the linear classifier.

The results indicate the importance of directional analysis of the fibroglandular tissue in the detection of bilateral asymmetry.



8.10 Application: Architectural Distortion in Mammograms

Architectural distortion is defined in BI-RADSTM as follows:

“The normal architecture (of the breast) is distorted with no definite mass visible. This includes spiculations radiating from a point and focal retraction or distortion at the edge of the parenchyma.”.

According to van Dijck et al., “in nearly half of the screen-detected cancers, minimal signs appeared to be present on the previous screening mammogram two years before the diagnosis”.



Burrell et al., in a study of screening interval breast cancers, showed that architectural distortion is the most commonly missed abnormality in false-negative cases.

Broeders et al. suggested that improvement in the detection of architectural distortion could lead to an effective improvement in the prognosis of breast cancer patients.



8.10.1 Detection of spiculated lesions and distortion

The breast contains several piecewise linear structures, such as ligaments, ducts, and blood vessels, that cause oriented texture in mammograms.

The presence of architectural distortion is expected to change the normal oriented texture of the breast.

Ayres and Rangayyan proposed the application of Gabor filters and phase portraits to detect sites of architectural distortion in full mammograms.

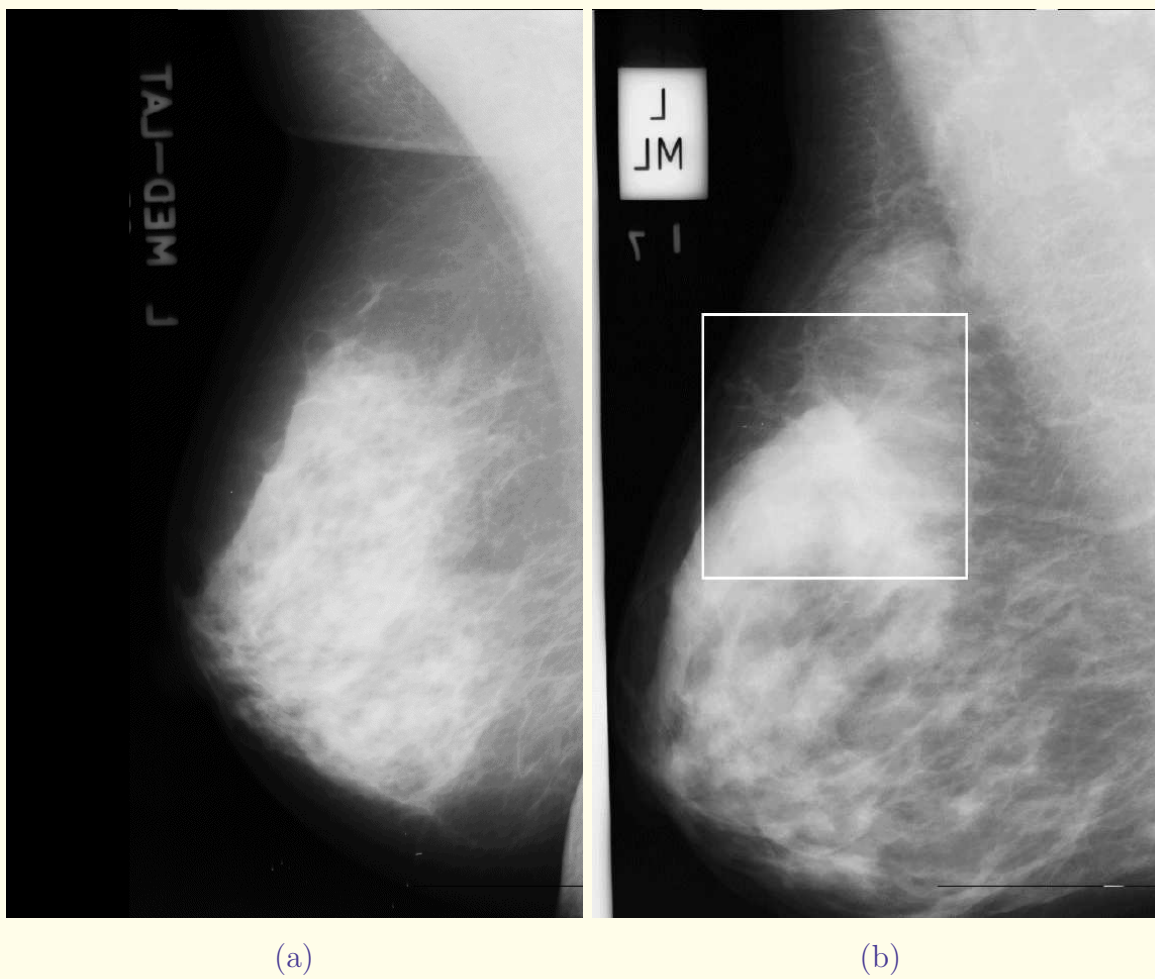


Figure 8.66: (a) Mammogram showing a normal breast; image mdb243 from the Mini-MIAS database. Width of image = 650 pixels = 130 mm. (b) Architectural distortion present in a mammogram from the Mini-MIAS database (mdb115). Width of image = 650 pixels = 130 mm. The square box overlaid on the figure represents the ROI including the site of architectural distortion, shown enlarged in Figure 8.67. Reproduced with permission from F.J. Ayres and R.M. Rangayyan, “Characterization of architectural distortion in mammograms via analysis of oriented texture”, *IEEE Engineering in Medicine and Biology Magazine*, January 2005. © IEEE.

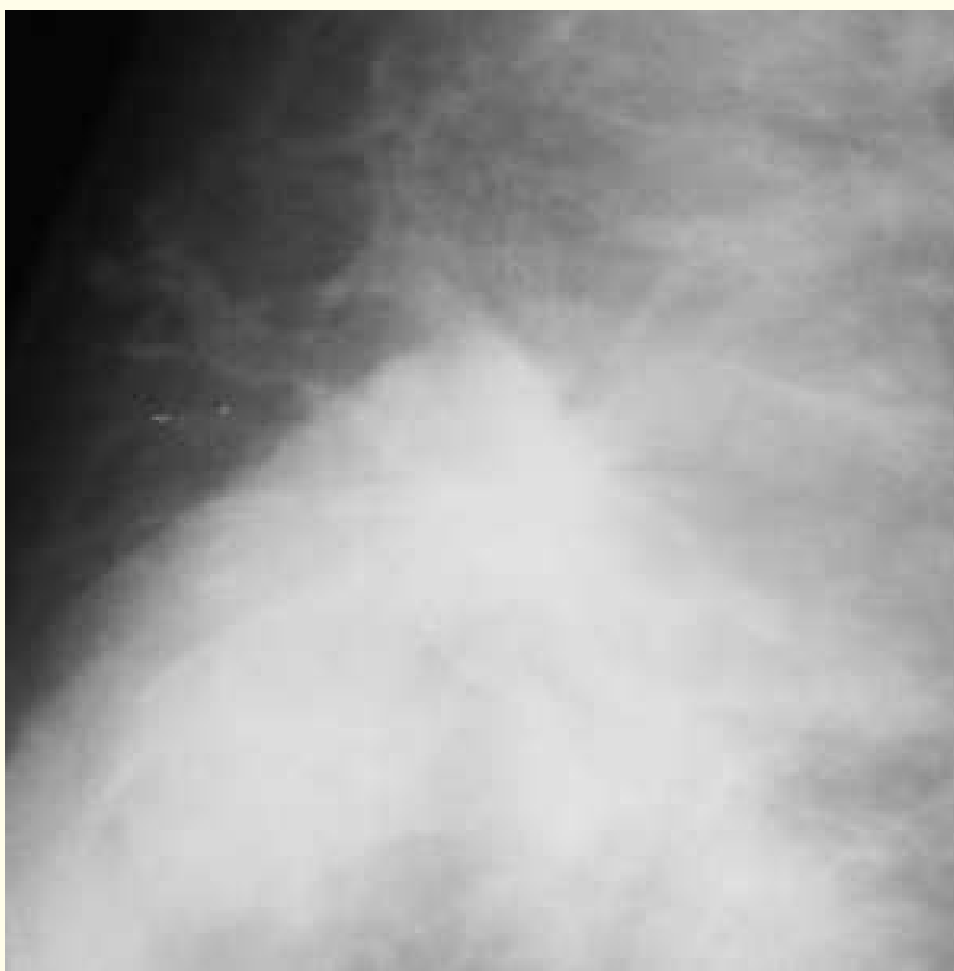


Figure 8.67: Detail of mammogram mdb115 showing the site of architectural distortion marked by the box in Figure 8.66 (b). Width of image = 300 pixels = 60 mm. Reproduced with permission from F.J. Ayres and R.M. Rangayyan, “Characterization of architectural distortion in mammograms via analysis of oriented texture”, *IEEE Engineering in Medicine and Biology Magazine*, January 2005. © IEEE.



8.10.2 Phase portraits

Phase portraits provide an analytical tool to study systems of first-order differential equations.

The method is useful in characterizing oriented texture.

Let $p(t)$ and $q(t)$ denote two differentiable functions of time t , related by a system of first-order differential equations as

$$\begin{aligned}\dot{p}(t) &= F[p(t), q(t)] \\ \dot{q}(t) &= G[p(t), q(t)] ,\end{aligned}\tag{8.89}$$

where the dot above the variable indicates the first-order derivative of the function with respect to time, and F and G represent functions of p and q .



Given initial conditions $p(0)$ and $q(0)$, the solution $[p(t), q(t)]$ to Equation 8.89 can be viewed as a parametric trajectory of a hypothetical particle, placed at $[p(0), q(0)]$ at time $t = 0$ and moving through the (p, q) plane with velocity $[\dot{p}(t), \dot{q}(t)]$.

The (p, q) plane is referred to as the *phase plane* of the system of first-order differential equations.

The path traced by the hypothetical particle is called a *streamline* of the vector field (\dot{p}, \dot{q}) .

The *phase portrait* is a graph of the possible streamlines in the phase plane.



A *fixed point* of Equation 8.89 is a point in the phase plane where $\dot{p}(t) = 0$ and $\dot{q}(t) = 0$:
a particle left at a fixed point remains stationary.

When the system of first-order differential equations is linear, Equation 8.89 assumes the form

$$\begin{bmatrix} \dot{p}(t) \\ \dot{q}(t) \end{bmatrix} = \mathbf{A} \begin{bmatrix} p(t) \\ q(t) \end{bmatrix} + \mathbf{b}, \quad (8.90)$$

where \mathbf{A} is a 2×2 matrix and \mathbf{b} is a 2×1 matrix.

In this case, there are only three types of phase portraits:
node, saddle, and spiral.



The type of phase portrait can be determined from the nature of the eigenvalues of \mathbf{A} , as shown in Table 8.4.

The center (p_0, q_0) of the phase portrait is given by the fixed point of Equation 8.90:

$$\begin{bmatrix} \dot{p}(t) \\ \dot{q}(t) \end{bmatrix} = 0 \Rightarrow \begin{bmatrix} p_0 \\ q_0 \end{bmatrix} = -\mathbf{A}^{-1}\mathbf{b}. \quad (8.91)$$



Solving Equation 8.90 yields a linear combination of complex exponentials for $p(t)$ and $q(t)$, whose exponents are given by the eigenvalues of A multiplied by the time variable t .

Table 8.4 illustrates the streamlines obtained by solving Equation 8.90 for a node, a saddle, and a spiral phase portrait.

The solid lines indicate the movement of the $p(t)$ and the $q(t)$ components of the solution.

The dashed lines indicate the streamlines.



The formation of each phase portrait type is explained as follows:

- *Node*: the components $p(t)$ and $q(t)$ are exponentials that either simultaneously converge to, or diverge from, the fixed-point coordinates p_0 and q_0 .
- *Saddle*: the components $p(t)$ and $q(t)$ are exponentials; while one of the components [either $p(t)$ or $q(t)$] converges to the fixed point, the other diverges from the fixed point.
- *Spiral*: the components $p(t)$ and $q(t)$ are exponentially modulated sinusoidal functions — the resulting streamline forms a spiral curve.



Associating the functions $p(t)$ and $q(t)$ with the x and y coordinates of the Cartesian (image) plane, we can define the *orientation field* generated by Equation 8.90 as

$$\phi(x, y | \mathbf{A}, \mathbf{b}) = \arctan \left[\frac{\dot{q}(t)}{\dot{p}(t)} \right], \quad (8.92)$$

which is the angle of the velocity vector $[\dot{p}(t), \dot{q}(t)]$ with the x axis at $(x, y) = [p(t), q(t)]$.

Table 8.4 lists the three phase portraits and the corresponding orientation fields generated by a system of linear first-order differential equations.



Table 8.4: Phase Portraits for a System of Linear First-order Differential Equations.

Phase portrait type	Eigenvalues	Streamlines	Appearance of the orientation field
Node	Real eigenvalues of same sign		
Saddle	Real eigenvalues of opposite sign		
Spiral	Complex eigenvalues		

Solid lines indicate the movement of the $p(t)$ and the $q(t)$ components of the solution; dashed lines indicate the streamlines. Reproduced with permission from F.J. Ayres and R.M. Rangayyan, “Characterization of architectural distortion in mammograms via analysis of oriented texture”, *IEEE Engineering in Medicine and Biology Magazine*, January 2005. © IEEE.



Using the concepts presented above, the orientation field of a textured image may be described qualitatively by determining the type of the phase portrait that is most similar to the orientation field, along with the center of the phase portrait.

This notion was employed by Ayres and Rangayyan to characterize architectural distortion.



8.10.3 Estimating the orientation field

To extract the texture orientation at each pixel, the image was filtered with a bank of Gabor filters of different orientations.

The basic Gabor filter kernel was formulated as

$$g(x, y) = \frac{1}{2\pi\sigma_x\sigma_y} \exp \left[-\frac{1}{2} \left(\frac{x^2}{\sigma_x^2} + \frac{y^2}{\sigma_y^2} \right) \right] \cos(2\pi f_o x). \quad (8.93)$$

Kernels at other angles were obtained by rotating this kernel.

A set of 180 kernels was used, with angles spaced evenly over the range $[-\pi/2, \pi/2]$.



Gabor filters may be used as line detectors.

In the work of Ayres and Rangayyan, the parameters in Equation 8.93, namely σ_x , σ_y , and f_o , were derived from a design rule as follows.

Let τ be the thickness of the line detector.

This parameter constrains σ_x and f_o as follows:

- The amplitude of the exponential term in Equation 8.93, that is, the Gaussian term, is reduced to one half of its maximum at $x = \tau/2$ and $y = 0$; therefore, $\sigma_x = \tau/(2\sqrt{2 \ln 2})$.
- The cosine term has a period of τ ; therefore, $f_o = 1/\tau$.



The value of σ_y was defined as $\sigma_y = l \sigma_x$, where l determines the elongation of the Gabor filter in the orientation direction, with respect to its thickness.

The values $\tau = 4$ pixels (0.8 mm at a pixel size of $200 \mu\text{m}$) and $l = 8$ were determined by observing the typical spicule width and length in mammograms with architectural distortion.

The effects of the different design parameters are shown in Figure 8.68.

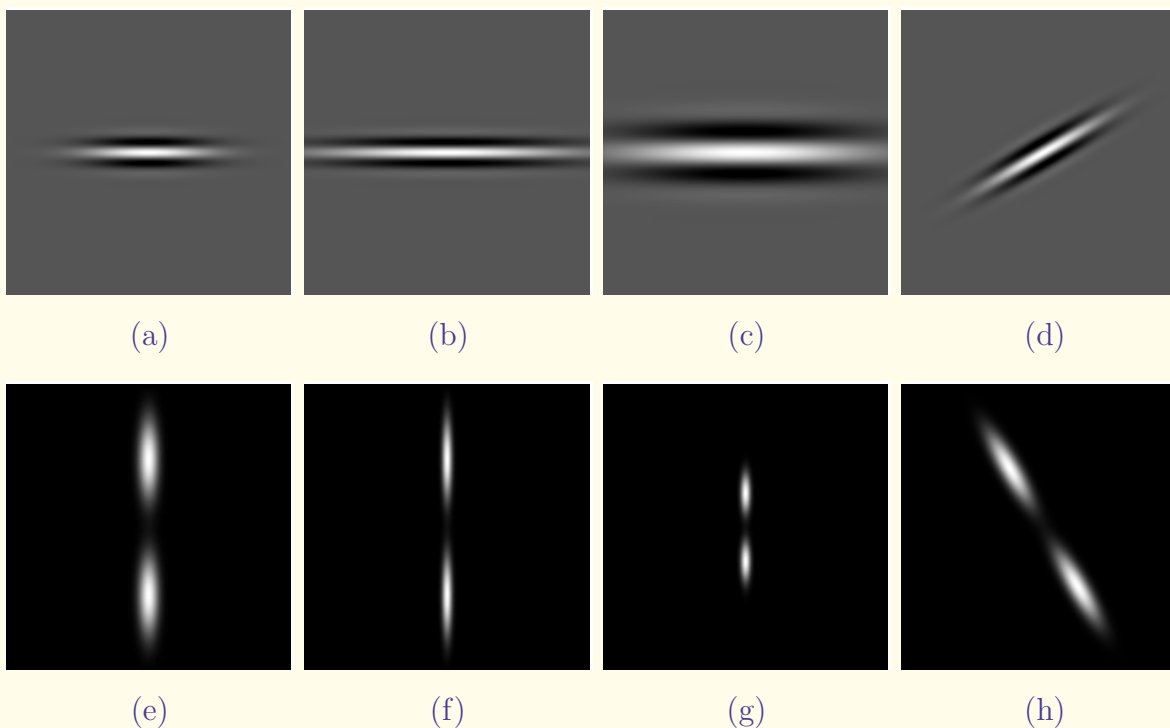


Figure 8.68: Effects of the different parameters of the Gabor filter. (a) Example of the impulse response of a Gabor filter. (b) The parameter l is increased: the Gabor filter is elongated in the x direction. (c) The parameter τ is increased: the Gabor filter is enlarged in the x and y directions. (d) The angle of the Gabor filter is modified. Figures (e) – (h) correspond to the magnitude of the Fourier transforms of the Gabor filters in (a) – (d), respectively. The $(0, 0)$ frequency component is at the center of the spectra displayed. Reproduced with permission from F.J. Ayres and R.M. Rangayyan, “Characterization of architectural distortion in mammograms via analysis of oriented texture”, *IEEE Engineering in Medicine and Biology Magazine*, January 2005. © IEEE.



The texture orientation at a pixel was estimated as the orientation of the Gabor filter that yielded the highest magnitude response at that pixel.

The orientation at every pixel was used to compose the *orientation field*.

The magnitude of the corresponding filter response was used to form the *magnitude image*.

The magnitude image was not used in the estimation of the phase portrait, but was found to be useful for illustrative purposes.



Let $\theta(x, y)$ be the texture orientation at (x, y) , and

$g_k(x, y)$, $k = 0, 1, \dots, 179$, be the Gabor filter oriented at

$$\alpha_k = -\pi/2 + \pi k/180.$$

Let $f(x, y)$ be the image being processed, and

$$f_k(x, y) = (f * g_k)(x, y),$$

where the asterisk denotes linear 2D convolution.

Then, the orientation field of $f(x, y)$ is given by

$$\theta(x, y) = \alpha_{k_{\max}} \text{ where } k_{\max} = \arg\left\{\max_k [|f_k(x, y)|]\right\}. \quad (8.94)$$



8.10.4 Characterizing orientation fields with phase portraits

In the work of Ayres and Rangayyan, a sliding analysis window was used for the estimation of \mathbf{A} and \mathbf{b} .

For every point (x, y) , let

$$\Delta(x, y) = \sin[\theta(x, y) - \phi(x, y | \mathbf{A}, \mathbf{b})]$$

represent the error between the orientation of the texture given by Equation 8.94 and the orientation of the model given by Equation 8.92.



Then, the estimation problem is that of finding \mathbf{A} and \mathbf{b} that minimize the sum of the squared error

$$\epsilon^2 = \sum_x \sum_y \Delta^2(x, y) = \sum_x \sum_y \{\sin[\theta(x, y) - \phi(x, y | \mathbf{A}, \mathbf{b})]\}^2, \quad (8.95)$$

which may be solved using a nonlinear least-squares algorithm.



The given image was analyzed by sliding the analysis window through the orientation field, and accumulating the information obtained, that is, the type of the phase portrait and the location of the fixed point, for each window position, as follows:

1. Create three maps, one for each type of phase portrait (called the *phase portrait maps*), that will be used to accumulate information from the sliding analysis window. The maps are initialized to zero, and are of the same size as the image being processed.
2. Slide the analysis window through the orientation field of the ROI. At each position of the sliding window, determine the type of the phase portrait and compute the fixed point.
3. Increment the value at the location of the fixed point in the corresponding phase portrait map.



The size of the sliding analysis window was set at 44×44 pixels ($8.8 \times 8.8\text{ mm}$).

The three maps obtained as above provide the results of a voting procedure, and indicate the possible locations of fixed points corresponding to texture patterns that (approximately) match the node, saddle, and spiral phase portraits.

It is possible that, for some positions of the sliding analysis window, the location of the fixed point falls outside the spatial limits of the ROI or image being processed; the votes related to such results were ignored.

The value at each location (x, y) in a phase portrait map provides the degree of confidence in determining the existence of the corresponding phase portrait type centered at (x, y) .



8.10.5 Feature extraction for pattern classification

The estimates of the fixed point for a given phase portrait pattern can be scattered around the true fixed-point position, due to

the limited precision of the estimation procedure,
the presence of multiple overlapping patterns,
the availability of limited data within the sliding analysis window,
and the presence of noise.

A local accumulation of the votes is necessary to diminish the effect of fixed-point location errors.

Ayres and Rangayyan employed a Gaussian smoothing filter with a standard deviation of 25 pixels (5 mm) for this purpose.



For the purpose of pattern classification, six features were extracted to characterize each ROI:

the maximum of each phase portrait map (three features),

and the entropy of each phase portrait map (three features).

The maximum of each map conveys information about the likelihood of the presence of the corresponding phase portrait.

The entropy relates to the uncertainty in the location of the fixed point in each map.



The entropy H of a map $h(x, y)$ was computed as

$$H[h(x, y)] = - \sum_x \sum_y \frac{h(x, y)}{S_h} \ln \left[\frac{h(x, y)}{S_h} \right], \quad (8.96)$$

$$S_h = \sum_x \sum_y h(x, y). \quad (8.97)$$

A map with a dense spatial concentration of votes is expected to have a large maximum value and a low entropy.

On the contrary, a map with a wide scatter of votes may be expected to have a low maximum and a large entropy.



8.10.6 Application to segments of mammograms

Ayres and Rangayyan analyzed a set of 106 ROIs, each of size 230×230 pixels ($46 \times 46\text{ mm}$, with a resolution of $200\text{ }\mu\text{m}$), selected from the Mini-MIAS database.

Only the central portion of 150×150 pixels of each ROI was investigated using a 44×44 sliding analysis window.

Linear discriminant analysis was performed using SPSS, with stepwise feature selection.

The sensitivity obtained was 82.4%, and the specificity was 71.9%. The fraction of cases correctly classified was 73.6%.

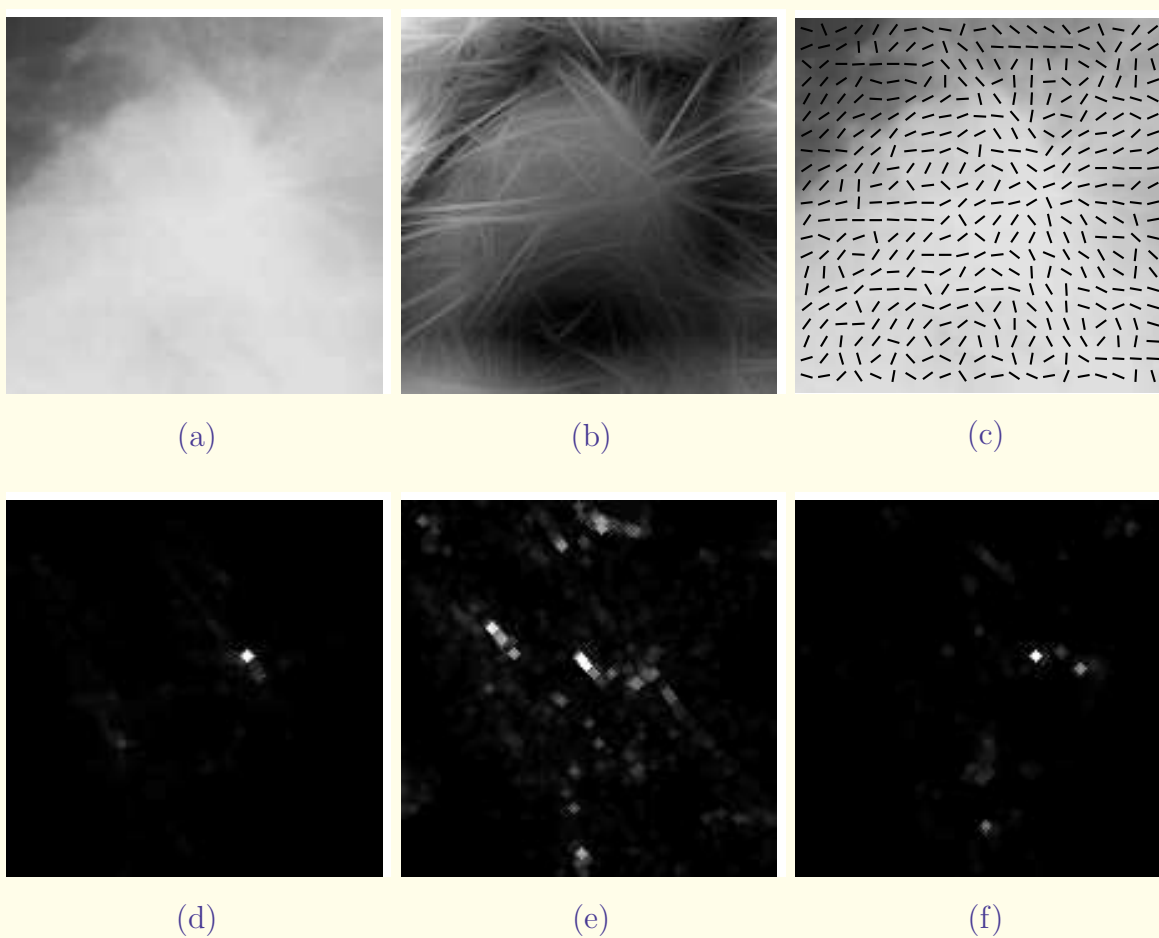


Figure 8.69: Analysis of the ROI from the image mdb115, which includes architectural distortion: (a) ROI of size 230×230 pixels (46×46 mm); (b) magnitude image; (c) orientation field superimposed on the original ROI; (d) node map, with intensities mapped from $[0, 123]$ to $[0, 255]$; (e) saddle map, $[0, 22]$ mapped to $[0, 255]$; (f) spiral map, $[0, 71]$ mapped to $[0, 255]$. This image was correctly classified as belonging to the “architectural distortion” category (Table 8.5). Reproduced with permission from F.J. Ayres and R.M. Rangayyan, “Characterization of architectural distortion in mammograms via analysis of oriented texture”, *IEEE Engineering in Medicine and Biology Magazine*, January 2005. © IEEE.



Table 8.5: Results of Linear Discriminant Analysis for ROIs with Architectural Distortion Using the Leave-one-out Method.

Architectural distortion	#ROIs	Classified as	
		Architectural distortion	Other
Benign	9	7	2
Malignant	8	6	2
Total	17	TP = 13	FN = 4

TP = true positives, FN = false negatives. The results correspond to the prior probability of belonging to the architectural distortion class being 0.465. Sensitivity = 76.5%. Reproduced with permission from F.J. Ayres and R.M. Rangayyan, “Characterization of architectural distortion in mammograms via analysis of oriented texture”, *IEEE Engineering in Medicine and Biology Magazine*, January 2005. © IEEE.



Table 8.6: Results of Linear Discriminant Analysis for ROIs Without Architectural Distortion Using the Leave-one-out Method.

Type	#ROIs	Classified as		Other
		Architectural distortion	Other	
Masses	CB	19	4	15
	SB	11	3	8
	CM	4	1	3
	SM	8	3	5
Calcifications	2	1	1	
Normal	45	9	36	
Total	89	FP = 21	TN = 68	

CB = circumscribed benign mass, CM = circumscribed malignant tumor, SB = spiculated benign mass, SM = spiculated malignant tumor, FP = false positives, TN = true negatives. The results correspond to the prior probability of belonging to the architectural distortion class being 0.465. Specificity = 76.4%. Reproduced with permission from F.J. Ayres and R.M. Rangayyan, “Characterization of architectural distortion in mammograms via analysis of oriented texture”, *IEEE Engineering in Medicine and Biology Magazine*, January 2005. © IEEE.



8.10.7 Detection of sites of architectural distortion

Ayres and Rangayyan hypothesized that architectural distortion would appear as an oriented texture pattern that can be locally approximated by a linear phase portrait model.

Before searching the maps for sites of distortion, the orientation field was filtered and downsampled as follows.

Let $h(x, y)$ be a Gaussian filter of standard deviation σ_h :

$$h(x, y) = \frac{1}{2\pi\sigma_h} \exp\left[-\frac{1}{2}\left(\frac{x^2 + y^2}{\sigma_h^2}\right)\right]. \quad (8.98)$$



Define the images $s(x, y) = \sin[2\theta(x, y)]$ and $c(x, y) = \cos[2\theta(x, y)]$, where $\theta(x, y)$ is the orientation field.

Then, the filtered orientation field $\theta_f(x, y)$ is obtained as

$$\theta_f(x, y) = \frac{1}{2} \arctan \left(\frac{h(x, y) * s(x, y)}{h(x, y) * c(x, y)} \right), \quad (8.99)$$

where the asterisk denotes 2D convolution.

The filtered orientation field was downsampled by a factor of four, thus producing the downsampled orientation field θ_d as

$$\theta_d(x, y) = \theta_f(4x, 4y). \quad (8.100)$$

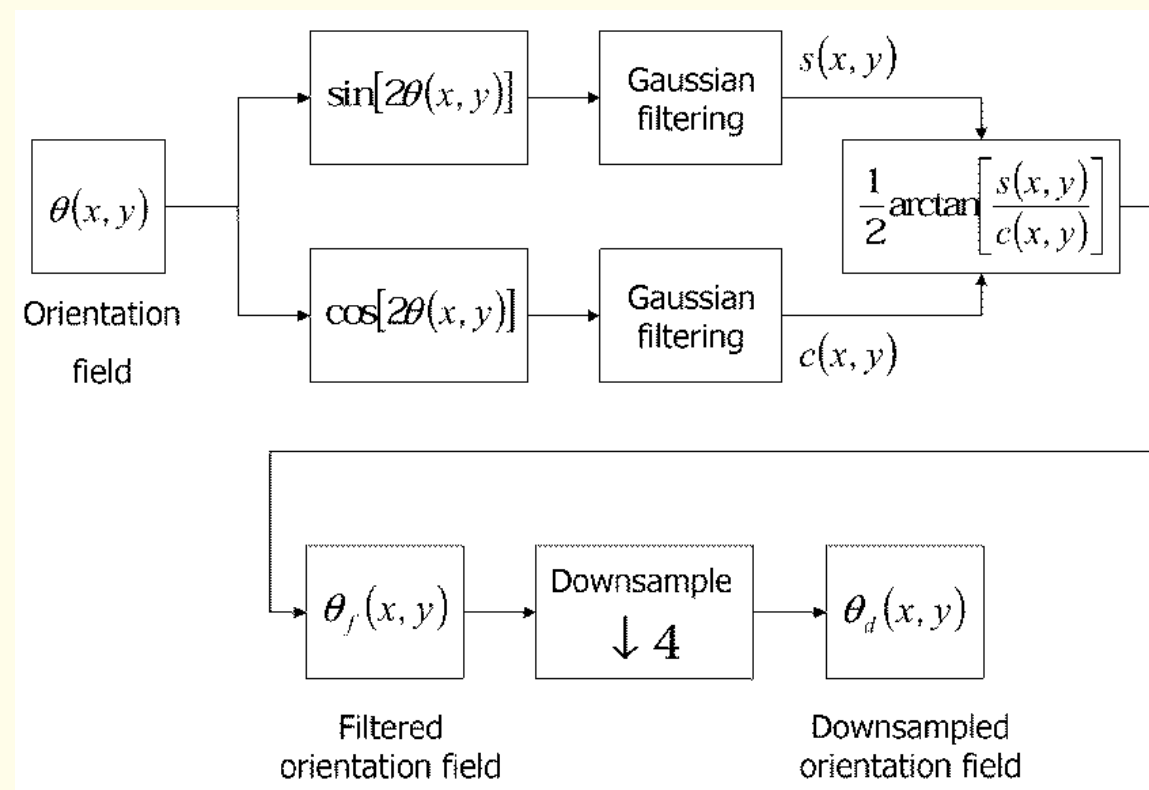


Figure 8.70: Filtering and downsampling of the orientation field. Figure courtesy of F.J. Ayres.



1. The node map is filtered with a Gaussian filter of standard deviation equal to 1.0 pixel (0.8 mm).
2. The filtered node map is thresholded.
3. The thresholded image is subjected to the following series of morphological operations to group positive responses that are close to one another, and to reduce each region of positive response to a single point. The resulting points indicate the detected locations of architectural distortion.
 - (a) A closing operation is performed to group clusters of points that are less than 8 mm apart. The structural element is a disk of radius 10 pixels (8 mm).
 - (b) A “close holes” filter is applied to the image. The resulting image includes only compact regions.
 - (c) The image is subjected to a “shrink” filter, where each compact region is shrunk to a single pixel.



The method was applied to 18 mammograms exhibiting architectural distortion, selected from the Mini-MIAS database.

The mammograms were MLO views, digitized to $1,024 \times 1,024$ pixels at a resolution of $200 \mu\text{m}$ and 8 b/pixel .

The free-response receiver operating characteristic (FROC) curve was derived by varying the threshold level in the detection step.

A sensitivity of 88% was obtained at 15 false positives per image.



Figure 8.71 (a)



(b)

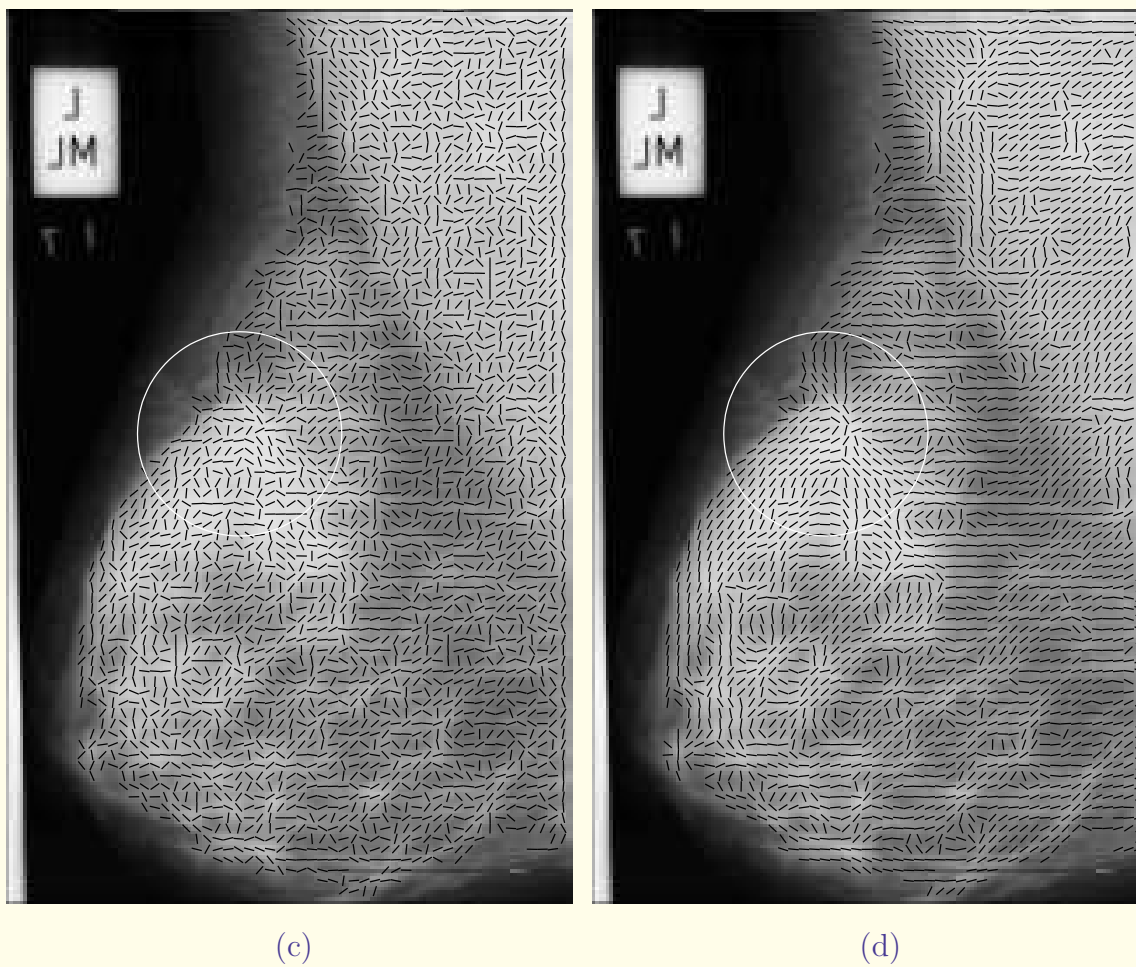


Figure 8.71: (a) Image mdb115 from the Mini-MIAS database. The circle indicates the location and the extent of architectural distortion, as provided in the Mini-MIAS database. (b) Magnitude image after Gabor filtering. (c) Orientation field superimposed on the original image. Needles have been drawn for every fifth pixel. (d) Filtered orientation field superimposed on the original image. Reproduced with permission from F.J. Ayres and R.M. Rangayyan, “Detection of architectural distortion in mammograms using phase portraits”, *Proceedings of SPIE Medical Imaging 2004: Image Processing*, Volume 5370, pp 587 – 597, 2004. © SPIE. See also Figure 8.72.

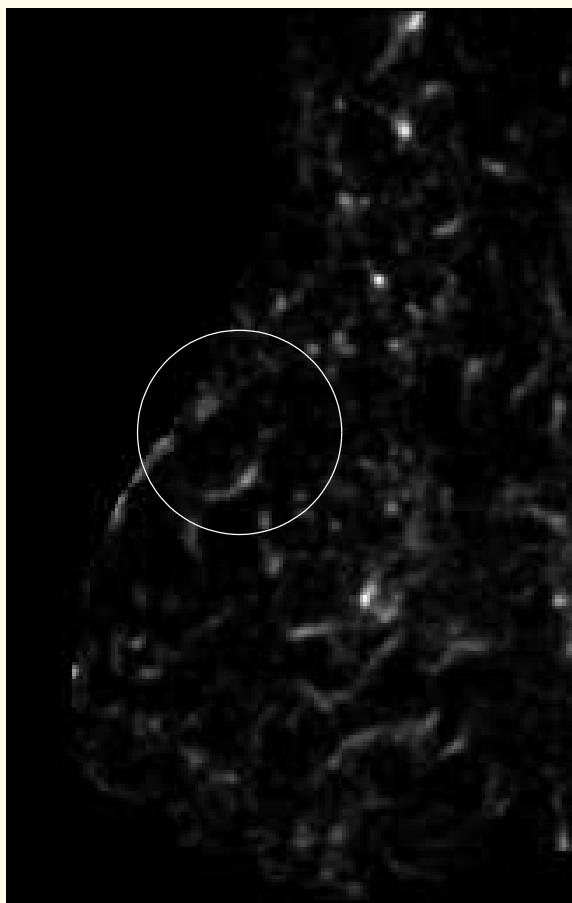


Figure 8.72 (a)



(b)

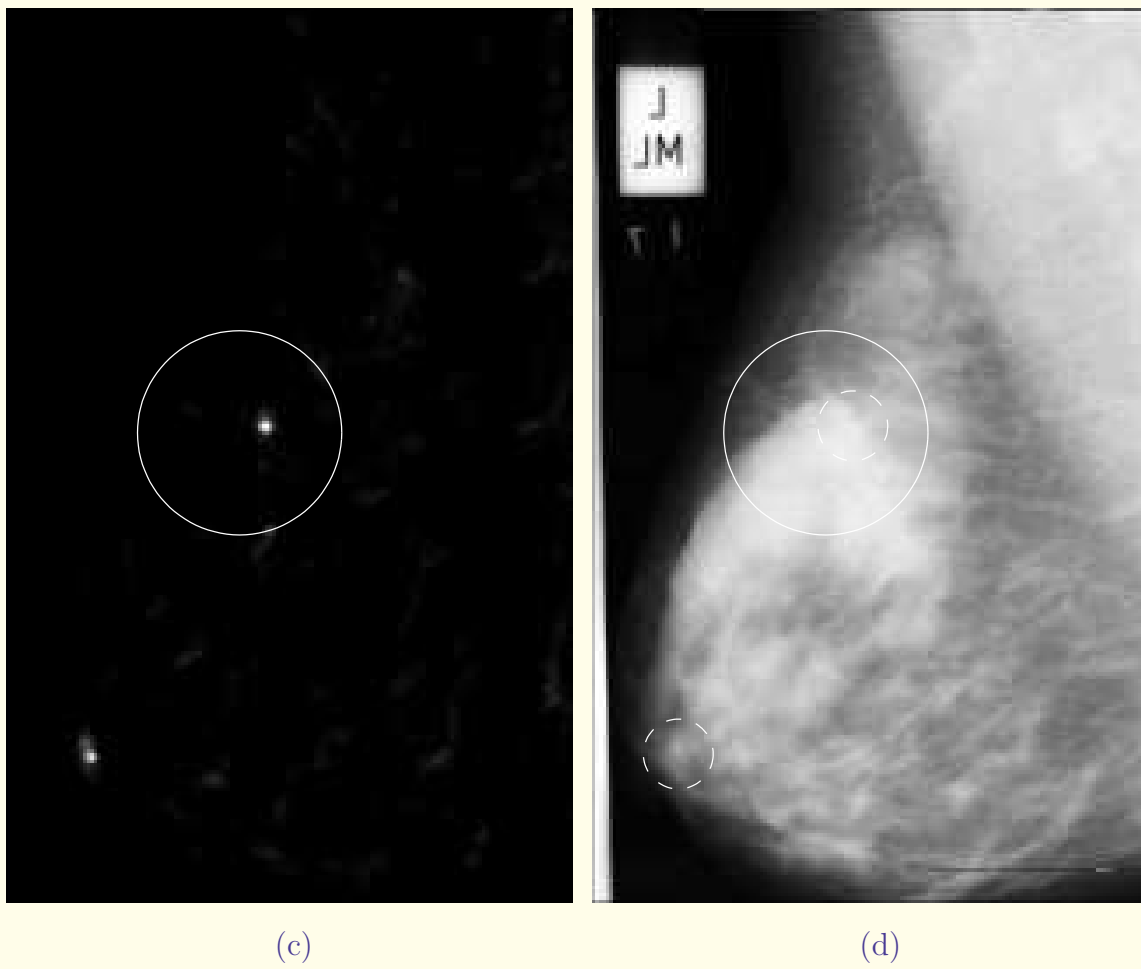


Figure 8.72: Phase portrait maps derived from the orientation field in Figure 8.71 (d), and the detection of architectural distortion. (a) Saddle map: values are scaled from the range [0, 20] to [0, 255]. (b) Spiral map: values are scaled from the range [0, 47] to [0, 255]. (a) Node map: values are scaled from the range [0, 84] to [0, 255]. (d) Detected sites of architectural distortion superimposed on the original image: the solid line indicates the location and spatial extent of architectural distortion as given by the Mini-MIAS database; the dashed lines indicate the detected sites of architectural distortion (one true positive and one false positive). Reproduced with permission from F.J. Ayres and R.M. Rangayyan, “Detection of architectural distortion in mammograms using phase portraits”, *Proceedings of SPIE Medical Imaging 2004: Image Processing*, Volume 5370, pp 587 – 597, 2004. © SPIE.

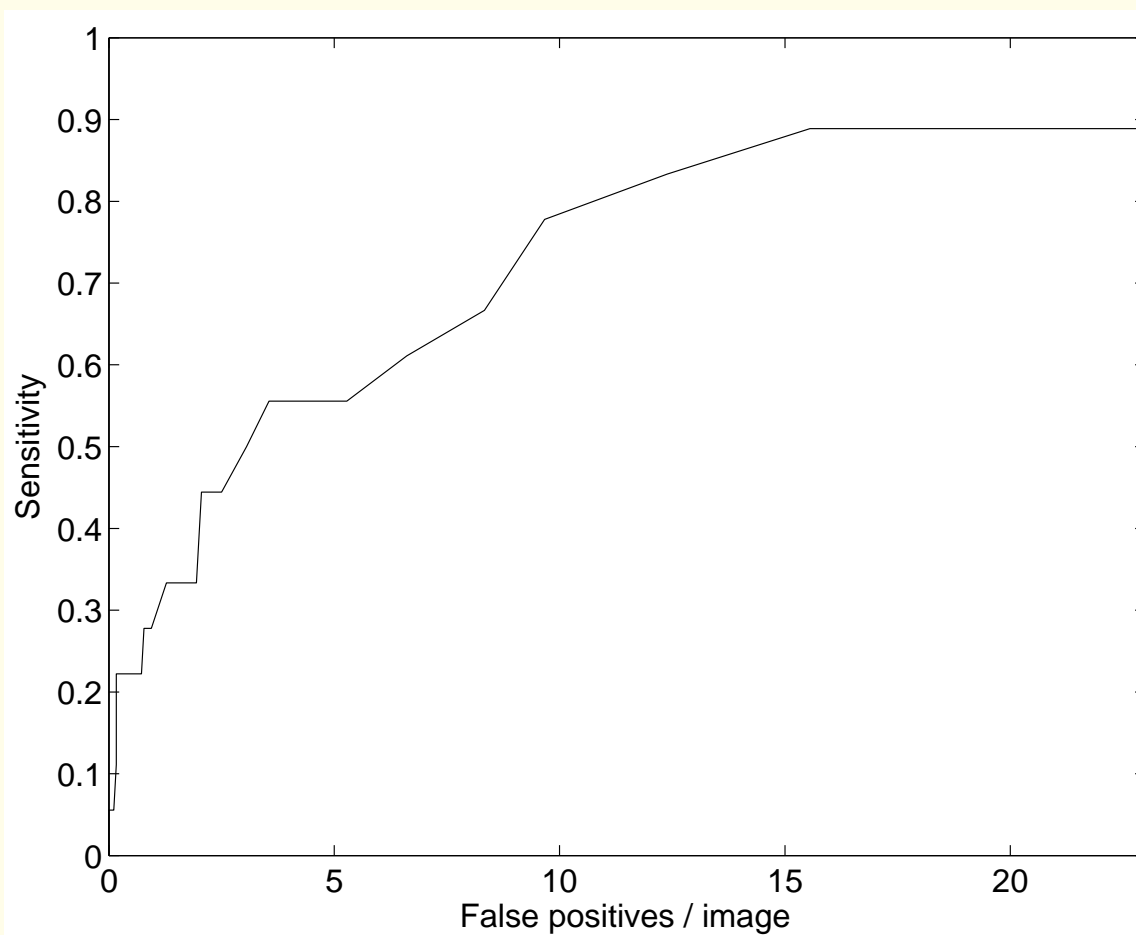


Figure 8.73: Free-response receiver operating characteristics (FROC) curve for the detection of sites of architectural distortion. Reproduced with permission from F.J. Ayres and R.M. Rangayyan, “Detection of architectural distortion in mammograms using phase portraits”, *Proceedings of SPIE Medical Imaging 2004: Image Processing*, Volume 5370, pp 587 – 597, 2004. © SPIE.



8.11 Remarks

Preferred orientation and directional distributions relate to the functional integrity of several types of tissues and organs; changes in such patterns could indicate structural damage as well as recovery.

Directional analysis could be used to study the health and well-being of a tissue or organ, as well as to follow the pathological and physiological processes related to injury, treatment, and healing.